POLITECNICO DI TORINO

Collegio di Ingegneria Meccanica, Aerospaziale, dell’Autoveicolo e dalla Produzione

Corso di Laurea Magistrale
in Ingegneria Meccanica

BLADELESS WIND ENERGY CONVERSION

Master Thesis of:

Marco BORETTO Matr. 242496

Supervisors

Prof. Giuliana Mattiazzo

Prof. Giovanni Bracco

Prof. Marco Belloli

April 2019

Index

Abstract

In recent years, there has been a strong interest in new approaches to wind generation, with particular attention to technologies able to be profitable in small scale and reduce the visual impact linked to traditional wind turbines. Because of their relative constructive simplicity, among the various proposals many are based on aeroelasticity phenomena grouped under the name of Flow-induced Vibrations, which are oscillations generated by the interaction between fluid and elastic structures. However, although these phenomena have long been studied in some areas of engineering because of their destructive effects, their actual potential for energy conversion is still debated.

In this context, the aim of the thesis is to investigate the characteristics and potentialities of these fluid-elastic interactions in energy production, focusing in particular on two phenomena: vortex-induced vibrations (VIV) and galloping. In this regard, an in-depth analysis of the physical models of the two phenomena and their sensitivity to the various parameters of the system was carried out. Furthermore, a preliminary design of systems able to generate different levels of power has been proposed, in order to study their performance as the size changes.

The main results of this analysis reveal that the conversion systems based on flow-induced vibrations are characterized by a poor conversion efficiency, little affected by the size of the system and considerably below that of traditional wind turbines. However, it was also highlighted how these phenomena can be induced even at low wind speeds, where traditional systems present different criticalities. As a result, the possible application of VIV or galloping-based wind energy conversion systems seems to be restricted to the power supply of isolated electronic devices and sensors.

Sommario

Negli ultimi anni si è sviluppato un forte interesse verso nuovi approcci alla generazione eolica, con particolare attenzione alle tecnologie in grado di essere profittevoli in piccola scala e ridurre l'impatto visivo legato alle turbine eoliche tradizionali. Per via della loro relativa semplicità costruttiva, tra le varie proposte molte sono basate su fenomeni aeroelastici raggruppati sotto il nome di Flow-induced Vibrations, ovvero oscillazioni generate dall'interazione tra fluido e struttura. Tuttavia, sebbene questi fenomeni siano da tempo studiati in alcuni ambiti dell'ingegneria a causa dei loro effetti distruttivi, il loro effettivo potenziale nella conversione energetica è molto dibattuto.

In questo contesto, l'obiettivo della tesi è quello di indagare le caratteristiche e le potenzialità di queste interazioni aeroelastiche nella produzione di energia, soffermandosi in particolare su due fenomeni: vortex-induced vibrations e galloping. A questo proposito, è stata svolta un'analisi approfondita dei modelli fisici dei due fenomeni e della loro sensibilità rispetto ai vari parametri del sistema. Inoltre, è stato svolto un design preliminare di sistemi in grado di generare diversi livelli di potenza, in modo da studiarne le performance al variare della dimensione.

I principali risultati di questa analisi rivelano che i sistemi di conversione basati sulle flow-induced vibrations sono caratterizzati da una scarsa efficienza di conversione, poco affetta dalle dimensioni del sistema e notevolmente al di sotto di quella delle tradizionali turbine eoliche. Tuttavia, viene anche evidenziato come questi fenomeni possano essere indotti anche a basse velocità del vento, dove i sistemi tradizionali presentano diverse criticità. Di conseguenza, la possibile applicazione di sistemi di conversione di energia eolica basati su VIVs o galloping sembra essere ristretta all'alimentazione di apparecchi elettronici e sensori isolati.

1. Introduction

In recent years, a strong interest in new concepts of wind power generators has grown, especially in the application of Flow-Induced vibrations as an alternative mechanism for wind power harvesting.

Through years, the traditional concept of horizontal axis wind turbines has been developed to maximize the exploitation of strong wind flows. As a result, wind turbine are growing bigger and bigger, in order to maximize the swept area and, proportionally, the power output. Moreover, traditional wind turbines efficiency generally grows with their size, reaching values as high as 45%, which are really near the Betz limit of 59.7%. As a result, despite large turbines require high costs of installations, operation and maintenance, wind power production is still a good alternative to fossil fuel. It is now the second renewable resource by global generation of electricity (after hydropower) and its installed capacity is continuously growing, having almost doubled in the last five years. According to the *International Energy Outlook 2017*, this positive trend is mainly due to the high economic competitiveness of wind power, even with respect to traditional fossil fuel resources (EIA, 2017).

Surprisingly, traditional wind turbines are somehow unpopular because of some drawback that comes directly from their big size. Their visual impact, together with the noise pollution they generate, are the main threat to wind turbine installation in proximity of densely populated areas or important naturalistic sites. Conversely, decreasing in size makes wind turbine less profitable with respect to other energy sources or different use of lands, usually resulting in a poor application for distribute small generation.

For these reasons, there have been many attempts in creating new concepts of wind power generator, based on various physical mechanisms, with the aim to obtain an alternative that is easier to integrate into landscapes and urban areas. Until now, none of them has been completely successful, but there are really interesting concepts that continue to challenge the existent paradigm. As an example, the concept proposed by *O-wind*, is inspired by a wind-powered rover and is specifically designed to harvest power from turbulent and ever-changing wind in urban environment. Or else, the one proposed by *Vortex Bladeless SL*, which is based on an aeroelasticity phenomenon called Vortex-induced vibrations, and aims to be a kind of "plug-in" device, characterized by an easy installation and a minimal maintenance effort.

Figure 1.1 O-wind (left) and Vortex Bladeless (right) wind turbine concepts

Furthermore, since wind exists almost everywhere, such as the flow in indoor heating and ventilation air conditioning systems and natural wind in outdoor spaces, wind power is also seen as an interesting energy source for isolated low power electronic devices and sensors, disconnected from the grid. In this case, the target of energy harvesting is to operate autonomous powered electronic devices over their lifetime. To this end, being able to exploit the energy sources present in the surrounding environment, even if small, can be useful and advantageous also from the economic point of view, as it allows to save on the cost of purchase, installation and replacement of batteries or energy storage systems. In this context, many researchers explored wind power generation from flow-induced vibrations (FIVs): mainly because their simple structure, FIVs-based energy harvesters have the potential to be an affordable way to provide low power quantities to isolated devices.

It seems clear that for each wind power application it is necessary to identify the most suitable method to harvest energy, based on the required power output, available space and costs. In this scenario, the purpose of this work is to explore the potential of the main Flow-induced vibration phenomena as mechanisms for wind power harvesting, understanding the involved mechanisms of conversion and assessing their best application field.

In Chapter 2 flow-induced vibrations are presented from a phenomenological point of view, explaining the mechanisms at the basis of VIVs and galloping, and the notation used in the following chapters. A deep analysis of the state of the art is then carried on in Chapter 3, focusing on the existing attempts to use FIVs as harvesting mechanisms. Subsequently, in Chapter 4 and 5, the mathematical model describing VIVs and galloping have been analysed and the effects of various parameters are assessed. Based on the analysis results, in Chapter 6, VIVs and galloping are compared in order to identify which of the two fluid-structure interactions has the bets potential in energy harvesting, and an original concept for an energy harvester is proposed. Finally, in Chapter 7 the performance of the proposed design is evaluated in a case study using real wind data.

2. Flow induced vibrations

In many applications, fluid and solid dynamics are approached independently: as an example, in fluid mechanics, the presence of solids is usually translated into a set of boundary conditions for the flow, often imposing a given flow speed in correspondence of the solid surface. In the same way, in solid mechanics, fluids are usually considered just as the load they apply on a solid surface, which of course can deform the body or affect its motion. However, there are conditions in which fluid and solid dynamics are coupled, and need to be solved together. This is the case of leaves moving in the wind or fishes moving underwater, both of which are examples of fluid-solid interactions. In these problems, fluid and solid dynamics equations are linked by two interface conditions: a kinematic condition that imposes the same velocity to fluid and solid at their interface, and a dynamic condition, which imposes the equilibrium of forces exchanged between the two domains.

Flow-induced vibrations (FIV) are a wide family of fluid-structure interactions, in which a fluid flow induces an elastic or elastically mounted structure into an oscillatory motion. FIVs are generated by the interactions between a flow and a *bluff body,* defined as a body causing the flow to separate from a large section of the structure's surface. It is possible to distinguish many different phenomenon under the huge family of flow induced vibrations. However, all of them are characterized by the same underlying mechanism, consisting into a coupling between the fluid flow and the structure (Figure 2.1)

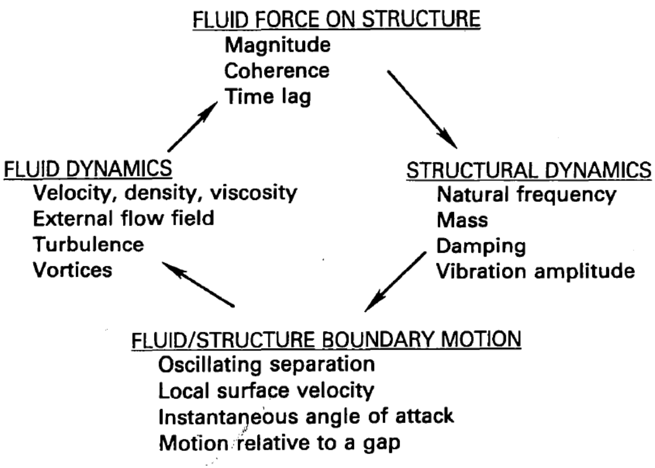

Figure 2.1 Fluid-structure interaction mechanism *(Blevins, 2001)*

In general, the presence of a bluff body perturbs the fluid motion, generating pressure variations. The developed fluid force deforms or puts in motion the structure, and changes its boundary with respect to the fluid. Consequently, fluid dynamics changes and the fluid force developed may do the same, since it is determined by the orientation and velocity of the structure relative to the fluid flow. Moreover, also the corresponding forces exerted by the solid on the fluid may have an effect forcing flow motion (Blevins, 2001).

2.1. Mathematical formulation and dimensionless parameters

In the phenomena analysed in the following chapters, the focus is to study the transverse motion of the solid body with respect to fluid flow. In a general case, the structure consists in a bluff body characterized by a random transverse section, elastically mounted in such a way that only the cross-flow motion is allowed, and subjected to a transverse fluid force (Figure 2.2).

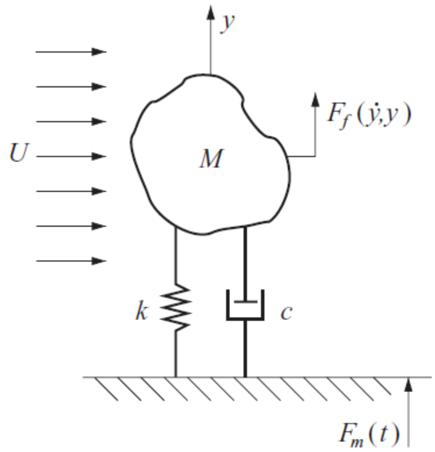

Figure 2.2 General scheme of a single DOF structure

The dynamic equation describing this system is:

$$ml\ddot{y} + c\dot{y} + ky = F_{fluid}(\dot{y}, y) + F_m(t) \tag{2.1}$$

Where k and c are the structural stiffness and damping, F_m is an eventual base excitation, l the length of the bluff body, and $m = m_s + m_a$ is the sum of the structural mass per unit length (m_s) and the added mass (m_a), that represents the effect of the fluid inertia and depend on the section shape and dimensions. Finally, $F_{fluid}(\dot{y}, y)$ is the fluid force responsible of the motion, which following the notation of Païdoussis can be expressed as:

$$F_{fluid}(\dot{y}, y) = \frac{1}{2}\rho U^2 Dl C_{f1}(\dot{y}, U) + \frac{1}{2}\rho U^2 Dl C_{f2}(y, U) \tag{2.2}$$

With ρ being the fluid density, U the flow speed and D the characteristic dimension of the transverse section, that is usually the dimension facing the flow. C_{f1} and C_{f2} are fluid-dynamic force coefficients, chosen to separate the effects of transverse speed and displacement respectively.

In the study of flow-induced vibrations, it is useful to obtain the dimensionless form of the governing equation in order to obtain general results. Consequently, a set of dimensionless parameters are defined.

Structure natural frequency	$\omega_n = \sqrt{\frac{k}{ml}}$	*Damping ratio*	$\zeta = \frac{c}{2ml\omega_n}$
Reduced displacement	$Y = \frac{y}{D}$	*Reduced mass*	$m_r = \frac{m}{\rho D^2}$
Reduced velocity	$U_r = \frac{U}{f_n D}$	*Structure-based time scale*	$\tau = \omega_n t$

Among them, it is important to highlight the importance of the reduced mass m_r and the reduced velocity U_r, which are obtained from the ratio between structure and fluid parameters. The reduced mass represents the ratio between the average density of the structure and the density of the fluid and, together with the damping ratio, plays a fundamental role in determining the structural response in flow-induced vibrations problems: as a general rule, the lower the value of m_r (and ζ) , the more the structure is subject to FIVs.

The second fundamental parameter in FIVs is the reduced velocity U_r, which represents the ratio between the two timescales of fluid and solid dynamics. In facts, it is possible to define a timescale for both fluid and solid domain as the time at which information propagate inside the system: for the solid domain, T_{solid} is given as $1/\omega_n$, and represents the response time scale of an oscillation motion; for the fluid, it is possible to define T_{fluid} as D/U, that is the time required by a fluid particle to travel across the main system dimension. The reduced velocity is then obtained as:

$$U_r^* = \frac{T_{solid}}{T_{fluid}} = \frac{U}{\omega_n D} \tag{2.3}$$

Which is an equivalent definition of the reduced velocity of the previous one ($U_r = \frac{U}{f_n D}$), from which differs just because of a constant term. Both of them are used in the literature, depending on the author and on the purpose.

The value of reduced velocity U_r is also an important tool for classifying the different phenomena in the family of flow-induced vibrations: at different range of reduced velocity correspond different approximations, made in order to simplify the general problem getting rid of uninfluential terms in the equations, and obtain simpler and effective models (Sebastien Michelin, 2018).

Substituting Equation 2.2 and the defined dimensionless terms into Equation 2.1, changing the time scale from t to τ, and neglecting the base excitation term, we obtain the general governing equation in dimensionless form:

$$\ddot{Y} + 2\zeta\dot{Y} + Y = \frac{1}{2}\frac{U_r^{*2}}{m_r}C_{f1}(\dot{Y}, U_r) + \frac{1}{2}\frac{U_r^{*2}}{m_r}C_{f2}(Y, U_r) \tag{2.4}$$

Even if it is clear that the flow acts as an energy source for the dynamic system, flow-induced vibrations are often referred as self-induced oscillations because of the way the governing motion equations are written. In facts, assuming that the flow forces can be expressed as a third degree polynomial function of $\dot{Y}$ and :

$$\frac{1}{2}\frac{U_r^{*2}}{m_r}C_{f1}(\dot{Y}, U_r) = \beta_1(U_r^*)\dot{Y} - \beta_2(U_r^*)\dot{Y}^3 \qquad \frac{1}{2}\frac{U_r^{*2}}{m_r}C_{f2}(Y, U_r) = \beta_3(U_r^*)Y - \beta_4(U_r^*)Y^3$$

and then substituting and rearranging the equation, it becomes:

$$\ddot{Y} + [2\zeta - \beta_1(U_r) + \beta_2(U_r)\dot{Y}^2]\dot{Y} + [1 - \beta_3(U_r) + \beta_4(U_r)Y^2]Y = 0 \tag{2.5}$$

In such a formulation, the effect of the fluid is incorporated into equivalent damping or rigidity terms. Under certain conditions of reduced velocity, for instance when U_r exceeds a certain threshold, the system can show both damping and stiffness instabilities, which appear as self-induced oscillating motions.

FIVs include a vast family of phenomena, sometimes very different from each other. In Figure 2.3, it is reported a classification of Flow-induced vibrations made by Blevins.

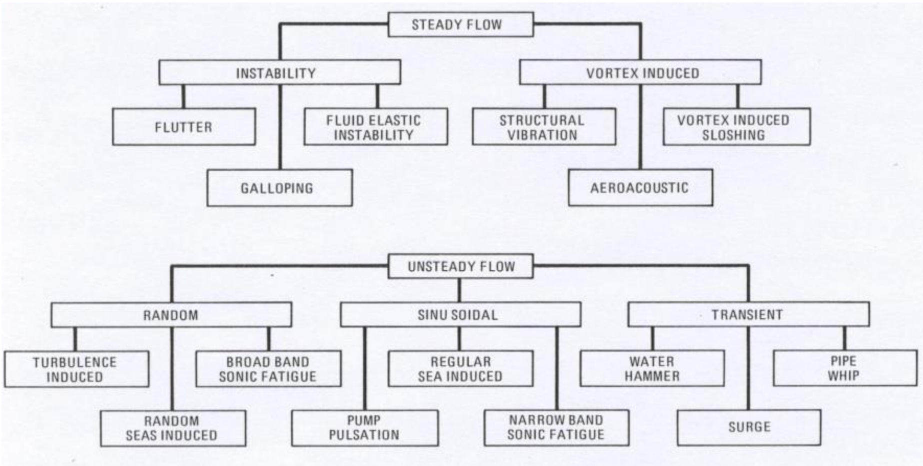

Figure 2.3 Flow-induced vibrations classification *(Blevins, 2001)*

Since the focus of this work is to study the applications of FIVs in energy production, just a couple of the FIVs phenomena have been investigated, namely galloping (or stall flutter) and vortex-induced vibrations, the selection of which was based on the study of scientific literature on energy harvesting applications of fluid-structure interactions.

Hence, in the following is reported a brief presentation of the two phenomena and the mathematical models used to describe them.

2.2. Vortex-induced vibrations (VIVs)

Vortex Induced Vibrations is a particular flow-structure interaction based on the coupling between the structure vibration and the *vortex shedding* in the structure wake.

The following words by Blevins provide a clear description of how the vortex-shedding phenomenon is established: "*as a fluid particle flows toward the leading edge of a cylinder, the pressure in the fluid particle rises from the free stream pressure to the stagnation pressure. The high fluid pressure near the leading edge impels flow about the cylinder as boundary layers develop about both sides. However, the high pressure is not sufficient to force the flow about the back of the cylinder at high Reynolds numbers. Near the widest section of the cylinder, the boundary layers separate from each side of the cylinder surface and form two shear layers that trail aft in the flow and bound the wake. Since the innermost portion of the shear layers, which is in contact with the cylinder, moves much more slowly than the outermost portion of the shear layers, which is in contact with the free flow, the shear layers roll into the near wake, where they fold on each other and coalesce into discrete swirling vortices. A regular pattern of vortices, called a vortex street, trails aft in the wake*" (Blevins, 2001).

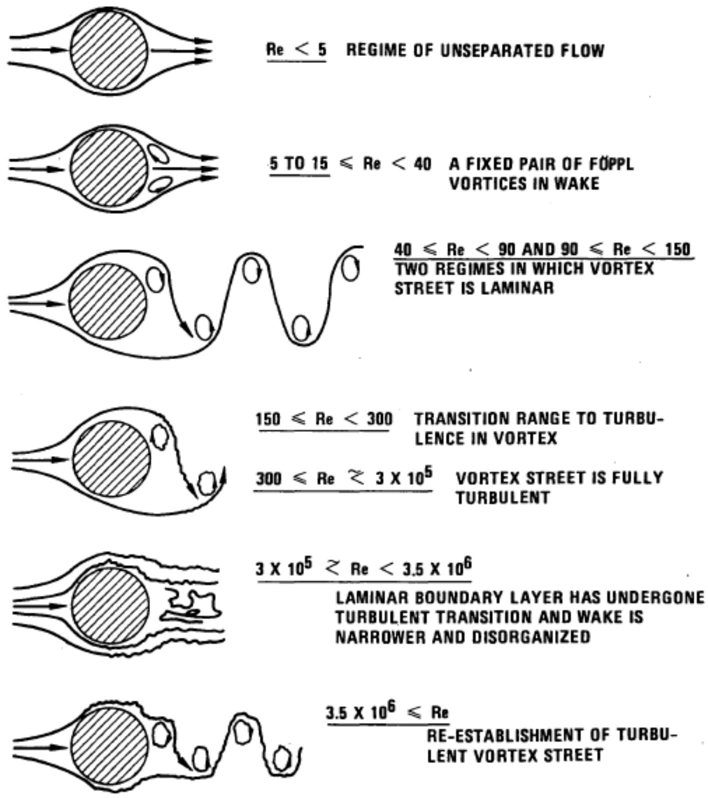

Figure 2.4 Vortex shedding at different Reynolds *(Blevins, 2001)*

In Figure 2.4 we can see that Vortex shedding behavior is a function of Reynolds number: at very low Re, the fluid follows the cylinder's surface in a smooth and unseparated flow, until, from around Re = 5, two fixed and symmetric vortices appear in the wake. In the range from 40 to 150, a periodic laminar wake of staggered vortices appears. From Re = 150, there is a transition phase in which vortices start becoming turbulent, while the flow around the cylinder remains laminar. Turbulence in vortices is then completely established during the *subcritical* range, $300 < Re < 1.5 \times 10^5$. Over $Re = 1.5 \times 10^5$ starts a new transitional phase in which turbulence is developed also along the cylinder boundary, and the flow becomes irregular and disorganized. Finally, above $Re = 1.5 \times 10^5$ there's a new establishment of turbulent vortex street.

Since vortex shedding is a phenomenon involving the wake dynamic behind the body, a second fundamental dimensionless parameter in the vortex shedding phenomenon is the Strouhal number, whose meaning is the ratio between the fluid flow and the vortex shedding timescales.

$$S_t = \frac{f_{St} D}{U} = \frac{T_{fluid}}{T_{vortex}} \qquad (2.6)$$

Where f_{St} is the frequency with which the vortices appear.

Interestingly, the experimental trend of Strouhal number reported in the Figure 2.5, shows that S_t remains quite constant (about 0.2) in a large range of Reynolds number, in particular in the range during which the vortex shedding happens. This means that the vortex shedding timescale is almost linearly dependent to the fluid flow one over a wide range of fluid velocity. Also, form the equation it comes that given the dimension of the bluff body, the vortex shedding frequency varies linearly with the speed of fluid flow.

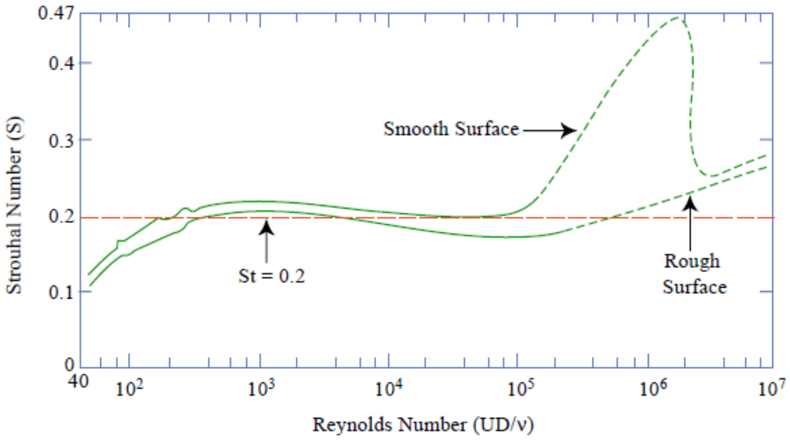

Figure 2.5 Strouhal Number as a function of Reynolds number *(Blevins, 2001)*

The generation of vortices in the flow produces a perturbation in pressure distribution on the cylinder boundary and consequently a force interaction between fluid and structure. As usual, the force exerted by the fluid on the cylinder can be divided in two components: the *Drag force*, in the direction of the flow, and the *Lift force*, that acts in the direction orthogonal to the flow. Due to the periodicity in pressure variation caused by vortex shedding, both Drag and Lift forces change their value periodically: the fluctuation in Drag force happens around a positive value and at twice the frequency of the vortex appearance, while Lift force oscillations between symmetric positive and negative values occur at the same frequency of vortex shedding.

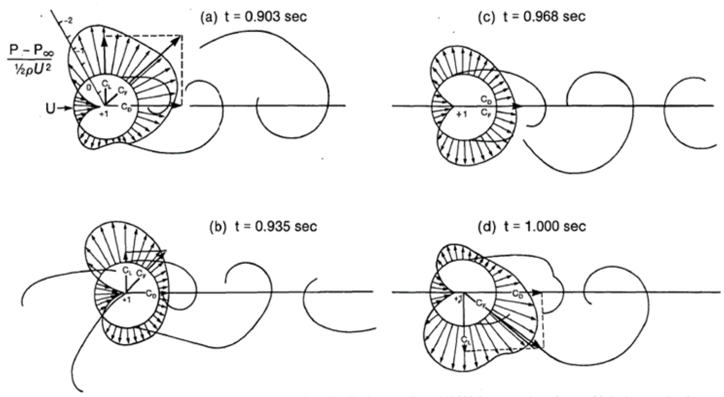

Figure 2.6 Pressure distribution caused by vortex shedding *(Blevins, 2001)*

If the bluff body is elastic or elastically mounted, the fluid force can induce the body in an oscillating motion, producing the effect called *Vortex-Induced Vibration (VIVs)*, thus absorbing part of the flow energy in the form of mechanical energy. In particular, the effects of VIVs become significant when there's coincidence between the forcing frequency, which is the same as the vortex shedding one, and structure natural frequency. Thus, since the resonance condition can also be expressed as the coincidence between T_{solid} and T_{vortex}:

$$\frac{T_{solid}}{T_{vortex}} = 1 \rightarrow \frac{T_{solid}}{T_{fluid}} S_t = U_r S_t = 1 \rightarrow U_r \cong 5 \tag{2.7}$$

However, experimental activities on VIVs show that VIVs generate a significant amplitude response over a relatively wide range of reduced velocities. Researcher attributed the cause at the feedback effect of the structure motion on the vortex shedding, that determine a coupling between the fluid-dynamic phenomenon and the structural dynamics of the body.

The results reported in Figure 2.7 show the significant impact of transverse cylinder oscillations on the vortex shedding phenomenon. As we can see, increasing the reduced velocity, the vortex shedding frequency initially follows the linear law proportional to Strouhal number. Once the excitation frequency approaches values close to the structure natural frequency f_n, transverse oscillations amplitude grows significantly and the shedding frequency he begins to break away from the trend expected for a fixed structure.

The cause of this behavior is that when the vibration amplitude *A/D* reach values around 0.1, the growth of the virtual body dimensions seen by the flow consequent to the structure motion determines a decrease of the shedding frequency, which change to match the natural frequency of the body as we can see in the Figure 2.7 (Sarpkaya, 2004). According to Sarpkaya, the body motion becomes dominant in the phenomenon, in the sense that it accommodates the changes in vortex shedding by letting the flow change its virtual mass and hence its frequency and acceleration, so that both the flow and the body arrive at a common frequency to which the body responds with exuberance.

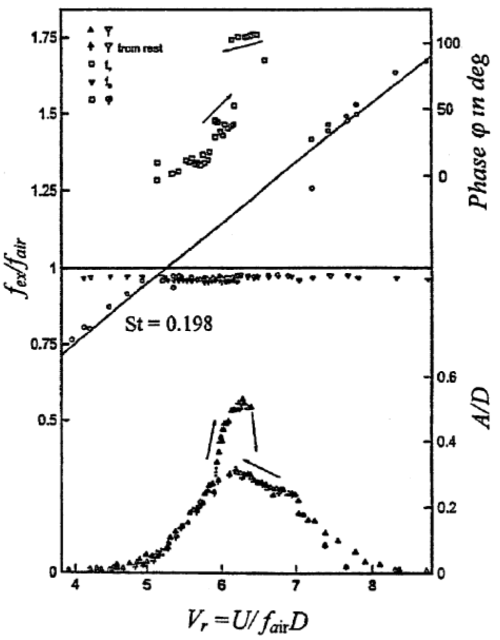

Figure 2.7 VIVs response *(Sarpkaya, 2004)*

Interestingly, the synchronization between the vortex shedding and the structure oscillation occurs over a *relatively* large range of flow velocity, and not just in correspondence of one specific flow speed. During this so called “lock-in” phenomenon, the body motion acts as a magnifier, organizer and synchronizer of the phenomenon: as a result, the force exchanged by the fluid grows, as well as the amplitude of the body oscillations. Finally, when the reduced velocity overcomes a certain value, typically in range of $U_r = 8 \div 10$, the synchronization stops and the transverse vibrations amplitude return to small values, while the shedding frequency returns to the linear proportion with U_r.

Different kind of mathematical models have been proposed in order to obtain the characteristic VIVs dynamic behavior. Anyway, the differences between them are mostly in the fluid force modelling, while the structure is modeled as a simple mass-spring-damping oscillator.

$$m\ddot{y} + c\dot{y} + ky = \frac{1}{2}\rho U^2 D C_L \tag{2.8}$$

Where the lift force coefficient C_L represents the lift contribution of the forces generated by the vortex in wakes, expressed in different ways, depending on the model considered. In his book, Païdoussis reported three main kinds of models, based on different assumptions in the description of the fluid force acting on the bluff body (Païdoussis, et al., 2011):

- *Forced system models*, where the fluid force is only a function of time. In this case, C_L is modelled as a sinusoidal function, with vortex shedding frequency and constant amplitude, C_{L0} , measured in static experiments:
$$C_L = C_{L0} \sin(2\pi f_{St} t) \tag{2.9}$$
It is important to note that, by construction, forced system models can only contemplate a normal resonance response of the system, characterized by the necessity of almost exact coincidence between vortex shedding and natural frequencies, and by the appearance of theoretically infinite amplitudes of oscillations in presence of low damped systems.
- *Fluid-elastic system models*, where the fluid force is function of both time and structure motion, described by the y coordinate or its derivatives. As an example, the lift force coefficient can be expressed as:
$$C_L = C_{L0}\left(\frac{y}{D}\right) \sin(2\pi f_{St} t) \tag{2.10}$$
Where the time dependency is delegated to sinusoidal function, while the semi-amplitude C_{L0} takes into account the effects of motion on the force intensity: in facts, while for moderate oscillation amplitudes the lift force is enforced, when the amplitudes grow over a certain limit there's a negative effect on the lift intensity. This experimental behaviour is usually taken into account introducing polynomial expression for C_{L0}, tuned on

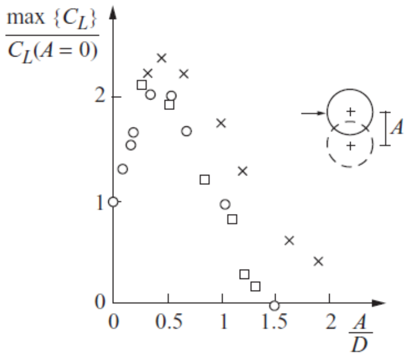

Figure 2.8 Lift force magnification due to transverse motion *(Païdoussis, et al., 2011)*

experimental measures:
$$C_{L0} = C_{L0\,static} + A\left(\frac{y}{D}\right) + \mathrm{B}\left(\frac{y}{D}\right)^2 \tag{2.11}$$
In this way, it is possible to obtain the self-limiting amplitude response typical of VIVs, but the lock-in between structure and wake is still impossible to reproduce.
- *Coupled system model*, where the fluid force is proportional to a variable related to the wake dynamics, the evolution of which is affected by the structure motion. In this models, it is common to define a variable representing the strength of the vortices in the wake: for instance, the variable
$$q = 2\frac{C_L}{C_{L0}} \tag{2.12}$$

given by the ratio between the dynamic lift force coefficient and the static one. Also the wake variable describes an oscillating dynamics, found to be properly described by a Van der Pol oscillator equation (Hartlen & Currie, 1970), in which a coupling term takes into account the effect of the structure motion, which has been suggested to be considered as a function of its transverse acceleration $\ddot{y}$ (Facchinetti, et al., 2004).

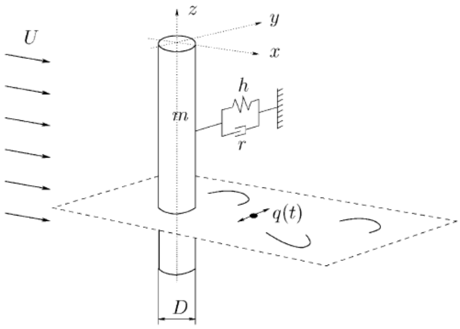

Figure 2.9 Structure and wake coupled model *(Facchinetti, et al., 2004)*

As a result, coupled system models describe VIVs by means of a system of two coupled oscillator equation, whose frequencies synchronize over a wide range of reduced velocity, obtaining the lock.in effect, and producing a self-limiting amplitude response.

$$\begin{cases} m\ddot{y} + c\dot{y} + ky = \frac{1}{2}\rho U^2 D \frac{C_{L0}}{2} q \\ \ddot{q} + \varepsilon\omega_f(q^2 - 1)\dot{q} + \omega_f^2 q = A\ddot{y} \end{cases} \tag{2.13}$$

Where ω_f is the vortex shedding frequency expected if the structure is fixed, and ε and A are two semi empirical parameters tuned on experimental results.

2.3. Transverse galloping

Transverse galloping is a fluid-structure interaction found in an intermediate range of reduced velocity U_r, characterized by a relatively high flow speed, such that the body velocity can't be neglected with respect to the fluid speed, but it can be considered "frozen in time" while it comes to solve the fluid dynamic of the system. In the scientific literature, the application of the so called *pseudo-static approximation* is usually restricted to a limited range of reduced velocity, which lower limit varies from 10 to 30 depending on the author considered.

Considering a body with a general transverse section and moving transversely to the flow with a not negligible velocity, it is clear from the Figure 2.10 that it is equivalent to consider an apparent change in the angle of incidence α with respect to the flow, dependent on the velocity of the bluff body:

$$\tan(\alpha) = \frac{\dot{y}}{U} \tag{2.14}$$

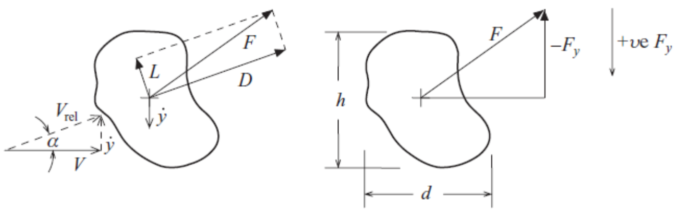

Figure 2.10 Change of the angle of attack due to transverse motion *(Païdoussis, et al., 2011)*

Assuming that the structure is elastically mounted allowing only the cross-flow motion, the dynamic equation of the system is:

$$ml\ddot{y} + c\dot{y} + ky = \frac{1}{2}\rho U^2 Dl[-C_L\cos(\alpha) - C_D\sin(\alpha)] \tag{2.15}$$

Where C_L and C_D are the fluid-dynamic lift and drag force coefficient, whose value is a function of the section shape and the angle of attack, and consequently of the transverse velocity of the body. Consequently, these coefficients could be substituted by an equivalent flow induced damping term, which can be either positive or negative depending on the variation of the lift and drag coefficients with the angle of attack.

Depending on the section shape and orientation, the effect of fluid force can have different effects (Figure 2.11).

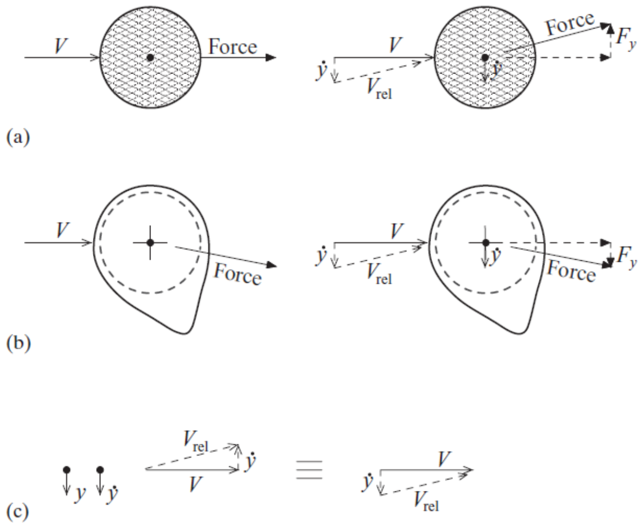

Figure 2.11 Differences of behaviour depending on the transverse section shape *(Païdoussis, et al., 2011)*

For instance, circular sections would develop a resulting fluid force in the same direction of the fluid flow, the transverse component of which oriented in the opposite direction with respect to the current cross-flow structure speed $\dot{y}$. In this case, the fluid force would produce a negative work, thus having the same effect as a positive damping. On the other hand, different sections exist in which the resulting fluid force would be oriented in such a way that its component in the y direction would be oriented in the same direction as the transverse body velocity $\dot{y}$, resulting in a positive work flux from the fluid to the system, equivalent to a negative damping contribution.

Considering a situation in which the transverse body velocity is near to zero, it is possible to linearize the motion equation to obtain the necessary condition for the galloping instauration. In facts, taking in to account that, for $\rightarrow 0$:

$$\cos(\alpha) \cong 1 \qquad \sin(\alpha) \cong 0 \qquad \alpha \cong \frac{\dot{y}}{U}$$

And assuming that we are considering a symmetric section with respect to the in-line direction, so that

$$C_L|_{\alpha=0} = 0 \qquad \left.\frac{\partial C_D}{\partial \alpha}\right|_{\alpha=0} = 0$$

the motion equation becomes:

$$ml\ddot{y} + \left[c + \frac{1}{2}\rho \mathrm{U} D l \left(\left.\frac{\partial C_L}{\partial \alpha}\right|_{\alpha=0} + C_D|_{\alpha=0} \right) \right] \dot{y} + ky = 0 \tag{2.16}$$

It is clear that galloping instability is possible only if the term $\left(\left.\frac{\partial C_L}{\partial \alpha}\right|_{\alpha=0} + C_D|_{\alpha=0} \right)$ is negative, which depend only on the section properties. Not all kinds of sections are susceptible to galloping: as anticipated, circular section cannot experience this instability, while square, rectangular, “D” shape and even blade section do. With this regard, the instability that may occurs when a body of arbitrary shape moves transversely to the flow is usually referred as *transverse galloping*, while the term *stall fluttering* is specifically referred to a blade section body. Anyway, the principle that drives the phenomenon is the same.

Moreover, the instability will effectively arise only when the total damping term is negative, which can happen when the flow speed is higher that a threshold value, defined as the critical flow speed:

$$U_{cr} = \frac{2c}{\rho D l \left(-\left.\frac{\partial C_L}{\partial \alpha}\right|_{\alpha=0} - C_D|_{\alpha=0} \right)} \tag{2.17}$$

From this flow speed on, the system will absorb energy from the flow, becoming unstable. This involves high amplitudes of oscillations, whose values are usually determined equating the absorbed energy from the flow over a complete oscillation cycle, and the energy dissipated over the same by mechanical or electromechanical conversion damping. Moreover, the speed range in which galloping appears is only limited by an inferior limit, represented by the critical speed.

3. State of the art

3.1. Flow induced vibrations as a mechanism for energy harvesting

Flow induced vibrations have been studied since decades by civil engineers because of their potentially destructive effects. Probably the most famous example of FIVs effects on civil structures is the Tacoma Narrows Bridge disaster, become popular also thanks to the impressive video that shows the oscillations of the bridge until its collapse. However, as reported by Païdoussis, FIVs play an important role also in heat exchangers tubes arrays, high-rise buildings, submerged pipelines and transmission lines. In all these examples, FIVs can produces high amplitude oscillations interfering with the expected behaviour, or eventually leading to fatigue failures. Consequently, the understanding of the involved fluid-structure interaction mechanisms is crucial in order to avoid the occurrence or limit the negative effects of FIVs.

Nevertheless, in recent years has grown a new interest with respect to flow-induced vibrations into energy generation, with many researchers studying FIVs as a mechanism for energy harvesting from wind and water currents, with the aim of designing simple and economic devices, capable to work in a small scale in a profitable way.

Notably, one of the first analysis of FIVs potential as an alternative to traditional wind turbines was carried out in the '80 by Peter South. In his work, it has been noted that these phenomena might be exploited through simpler and cheaper systems than traditional wind turbines, mainly because of the nature of the motion involved (mostly linear), that do not require high quality materials. However, it was reported that FIVs do not have significant advantages with respect to traditional turbines, in particular when it comes to big scale projects (Peter South, 1983). As a matter of facts, in Peter South analysis only a few FIVs phenomena have been cosidered. Hence, many researcher continued investigating FIVs as mechanisms for small and micro scale wind energy harvesters.

An important feature of FIVs energy harvesters is that the extraction of mechanical power from the system, necessary to produce electrical output and seen as a damping effect, inevitably affects the system dynamics, resulting in lower amplitude of oscillations or even the disappearance of the phenomenon, depending on the magnitudes involved. Hence, in order to use FIVs for harvesting energy it is critical to control the conversion intensity, which represent how much of the mechanical energy is converted into electricity.

$$\eta = \frac{\text{Extracted energy}}{\text{Fluid K.E. flux}}$$

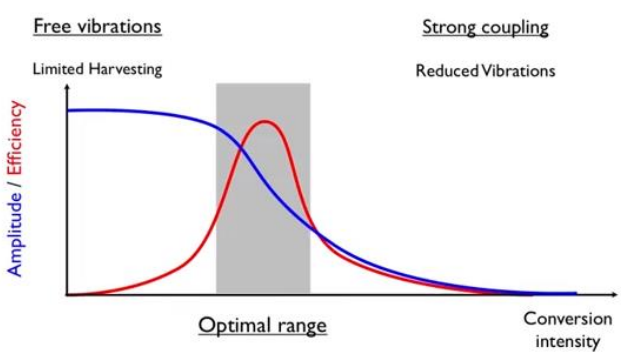

Figure 3.1 Effect of conversion intensity on efficiency *(Sebastien Michelin, 2018)*

If the conversion intensity is low, the solid's dynamics is marginally impacted: basically, the solid does not see the energy taken out, and vibrations amplitudes remain large. However, the harvested energy and efficiency are very limited. On the other hand, if the conversion intensity is large, vibrations are damped out too strongly, greatly reducing the energy extracted from the flow and therefore the system's efficiency (Figure 3.1).

Therefore, identifying and quantifying an optimal conversion regime between these two limits, where the vibrations are modified but not completely mitigated by the energy extraction, is a crucial objective to effectively exploit flow-induced vibrations in energy harvesting (Sebastien Michelin, 2018).

In the next paragraphs, it is reported a literature review on the topic of energy harvesting from flow-induced vibrations, with a major focus on applications involving VIVs and galloping of bluff bodies. As it will become clear, the majority of concepts for wind power harvesting have been actually implemented in micro-scale power production, with just a few examples of studies for bigger scales. However, the situation changes if we consider applications aiming to harvest power from water currents in oceans or rivers, where intrinsic advantages make flow-induced vibrations more effectives.

3.2. Energy harvesters based on VIVs

Given the self-induced and self-limited amplitude characteristics of VIVs, many researchers have investigated their potential application into fluid power conversion, exploring many possible strategies and configurations.

One of the simplest and most common configurations has been presented by H D Akaydin (Figure 3.2). It consists in a circular cylinder mounted on a flexible beam, allowing only a cross-direction motion with respect to flow. On the beam is then applied a piezoelectric layer, able to convert the elastic energy into electric tension as the beam bends. Depending on the beam stiffness, the system will experience the vortex-induced vibrations in a specific range of wind speed. By experimental tests, Akaydin demonstrated that this simple concept is able to produce a little amount of power: with a 1.98 cm diameter and 20.3 cm length cylinder, a maximum power of 0.1 mW was achieved at a low wind speed of 1.192 m/s (H. D. Akaydin, 2012).

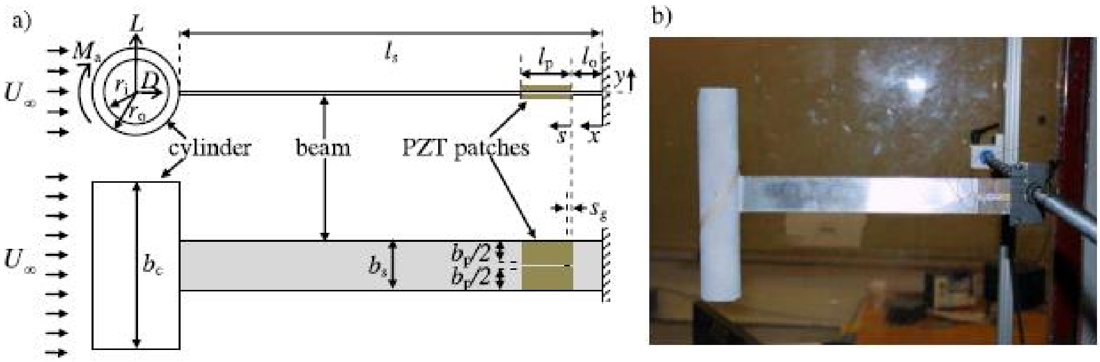

Figure 3.2 Energy harvester based on VIVs *(H. D. Akaydin, 2012)*

A different configuration, in which the cylinder is elastically mounted through a piezoelectric beam anchored to its lower edge in a vertical position (Figure 3.3), has been analyzed both numerically and experimentally (Jia, et al., 2018). Experimental results show a peak power of 635.04 µW at a wind speed of 4.20 m/s, with a bluff body diameter and length of 40 and 80 mm, respectively.

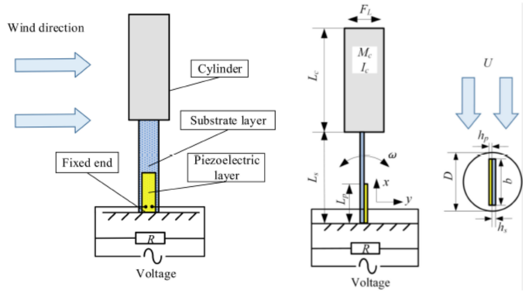

Fi

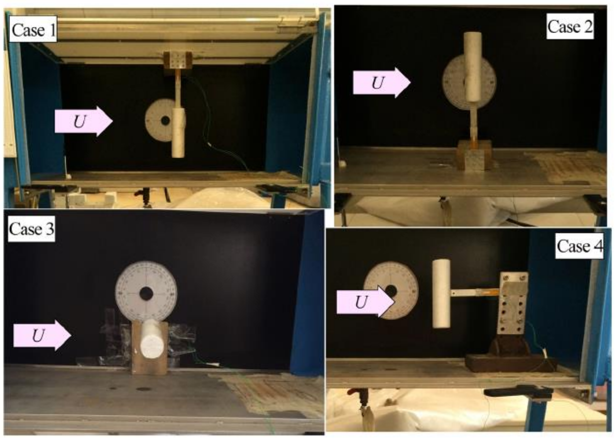

Figure 3.4 Different configurations for VIVs based energy harvesters *(Dai, et al., 2016)*

Both the previous two configurations have been compared in an experimental study, together with two more, maintain the same characteristics of the bluff body (Dai, et al., 2016). The results show that the different mountings produce differences in the natural frequency of the system, and consequently on the wind speed range in which the lock-in phenomenon appears. Also the power produced is different in the 4 four cases. With a cylinder 30 mm in diameter and 120 mm in length, the first three configurations, which operate in a similar wind speed range and similar damping, show slightly different behavior, with a maximum registered power production of about 25, 30 and 20 µW at a wind speed of 1.6, 1.6 and 1.5 m/s, respectively. The fourth configuration, that is the same as the one presented by Akaydin, operates at an higher frequency of about 12 HZ with respect to the 6 Hz of previous three, and produces a peak power of 145 µW at 3.6 m/s wind speed.

A famous attempt to exploit VIVs in the production of energy on a medium-small scale has been made by the Spanish start-up Vortex Bladeless.

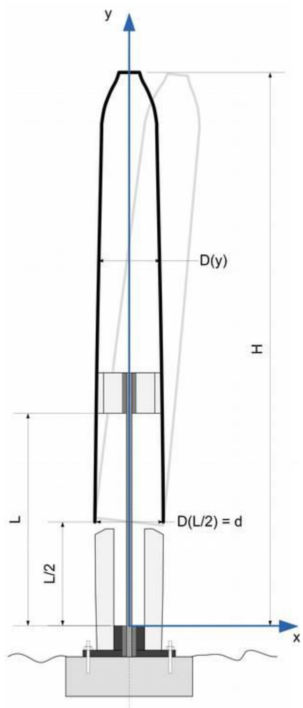

Figure 3.5 Vortex Bladeless turbine scheme *(Vortex Bladeless S.L., 2018)*

Vortex Bladeless turbine structure consists in a vertical rigid mast, the *capture element*, mounted on a flexible rod, anchored to the floor. While invested by the wind flow, the mast generates alternating vortices in the wake, and it's put in an oscillating motion by the alternating forces exchanged with the fluid. A significant energy transfer between fluid and structure is obtained when the coupling between vortex shedding and structural natural frequencies occurs. Hence, the bladeless wind turbine can produce power only in a specific range of wind speed, out of which it naturally stops (Vortex Bladeless S.L., 2018).

In order to extend the wind speed working range, a tuning system is provided with the aim to adapt the natural frequency of the structure to different wind speeds. A first passive adaptation is given by introducing two concentric rings of permanent magnets (and/or electromagnets) that result in a non linear spring for the system dynamics: these magnets repulsive force grows with the square of the movement amplitude, which is proportional to the fluid force and thus to the flux speed. Eventually, an active control on the system stiffness and damping can be exploited by varying the electromagnets alimentation and the power conversion intensity of the turbine.

Since the motion of the turbine is a 3D flexion oscillation, Vortex Bladeless has designed a particular conversion system, which is probably the most original contribution of this concept. Originally, their *bladeless wind turbine* (BWT) was conceived to convert vibrational energy by means of a piezoelectric generator (Villarreal, 2016). Interestingly, being the structure characterized by a low natural frequency, which is disadvantageous to the piezoelectric energy conversion, a particular system was proposed in order to improve the electromechanical conversion, by decoupling structure and piezoelectric beams frequencies (Figure 3.6). In this solution, the piezoelectric elements are excited by the mast oscillations, and vibrate at frequency close to their natural one.

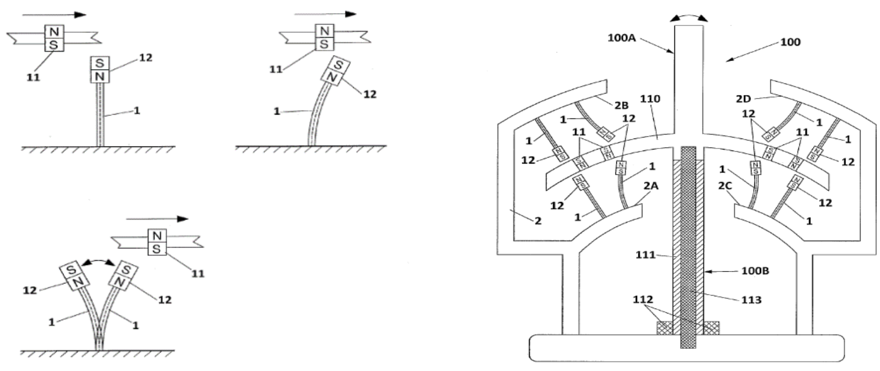

Figure 3.6 Scheme of omnidirectional piezoelectric energy converter *(Villarreal, 2016)*

However, the low conversion efficiency of the piezoelectric layer, together with the fatigue effects to which they were subjected, constituted major problems for this first concept. Consequently, the company moved to a more developed option for the energy conversion, based on electromagnetic induction, by using a permanent-magnets alternator (Villarreal, 2017). More in details, the proposed solution is based on the conversion of the transverse oscillating motion of the mast into a vertical motion, by means of a direction-independent kinematic. This kinematic uses permanent magnets repulsion to convert the kinetic energy of the oscillating mast into an impulsive force that act on a linear electromagnetic alternator each time the mast pass through the vertical configuration, corresponding to the point with maximum kinetic energy (Figure 3.7). The alternator is excited twice in each mast oscillation, and then vibrates at its own natural frequency. Clearly, this decoupling between the mast oscillation frequency and alternator frequency is a common feature with the piezoelectric generator presented before, that in the opinion of the inventor produces a positive effect on the energy conversion.

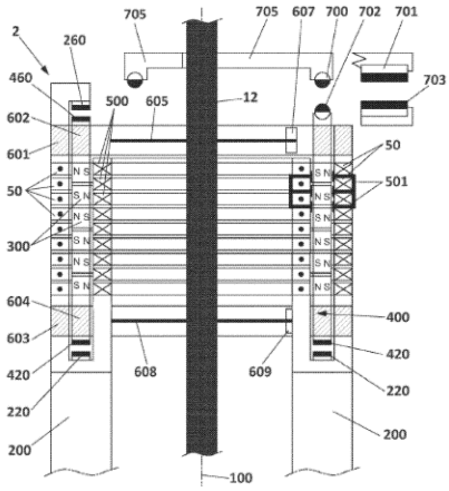

Figure 3.7 Scheme of omnidirectional electromagnetic energy converter *(Villarreal, 2017)*

Another important feature of Vortex Bladeless design is that it has been conceived in order to produce electricity without any friction between components and avoiding the need of a gearbox and lubrication: in the inventors' vision, these abilities are key factors that could make their BWT competitive on the market. First of all, their turbine should emulate the characteristics of photovoltaic cells responsible of making them the most used solution in distributed generation worldwide. That is, mostly, their relatively low cost associated to operation and maintenance. The circular section, together with the structure of the alternator, allow the Vortex Bladeless Turbine to adapt to any wind direction, while the mast diameter can be chosen in order to get the synchronization with relatively low wind speed. Furthermore, low maintenance could be an advantage also in large-scale power production, where cutting down costs might enable higher profitability in off-shore wind farms. Their design should also avoid noise pollution and have less environmental impact, allowing Vortex Bladeless S.L. to get the support of associations fighting for wildlife defense.

On the other hand, many detractors have criticized this technology. First, they argued about the low capture area, which constrains a singular BWT to capture small amounts of wind energy. Then, BWT present a less efficient way to transfer power from the wind flow to the oscillatory mast compared to traditional turbines. Moreover, as all FIVs phenomenon only a fraction of the energy absorbed can be converted in order to not extinguish the motion. This, together with the lower conversion efficiency of the particular linear alternator employed, stated around 70% by Vortex Bladeless in 2015, can be considered an obstacle to the economic advantages promised. Vortex Bladeless CEOs admitted these side effects of their design, but are still convinced that their lower costs can guarantee profitability. Moreover, they are studying how many BWTs would behave when installed one next to the other, in order to maximize power density with respect to land utilization, and thus compensating their lower power output.

Another problem raised by skeptics, is the actual feasibility of scaling up the Vortex Bladeless design, and consequent real savings in terms of installation costs, when the size of BWT reaches dozens of meters to produce an output of the order of kilowatts. Their concern is that at high wind speeds and correspondent increased diameter of the cylinder, the air flow becomes turbulent, producing chaotic effects and causing the oscillating frequency to become difficult to optimize for energy production.

As a matter of fact, recently, the company focused on completing the smallest between their foreseen products model, announcing the “Vortex Tacoma” model to enter the market by the beginning of 2020. With this 2.75 meters tall BWT and a rated power of 100 W, Vortex Bladeless wants to enter the market of photovoltaic solar panels, both as a competitor and as a synergic alternative to obtain a more stable energy production. An estimation of the power curve of the turbine for low wind speeds (from 3 to 10 m/s) has been published on the start-up website, together with a comparison of LCOE for different small scale wind turbines. From their results, it seems that “Vortex Tacoma” can be effective in low wind speed locations, where traditional horizontal and vertical axis turbines are not economically advantageous.

3.3. Energy harvesters based on transverse galloping

As for VIVs, many researcher explored the exploitation of galloping as a mechanism to harvest energy from fluid currents. Differently from VIVs, galloping is characterized by very large amplitude oscillation, and it only present an inferior limit in the wind speed range of operation.

Galloping-based energy harvesters have been presented in many configurations, and different bluff body sections. Often, the scheme followed is similar to the one reported in the Figure 3.8.

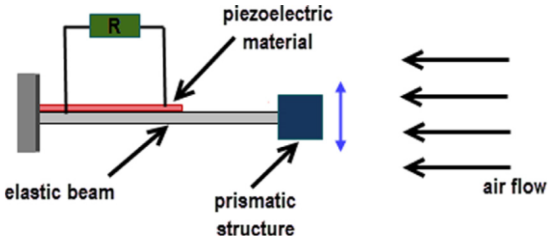

Figure 3.8. Example of galloping-based harvester configuration

An example of this configuration has been analyzed by Sirohi and Mahadik, who tested an equilateral triangular cross section prism (with 40 mm long sides) connected with two cantilever of dimensions 161 × 38 × 0.635 mm. They achieved a good power output of about 50 mW at a wind speed of 5.2 m/s. Interestingly, at slightly higher flow speeds the phenomenon extinguished, contrary to what the galloping theory says. In the opinion of the authors, it was caused by strong turbulence in the wind tunnel (Jayant Sirohi, 2011).

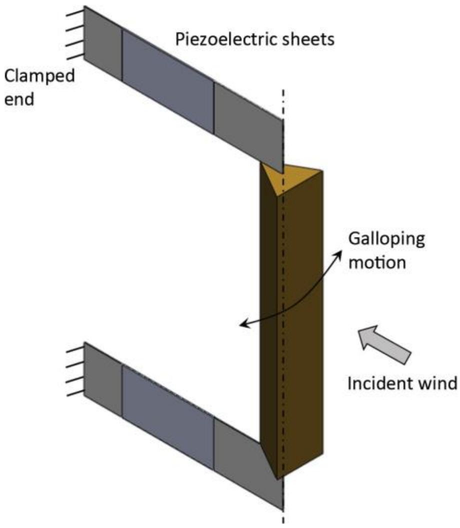

Figure 3.9 Scheme of galloping-based energy harvester with a triangular cross section *(Jayant Sirohi, 2011)*

Furthermore, a comparative study of prism different cross-sections effects on galloping has been carried out by Zhao, using the same configuration described before (L. Zhao, 2012). Among square, rectangle, triangle, and D-shape sections, the most suitable in order to maximize the instability was found to be the square one, which provided the lower cut-in speed too. Anyway, it is important to note that the different sections were compared maintaining constant all the other parameters (bluff body characteristic dimension, structural frequency and damping…), such that the "D" section was not even instable in the experimental conditions. However, in this study, a 40 mm side square bluff body, 150 mm long and mounted on a 150mm × 30mm × 0.6mm cantilever, was able to produce a peak power of 8.4 mW in correspondence of a 8 m/s wind speed.

In a different study, it was proven that galloping is sensitive to the flow condition and that turbulence can have effects on the behavior of different cross section bluff bodies. As an example, L. Zhao reported that turbulence in the flow can stabilize the square section, while it destabilizes the D-section (Liya Zhao, 2017). Also, Barrero-Gil analytically analyzed transverse galloping as a method for energy harvesting, showing how triangular and "D" section experience the instability at higher wind speed, other conditions being equal, but generate an higher power output once excited (Barrero-Gil, et al., 2010).

Moreover, in order to reduce the cut-in wind speed of galloping energy harvesters, L. Zhao also introduced a non-linearity in the system stiffness. Experimental results proved the effectiveness of the solution, achieving a cut-in speed of 1 m/s, and an overall enhancement of the power conversion in range from 1 to 4.5 m/s (L. Zhao, 2014).

To date, it has not been found any application of galloping in bigger size devices. The reason can be seen in the high amplitude of oscillation reached by the system once the instability occurs, together with the fact that both galloping and VIVs based energy harvesters present low efficiencies of a few percentage points, not comparable to those of traditional wind turbines.

3.4. Application of FIVs in water

The situation changes if applications of FIVs in water currents are considered. As a matter of facts, both VIVs and galloping based energy harvesters have been studied mainly in water flows.

One important example is given by VIVACE (Vortex Induced Vibration Aquatic Clean Energy), an energy conversion system patented by Michael M. Bernitsas, professor at the University of Michigan, and commercialized by Vortex Hydro Energy. The original scheme was quite simple, consisting in a horizontal cylinder free to oscillate in the vertical plane, and attached to a linear electromagnetic alternator (Bernitsas, et al., 2008). When the flow pass through the converter, the cylinder experiences the VIV phenomenon, and the kinetic energy extracted is transformed in

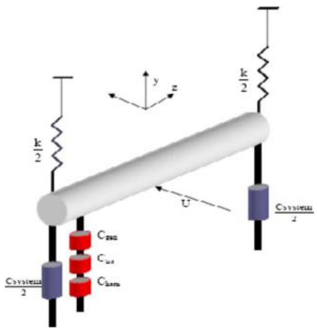

Figure 3.10 Scheme of VIVACE energy harvester
(Bernitsas, et al., 2008)

electrical power. However, differently from wind power applications, the VIVACE converter takes advantage from the different nature of the fluid and the sites where it can be installed.

First, VIVACE works in water flows, about 800 times denser than air and thus carrying a proportionally higher amount of power. Moreover, the density of the fluid is also convenient for the VIV phenomenon itself, since the amplitude of the motion has been found to be inversely proportional to the mass damping factor. This means that a bluff body will experience a more powerful oscillation when the product of the mass ratio for the damping factor is lower. Now, since the cylinder density can be easily lower than that of water, it means that a stronger damping can be exerted without negatively affecting the VIVs. Conversely, the same system needs lower damping, and electricity conversion, if working in air.

Moreover, the nature of sites where the technology can be installed is a big advantage with respect to wind power applications. As explained before, VIVs occur in a limited range of flow velocities, hence the system needs to be designed to match the right range of speeds in a site. Differently from wind, water flows such as river or ocean currents are characterized by a more constant speed, that is then easy to match with an accurate system design. Also, the direction of water flows is often constant, so the VIVACE converter does not need to adapt to directional variability as the wind power applications need to do.

Nevertheless, during the development of VIVACE converter many interesting results have been achieved in the study of different strategies to maximize the power density. Among others, the introduction of a specifically designed roughness on the cylinder surface (Che-Chun (Jim) Chang, 2011), made to exploit both VIVs and galloping phenomenon, and the study of the synergy between more cylinders positioned in a tandem arrangement have been analyzed and applied in the realization of the converter (Hai Sun, 2017).

The application of straight roughness strips on the cylinder surface, in certain range of angle position, has been found to partially suppress VIVs of the bluff body, while enhancing the galloping phenomenon over a threshold flow speed. Higher oscillation amplitude have been obtained and a wider range of flow speed has been exploited (Figure 3.11). Also the roughness height effects have been studied, assessing that it has not influence on the maximum amplitude of oscillations, but it promotes an earlier instauration of galloping.

Moreover, with the installation of two cylinders in tandem also a different fluid-structure interaction has been introduced: in facts, the tandem cylinders can experience both VIVs or galloping and *wake galloping.*

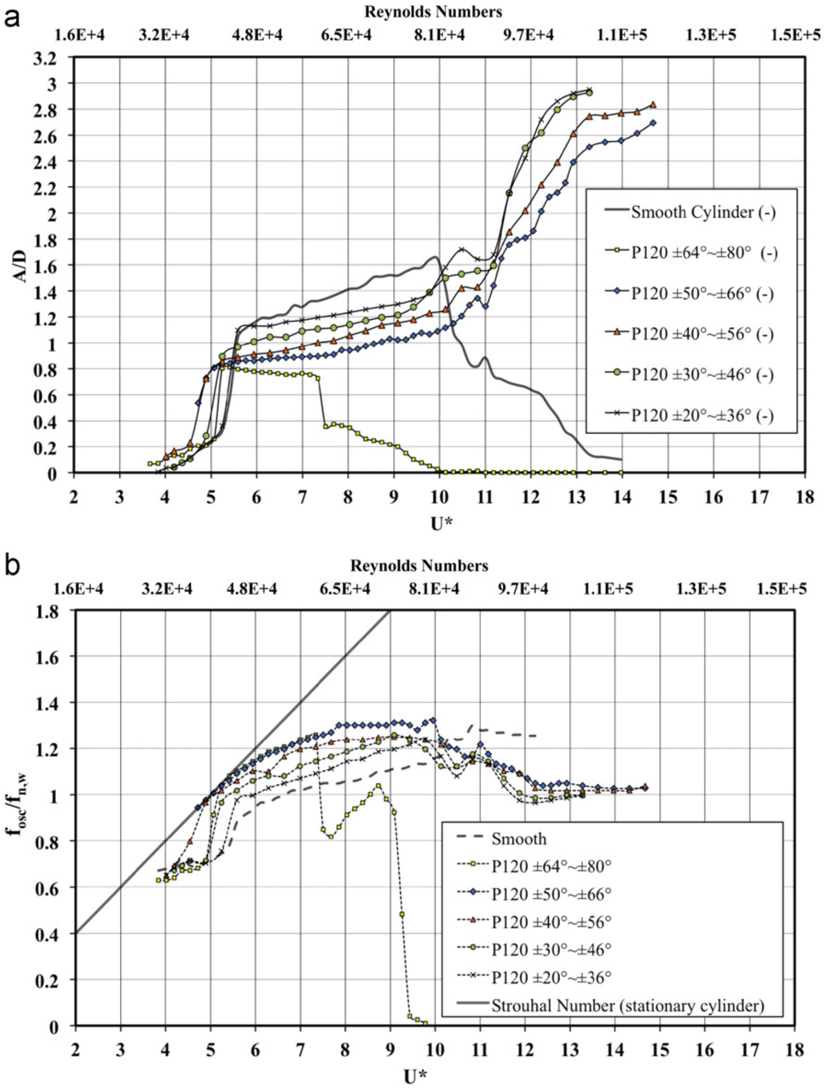

Figure 3.11 Effect of cylinder surface roughness on response amplitude and frequency *(Che-Chun (Jim) Chang, 2011)*

Wake galloping is a different kind of interaction between the structure and the vortices, in which, differently from VIVs, the elastic structure oscillates because of the vortices generated by an upstream bluff body. For instance, one configuration for wake galloping based energy harvesters consists in a piezoelectric “flag” deformed by the difference in pressure generated by the wake of a fixed upstream bluff body, as in the scheme in Figure 3.12 (Sebastian Pobering, 2008). With this configuration, the maximum efficiency was achieved when the piezoelectric vibrations synchronize with the wake vortices. The maximum power was 0.108 mW, achieved at the maximum wind speed of 45 m/s, hence very far from being competitive at a large scale.

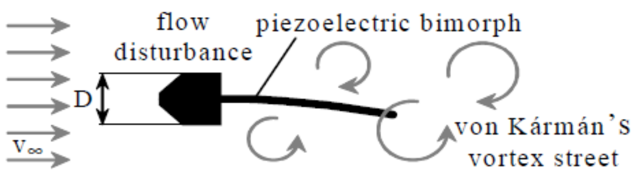

Figure 3.12 Wake galloping energy harvester concept *(Sebastian Pobering, 2008)*

On the other hand, in VIVACE concept also the upstream body is elastically mounted: interestingly, the experiments on tandem configuration reveal that both the upstream and downstream cylinder are affected (Figure 3.13). In the galloping range, the tandem disposition generates a synergic effect in such a way that the two cylinders harvest more than twice the power captured by a single cylinder

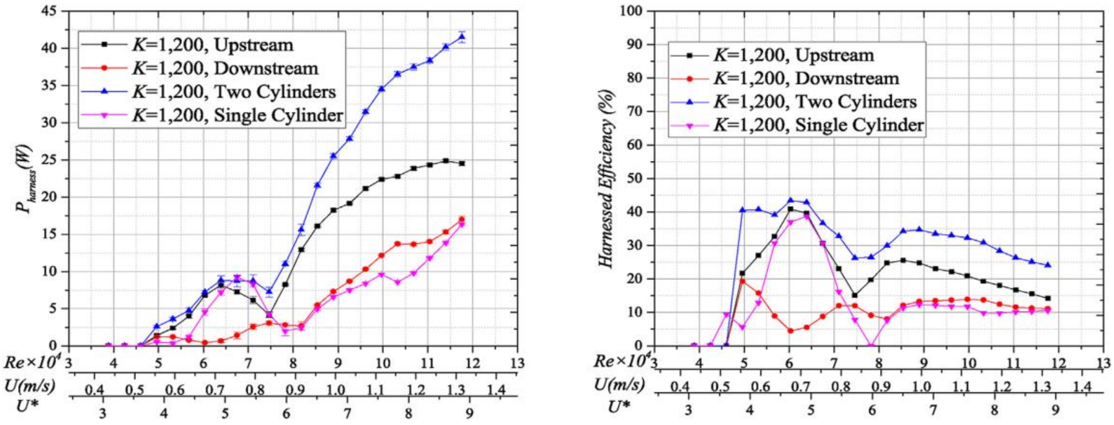

Figure 3.13 Harvested power and conversion efficiency of a single cylinder, compared to those of two tandem cylinders *(Hai Sun, 2017)*

in the same conditions. Interestingly, the major benefit in the power harvesting in the galloping range regards the upstream cylinder, which exhibits an increase up to 100% with respect to a single isolated cylinder. On the other hand, the downstream cylinder is almost unaffected by the synergy. In the VIVs range, both the upstream and the downstream benefit from the tandem configuration.

Another interesting solution for FIVs-based energy harvesting in water has been analyzed by Hamid Arionfard, who focused on the dynamics of pivoted cylinders in different configurations (Arionfard, 2018).

First, Arionfard studied the behavior of a single cylinder in two configurations: pivoted at the upstream and downstream (Figure 3.14). Results show that the downstream pivot layout achieved higher oscillation amplitudes and power output, since the drag force acts accordingly to the lift force, adding an elastic instability to the system, while in the other configuration the drag force has a stabilizing effect on the motion. The experimental tests show that a 30 mm diameter and 180 mm length polypropylene cylinder could generate a maximum power of about 0.06 W in the downstream-pivoted configuration.

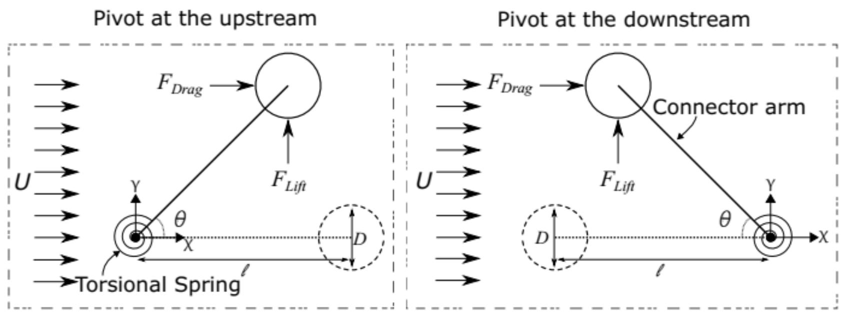

Figure 3.14 Upstream and downstream configuration of pivoted cylinder for VIV energy harvester *(Arionfard, 2018)*

However, the main part of the research focused on the behavior of two mechanically coupled pivoted circular cylinder. The circular cylinders are free to rotate around a pivot in different arrangements including: both cylinders on the downstream, both on the upstream and a cylinder on each side of the pivot point.

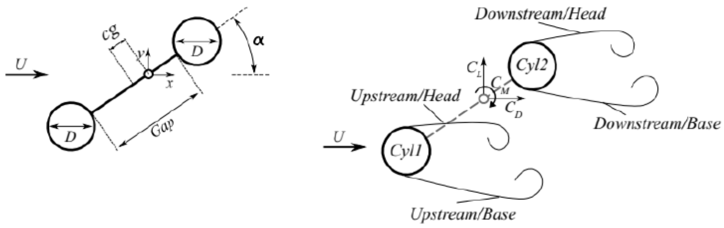

Figure 3.16 Energy harvester concept based on two pivoted cylinder in tandem and mechanically coupled *(Arionfard, 2018)*

It was found that different fluid dynamic phenomenon occurred depending on the configuration, as reported in the Figure 3.15. The cylinders experience flutter if both located on the upstream of the pivot (CG < 0) and the gap ratio (G=gap/D) between them is around zero. Vortex excitation is observed in two configurations and referred to as vortex induced vibration (VIV) and synchronized vibration (SV). VIV occurs when both cylinders are located on the downstream of the pivot while the gap is zero and SV occurs when the center of gravity is on the pivot (CG = 0) and the gap ratio between cylinders is G>3.9. If one cylinder is located on the center of the rotation and the other cylinder is on the downstream (CG > 0), wake induced vibration (WIV) takes place. While for G<1.4 the response is a typical wake galloping, for G>1.4 two vibration modes are recognizable as 'combined vortex resonance and galloping'. For all configurations with G>0, gap switching induced vibration (GSIV) is observed specially for 1.9<G<2.4. However, GSIV is the dominant mechanism of vibration if the center of gravity is on the pivot point (CG = 0). In cases where CG is not close to zero, the drag force may enhance the vibration, if the Reynolds number is not large enough to suppress the motion.

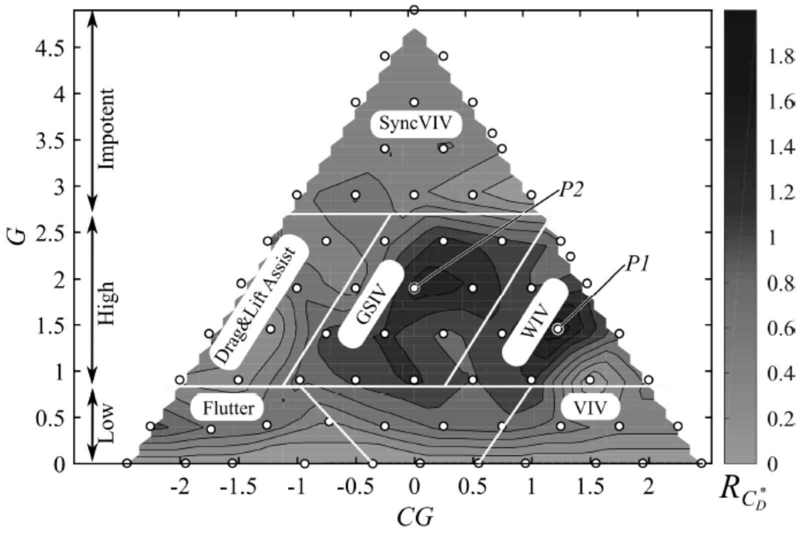

Figure 3.15 Classification of different Flow-induced interactions experienced by two mechanically coupled cylinder, depending on the pivot position and distance from bluff bodies *(Arionfard, 2018)*

3.5. Overall comments on the state of the art

Different fluid-structure interactions and configuration have been investigated as alternative mechanisms to convert wind or water current power into electric energy. Generally, the structure layouts present similar features, but their behavior and performance can vary significantly, depending on vibration mode, structural parameters and size.

As reported, none of the presented systems presents high power production. Also, referring to other recent literature review on the topic, it is clear that FIVs-based energy harvesters are generally characterized by low conversion efficiency, as it is traditionally defined for turbines:

$$\eta = \frac{absorbed\ power}{available\ power\ throgh\ the\ swept\ area} \tag{3.1}$$

Nevertheless, many researcher claimed that the traditional definition of efficiency could be inappropriate to evaluate such systems, and proposed other performance indicators. Clearly, the ideal indicator would be the energy cost, expressed by the levelized cost of energy (LCOE), which takes into account initial investment and the operational and maintenance costs to assess the actual economic profitability. Unfortunately, such an indicator is almost impossible to evaluate for preliminary design and concept proposals, thus other parameters need to be considered.

One alternative has been found in the power density, defined as the ratio between the produced power and the occupied volume or surface.

$$\delta = \frac{absorbed\ power}{occupied\ volume\ or\ surface} \tag{3.2}$$

In facts, both VIVACE and Arionfard studies on wake galloping and VIVs interactions in water aimed to assess the power density potential of FIVs energy harvesters as an important parameter to measure the system performance.

In this direction, also Vortex Bladeless design is characterized by a great effort to reduce operation and maintenance costs: in their view, the significant reduction of maintenance costs, together with the ease of installation, may lead to a sort of “plug-in” device, able to be competitive in the distributed power generation market.

It is also important to note that wind energy harvesters need to deal with wind variability, both in magnitude and direction. Again, Vortex Bladeless design seems to fit its mission, quickly adapting to wind variations.

Finally, it is clear from the literature review that the majority of low power harvesters make use of piezoelectric power generators, mostly because of their low cost and ease of integration in oscillating systems. However, it is interesting how higher power devices usually rely on electromagnetic conversion: in this case, the main reason seems to be related to the higher durability of such converters.

4. VIVs - Parametric analysis

In the following, are explained the motivation behind the selection of a particular mathematical model to describe the VIVs phenomenon and estimate its potential as a wind energy harvesting mechanism.

Starting from the analysis of the dimensionless form of the model, the effect of reduced mass and damping ratio values on the VIVs energy harvester performance are assessed in terms of conversion efficiency.

Then, using the dimensional form of the model, also other performance indicators, such as the encumbrance and the power density are evaluated, considering the effect of varying the system stiffness and damping to optimize the output.

4.1. Mathematical model – Wake oscillator model

Since the time when Hartlen and Currie first proposed the wake oscillator coupled model, many researchers have given their contribution in making it more accurate. Among the others, Facchinetti analysed the effect of different coupling terms representing the structure feedback in the wake oscillator equation, comparing position, velocity and acceleration coupling, namely Ay, $A\dot{y}$ and $A\ddot{y}$. He identified the acceleration coupling as the most suitable in VIVs (Facchinetti, et al., 2004), presenting the model in the form:

$$\begin{cases} m\ddot{y} + c\dot{y} + ky = \frac{1}{2}\rho U^2 D C_L \\ \ddot{q} + \varepsilon\omega_f(q^2 - 1)\dot{q} + \omega_f^2 q = A\ddot{y} \end{cases} \tag{4.1}$$

The modal mass term m contains both structural and added mass, which for circular cylinder coincide exactly with the displaced fluid mass, while the damping term contains the mechanical, electromechanical and fluid-added damping contributes, the last of which depends a stall term γ, function of the drag coefficient:

$$m = m_s + m_a \tag{4.2}$$

$$m_a = \rho\pi\frac{D^2}{4} \tag{4.3}$$

$$c = c_s + c_{em} + c_f \tag{4.4}$$

$$c_f = \gamma\omega_f\rho D^2 \tag{4.5}$$

$$\gamma = \frac{C_D}{4\pi S_t} \tag{4.6}$$

In Facchinetti work, the stall term was considered as a constant in order to reduce the system non-linearity and obtain an approximated analytical solution. In more recent works, however, the magnification effect of the structure motion on lift and drag coefficients is taken into account. Moreover, there are examples of models built to take into account both cross-flow and in-line structural motion, giving a more complete description of the dynamic behaviour. As a drawback, those models need to introduce more experimental and semi-empirical parameters, which complicate their adoption in the design stage of an energy harvester, as it will be explained in the following.

Considering these aspects, together with the fact that in the context of this work it is important to reduce the complexity of mathematical modelling in order to obtain a straightforward design method, it has been chosen to adopt the modified wake oscillator model proposed by Srinivasan. This model, which was originally meant to reproduce the two degree of freedom dynamic of VIVs, gives accurate results when restricted to a single degree of freedom case, taking into account the magnification effect of transverse motion on lift and drag (Srinivasan, et al., 2018).

$$\begin{cases} ml\ddot{y} + \left(c_s + c_e + \gamma\omega_f\rho D^2\right)\dot{y} + ky = \frac{1}{2}\rho U^2 DlC_L \\ \ddot{q} + \varepsilon\omega_f(q^2-1)\dot{q} + \omega_f^2 q = A\ddot{y} \end{cases} \tag{4.7}$$

Introducing the following dimensionless parameters, some of which has been already defined in chapter 1,

Structure natural frequency	$\omega_n = \sqrt{\frac{k}{ml}}$	Damping ratio	$\zeta = \frac{c_s + c_{em}}{2ml\omega_n}$
Reduced displacement	$Y = \frac{y}{D}$	Reduced mass	$m_r = \frac{m}{\rho D^2}$
Reduced velocity	$U_r = \frac{U}{f_n D}$	Reduced angular frequency	$\delta = \frac{\omega_n}{\omega_f} = \frac{1}{U_r S_t}$

and changing the time scale from t to the *wake-based time scale* $\tau = \omega_f t$, the equations become:

$$\begin{cases} \ddot{Y} + \left(2\zeta\delta + \frac{\gamma}{m_r}\right)\dot{Y} + \delta^2 Y = Mq \\ \ddot{q} + \varepsilon(q^2-1)\dot{q} + q = A\ddot{y} \end{cases} \tag{4.8}$$

Where:

$$\gamma = \frac{C_{D0}}{4\pi S_t}\sqrt{1 + \left(2\pi S_t \dot{Y}\right)^2} \tag{4.9}$$

$$M = \frac{C_{L0}}{2}\frac{1}{8\pi^2 {S_t}^2 m_r}\sqrt{1 + \left(2\pi S_t \dot{Y}\right)^2} \tag{4.10}$$

It is important to note that VIVs phenomenology depends on a long list of fluid and structure parameters, starting from flow regime and fluid viscosity, to structure mass, damping and superficial roughness, which have a strong effect on the system response and are often interrelated. Hence, even if the presented coupled model aim to give a sufficiently simplified tool to analyse VIVs, they still contains many experimental parameters, which depend on the flow regime and the dynamic properties of the structure. Consequently, this feature make it difficult to use them during the preliminary design phase of an energy harvester, which is for its own nature antecedent to any experimental activity.

Starting from the Strouhal number, S_t, many parameters depend on the Reynolds number. As it was already described in Chapter 2, S_t is almost constant over a wide range of Reynold number (from about $5 * 10^2$ to 10^5) where it is approximately equal to 0.2. Furthermore, also static lift and drag force coefficients, C_{L0} and C_{D0}, depend on the Reynolds number: as for S_t, they can be evaluated from static experimental measurements and averaged over a range of Re.

Finally, the wake oscillator equation contains two semi-empirical parameters, ε and A, which do not have a measurable physical meaning and need to be tuned fitting experimental results. Many authors dealing with the wake oscillator model took as reference the values proposed by Facchinetti ($\varepsilon = 0.3$ and $A = 12$) deduced in such a way to fit a wide set of experimental data available from literature. However, experimental results are sometimes very different from the prediction made using those semi-empirical values, as they should be tuned depending on the different experimental condition. Thus, it is a key factor to find proper values for the two semi-empirical parameters, in order to use the wake oscillator model in the preliminary design of energy harvesters.

As demonstrated by Govardhan and Williamson, VIVs response strongly depends on the mass-damping parameter $m_r\zeta$ and the Reynolds number. Their experiments show how systems characterized by the same value of reduced mass and Reynold number, but different damping ratio and thus different $m_r\zeta$, present very different response shape (Figure 4.1): while low mass-damping systems are characterized by three branches in their response (initial, upper and lower), higher mass-damping system only show two of them (initial and lower), with corresponding lower amplitudes (Govardhan & Williamson, 2006).

From this point of view, it seems very important to tune the semi-empirical parameters of the coupled model on experiments made in appropriate range of Reynolds and mass-damping. To this end, it was chosen to take as a suggestion the optimal value of mass-damping for VIVs-based energy harvesters found by Barrero-Gil: in facts, by analysing a simple forced model he found that the best energy harvesting efficiency can be obtained for $m_r\zeta = 0.2$ (Barrero-Gil, et al., 2012). Thus, comparing this value with the experimental results from Govardhan and Williamson in Figure 4.1, it is clear that it falls within the range in which the response presents all three branches of amplitude.

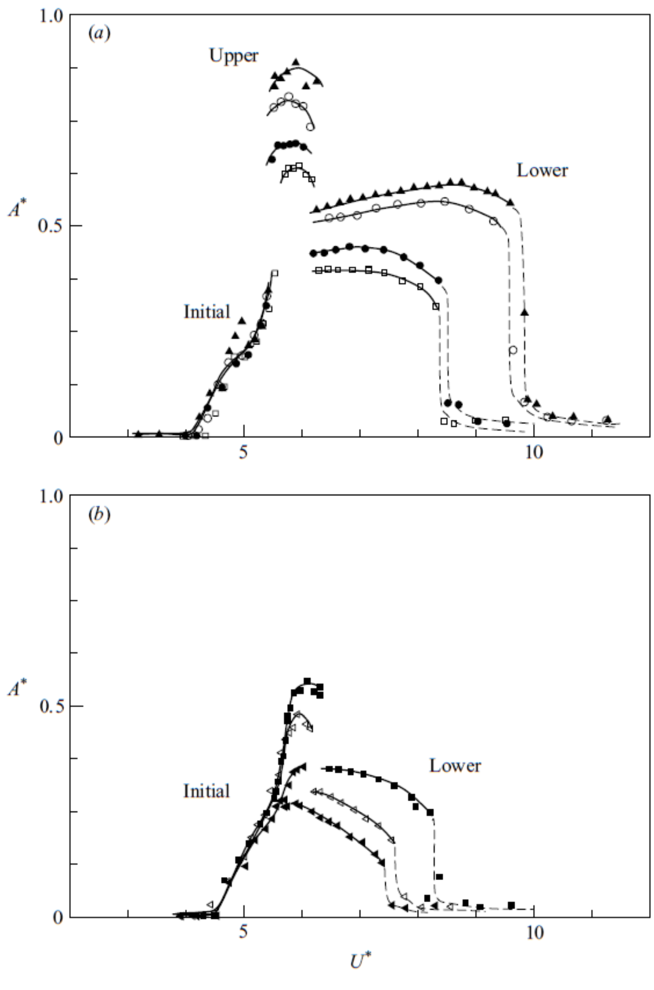

Figure 4.1 semi-amplitude response of a elastically mounted cylinder experiencing VIVs. The amplitudes curves are referred to different values of reduced mass. As the reduced mass decreases, the semi-amplitude grows. *(Govardhan & Williamson, 2006)*

Unfortunately, since the majority of the experiments on VIVs in air are made in order to investigate civil engineering applications, they are usually characterized by very high reduced mass and low damping ratios values, which are significantly different conditions from those expected for an energy harvester.

As a result, in the context of this work, the best choice has been to select a set of parameters tuned on water experiments in similar ranges of Reynolds, reduced mass and damping ratio to those that are realistically expected. The selected parameters come from Ogink and Metrikine work on a modified wake oscillator model (Ogink & Metrikine, 2010): in the paper, the parameters have been tuned on Khalak and Williamson experiments, made in a reduced mass range of 5 to 20, and mass-damping of about 0.02 (Khalak & Williamson, 1999). Moreover, also Franzini chose the same parameters in a similar work on piezoelectric energy harvester (Franzini & Bunzel, 2018), obtaining a good matching between his experimental data and the simulation results.

In the following, it is reported the whole set of parameters used as a reference in this work, and the comparison between experimental data and numerical simulation in two conditions of reduced mass and damping ratio, showing an overall good fitting (Figure 4.2). It is important to note that two set of semi-empirical parameters have been selected: the first for simulating the initial and upper branch, and the second for the lower branch.

$C_{D0} = 1.1856$	$C_{L0} = 0.3842$	$S_t = 0.1932$
Upper branch ($U_r < 5.5$)	$A = 4$	$\varepsilon = 0.05$
Lower branch ($U_r > 5.5$)	$A = 12$	$\varepsilon = 0.7$

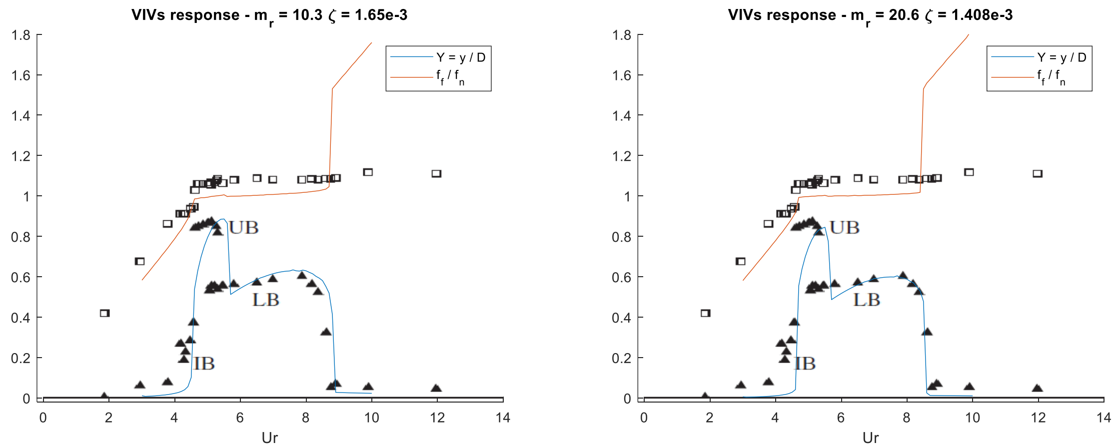

Figure 4.2 Comparison between experimental data from *(Govardhan & Williamson, 2006)* and numerical results obtained with the present model.

4.2. Numerical solution and methodology

The system of coupled non-lineal differential equations has been solved through the Runge-Kutta method of 4th order, for each value of crescent reduced velocity, in the range from 3 to 10.

Initial conditions for the first iteration have been set following the same method as Facchinetti:

$$Y_0 = 0 \qquad \dot{Y}_0 = 0 \qquad \ddot{Y}_0 = 0 \qquad q_0 = 2 \qquad \dot{q}_0 = 0$$

For each step of reduced velocity, the equations are solved over a time range sufficiently long to obtain a steady state response, set equal to 400 second. Is to be noted that shorter periods of simulation give overall similar results, but present some differences in the transition regions at the edge of the lock-in range.

The final conditions obtained at the end of each reduced velocity step are then set as the initial condition for the subsequent step. For each reduced velocity step, maximum amplitude, frequency response and the maximum value of the wake variable q have been recorded.

The main outcomes of the analysis of VIVs dimensionless model consist in the evaluation of the normalized semi-amplitude response $Y = y/D$, which comes directly from the numerical resolution, and the efficiency of conversion, calculated from the equation.

$$\eta = \frac{absorbed\ power}{available\ power\ throgh\ the\ swept\ area} = \frac{\frac{1}{T}\int_0^T c\dot{y}^2 dt}{\frac{1}{2}\rho U^3 (2y+D)l} \tag{4.11}$$

In this case, in order to compare the performance with the Betz limit, we refer to the fluid-dynamic conversion efficiency, and the absorbed power is set equal to the power dissipated from both mechanical and electromechanical damping, and the efficiency can be expressed as:

$$\eta = \frac{\frac{1}{T}\int_0^T (c_s + c_{em})\dot{y}^2 dt}{\frac{1}{2}\rho U^3 (2y+D)l} \tag{4.12}$$

Introducing the dimensionless parameters listed in the previous table, the equation becomes:

$$\eta = 4(2\pi)^3 \frac{m_r \zeta}{U_r^3 \delta^2} \frac{1}{(2Y+1)} \frac{1}{\Gamma} \int_0^\Gamma \dot{Y}^2 d\tau \tag{4.13}$$

For each reduced velocity step, the conversion efficiency has been calculated over five complete oscillations in order to obtain an average value.

In case one might be interested in the effective conversion into electrical power, it would be necessary to exclude the mechanical damping term, c_s, from the equation. Anyway, the result obtained would be qualitatively the same, since the mechanical damping component can be assumed as a constant, and the electromechanical conversion efficiency would become:

$$\eta_{em} = \frac{\zeta_{em}}{\zeta}\eta = \frac{\zeta - \zeta_s}{\zeta}\eta \tag{4.14}$$

4.3. Dimensionless analysis - Results

In Figure 4.3, Figure 4.4 and Figure 4.5 are reported the normalized amplitude and the conversion efficiency of the system for a given reduced mass and different values of damping ratio, which is proportional to the conversion intensity.

First, in all the figures it is clear that the maximum amplitude response and conversion efficiency happen at the same reduced velocity, equal to 5.2 .

As it can be noticed, if the damping is very small, the system experiences the highest amplitude response, but the efficiency of conversion is really low: in this case, just a few of the energy absorbed from the flow is really converted into electricity, while the system exploits the captured energy to increase its kinetic energy. On the other hand, if the damping ratio is too high, the system response is too damped and there is not a significant energy transfer from the fluid flow to the mechanic system. As a result, even if a bigger portion of the captured energy is converted into electricity, the total amount is too small and the same is true for the power output. Therefore, it seems that there exists an optimal value of damping ratio that maximizes the efficiency of conversion for every value of reduced mass.

In Figure 4.6, it has been reported the maximum value of the conversion efficiency for each set of reduced mass and damping ratio values. As it can be seen, the maximum value of the efficiency does not change significantly from one case to another. However, a smaller reduced mass determines a more moderate slope in the efficiency trend as a function of the damping ratio, while higher values of m_r are characterized by a shorter range of optimal energy conversion.

Interestingly, if the maximum efficiency values are expressed as a function of the mass-damping parameter, a perfect collapse occurs, as in Figure 4.7: as found by Barrero-Gil, the optimal value of the mass.damping parameter is around 0.2. Moreover, the maximum efficiency is found to be around 5.4%, which is significantly lower that any traditional wind turbine: however, as explained in the previous chapters, the conversion efficiency is not the only performance parameter to be considered, in particular if the energy harvester is meant to aliment off-grid electronic devices and sensors.

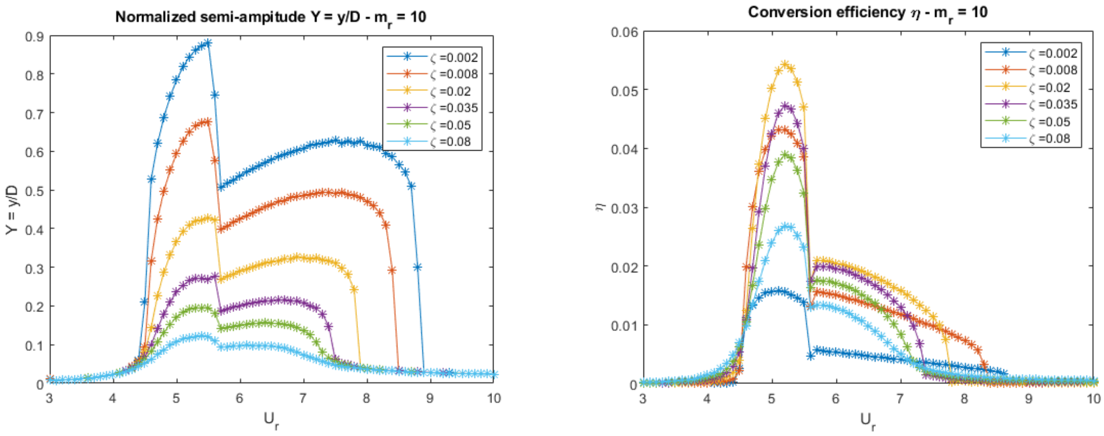

Figure 4.3 Normalized response semi-amplitude and conversion efficiency of a cylinder experiencing VIVs. $m_r = 10$

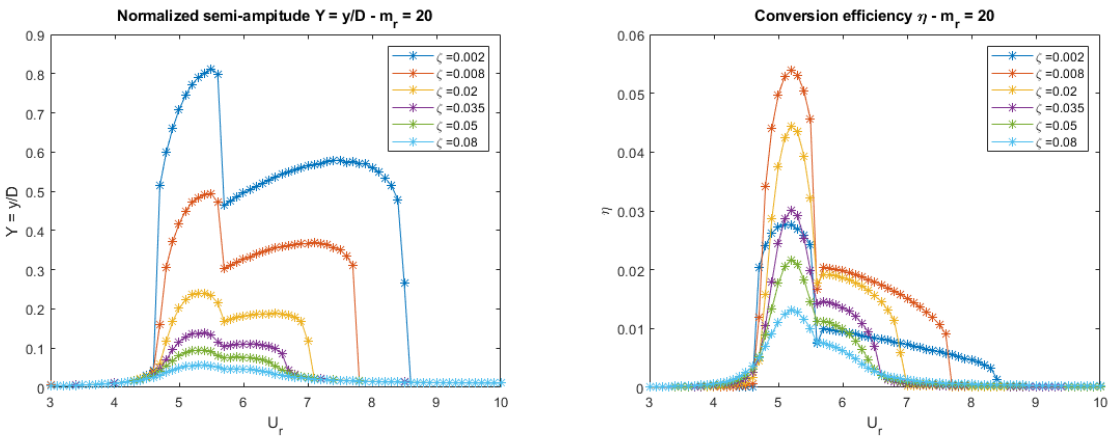

Figure 4.4 Normalized response semi-amplitude and conversion efficiency of a cylinder experiencing VIVs. $m_r = 20$

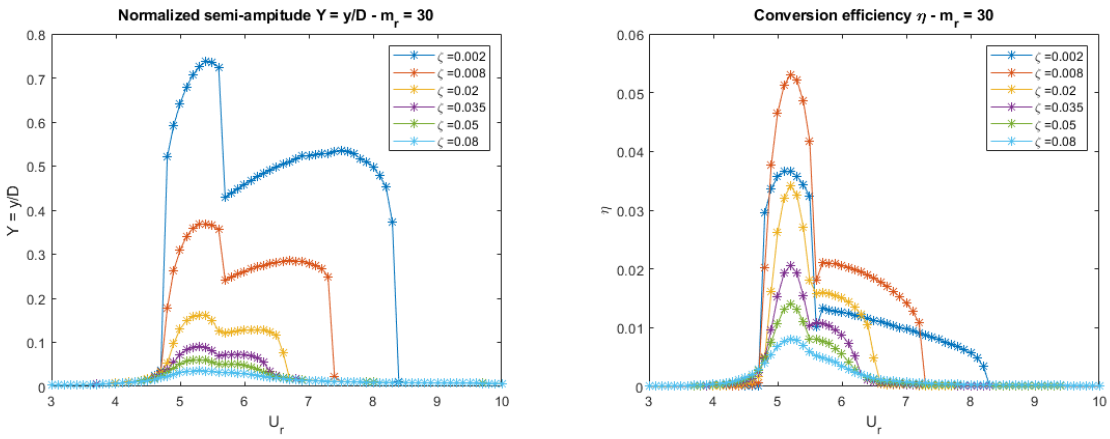

Figure 4.5 Normalized response semi-amplitude and conversion efficiency of a cylinder experiencing VIVs. $m_r = 30$

It is important to note that even if it does not affect the maximum efficiency, the reduced mass value should be maintained as small as possible. As seen from the results, an high reduced mass produces a shorter range of wind speed in which the conversion is maximized. Moreover, looking at the amplitude responses reported in the figures for different values of m_r, it is clear that lower values determine higher amplitudes: this has an important effect if one consider the power output instead than the efficiency, since the produced power is proportional to both the efficiency and the swept area.

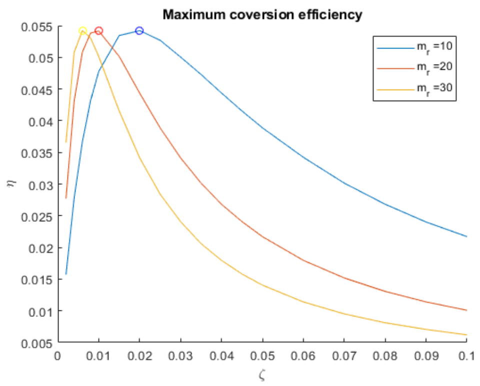

Figure 4.6 Maximum efficiency for each value of damping ratio

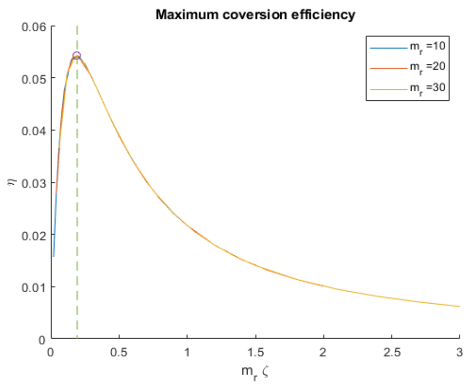

Figure 4.7 Maximum efficiency as a function of mass-damping parameter

4.4. Design of dimensional parameters

VIVs energy harvesters needs reduced mass values as low as possible. Unfortunately, in air, structure present higher values of m_r than in water, and this is the main reason because of which in literature, we found moderately large scale energy harvesters only in water.

Assuming that the bluff body is a hollow cylinder, the thickness of which is proportional to the diameter, ($\frac{s}{D} = cost$), it is possible to express the reduced mass as function of the ratio between structural material and air densities, thus independent from the diameter. Moreover, the value obtained from expression is increased by the 10% in order to consider the inertial contributes of all the components of the system.

$$m_r = \frac{1.1\left(\pi D s\rho_s + \pi\frac{D^2}{4}\rho_{air}\right)}{\rho_{air}D^2} = 1.1\pi\left(\frac{s}{D}\frac{\rho_s}{\rho_{air}} + \frac{1}{4}\right) \quad (4.15)$$

Obviously, both the ratios, $\frac{s}{D}$ and $\frac{\rho_s}{\rho_{air}}$, depend on the particular material used. Consequently, given a structural configuration and the selected material, the reduced mass should be almost univocally determined. From literature, it is possible to assess that typical values of reduced mass for an energy harvester can be between 10 and 80. In the following, we will consider a reduced mass equal to 15.

The subsequent step in the VIVs-base energy harvester design is to accurately choose the diameter and the natural frequency of the structure. As it was explained in the theoretical chapter about VIVs and seen from the dimensionless model analysis, the system is able to harvest a significant amount of power in correspondence of the lock-in region, and in particular it works with the best efficiency near the exact resonance response, at a reduced velocity equal to 5.2 .

At this point it is important to note there are two cases that needs to be analysed:

1. all the parameters of the system are kept fixed,
2. it is possible to control the system's stiffness and damping in order to adapt to each operational condition, optimizing the power output.

4.4.1. Case 1. Fixed parameters

In the case all the design parameters are kept constant, the choice of diameter and frequency requires the definition of a design condition for wind speed, which comes from the wind assessment of each particular site. Usually, the design wind speed does not coincide with the mean value of wind speed measures in a site, but it is a little higher. This is because the power carried by a wind flow depends on the cube of the flux speed, so that higher wind speed, even if not so frequent, would carry a bigger portion of the total energy amount of a given site. In the context of this chapter, the design wind speed will be set equal to 5 m/s.

As a result, the relation that design diameter and frequency should respect can be obtained from the definition of reduced velocity.

$$f_n D = \frac{U}{U_r} = \frac{5}{5.2} = 0.96\ \left[\frac{m}{s}\right] \quad (4.16)$$

Thus, the designer is free to select a particular diameter and consequently determine the necessary natural frequency of the structure. However, a larger value of diameter will provide higher swept area, and thus a higher amount of power from which to extract energy. On the other hand, big diameters will also determine large occupied volumes, which could result as a drawback in the power density evaluation.

For a given diameter size, it is possible to estimate the modal mass, and frequency, hence the system's stiffness.

$$m = 1.1\pi D^2\left(\frac{s}{D}\rho_s + \frac{1}{4}\rho_{air}\right) = m_r\rho_{air}D^2 \quad (4.17)$$

$$f_n = \frac{U}{U_r D} = \frac{0.96}{D} \quad (4.18)$$

$$k_{opt} = {\omega_n}^2 ml = (2\pi f_n)^2 ml \quad (4.19)$$

Then, it is also possible to calculate the system damping from the optimal value of mass-damping found in the previous paragraph.

$$\zeta_{opt} = \frac{(m_r\zeta)_{opt}}{m_r} = \frac{0.2}{m_r} \tag{4.20}$$

$$c_{opt} = 2\omega_n \zeta_{opt} ml \tag{4.21}$$

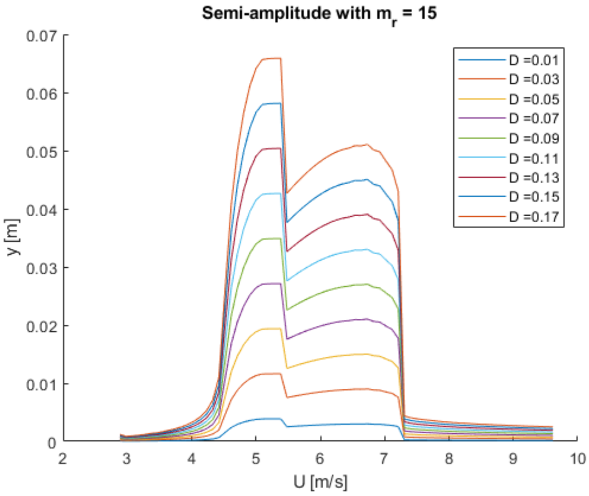

Figure 4.8 Response semi-amplitude calculated for different value of cylinder diameter

Figure 3.15 shows the response semi-amplitude calculated for different value of cylinder diameter, considering a bluff body length of 1 m. In order to obtain sufficiently reliable results, the diameter measure considered do not exceed 0.17 m, which is chosen in order to maintain an aspect ratio $\frac{l}{D}$ bigger than 6.

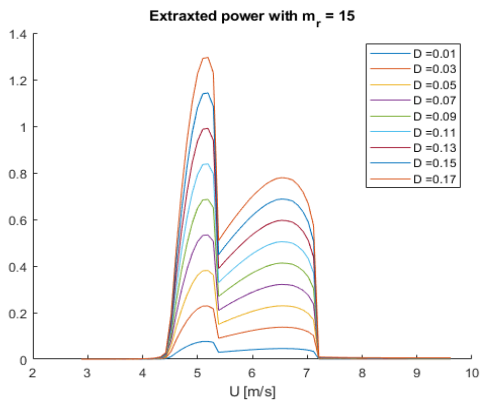

Figure 4.10 Mechanical power [W] absorbed by the system

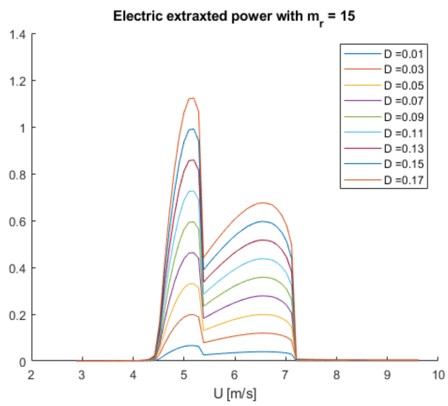

Figure 4.9 Electrical power [W] converted by the system

The power absorbed by the structure, and the actual power converted into electricity will be:

$$P_{F-B} = \eta P_{wind} = \eta \frac{1}{2}\rho U^3(2y + D)l \tag{4.22}$$

$$P_{em} = \eta_{em} P_{wind} = \eta_{em} \frac{1}{2}\rho U^3(2y + D)l = \frac{\zeta - \zeta_s}{\zeta} \eta \frac{1}{2}\rho U^3(2y + D)l \tag{4.23}$$

Where the mechanical damping ratio ζ_s, mainly due to friction, is estimated as equal to 0.002 by referring to similar structures in the literature.

4.4.2. Case 2. Tuned parameters

Controlling the conversion system, it is possible to tune the value of the electromechanical stiffness and damping, influencing the system's response. As said, the maximum conversion is achieved when there's a match between the vortex shedding and the system natural frequency: thus in theory, by changing the system stiffness proportionally to the wind speed, it would be possible to amplify the range of lock-in, and maintain the system in the optimal condition for power conversion.

Then, the system's frequency and stiffness would be a function of the wind speed:

$$f_n(U) = \frac{U}{U_r D} = \frac{U}{5.2\ D} \tag{4.24}$$

$$k_{opt}(U) = {\omega_n}^2 ml = (2\pi f_n)^2 ml \tag{4.25}$$

It is important to note that just changing the system frequency will extend the lock-in region, but without adapting the damping value to the new frequency, the system would quickly become too damped if the wind speed descends, or too little damped if the wind speed grows.

Consequently, while the optimal damping ratio, being function only of the reduced mass, remains constant, the optimal system damping needs to be determined as a function of the wind speed, since depends on the angular frequency:

$$c_{opt}(U) = 2\omega_n \zeta_{opt} ml \tag{4.26}$$

Actually, the value of c assumed by the system cannot decrease under the mechanical damping value: as a result, there is a minimum wind speed, below which the system will not be able to produce electrical power.

In the following figures it is reported the system response and performance obtained by adapting stiffness and damping to the wind speed.

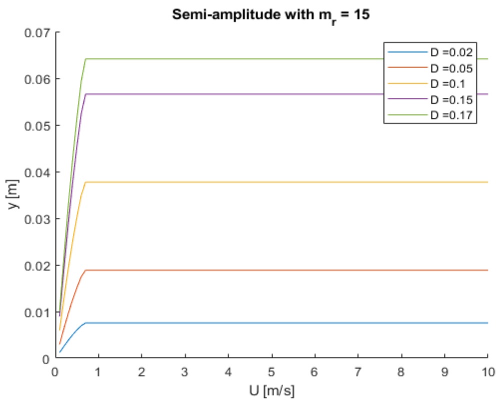

Figure 4.12 Response amplitude for different cylinder diameters, with varying stiffness and damping

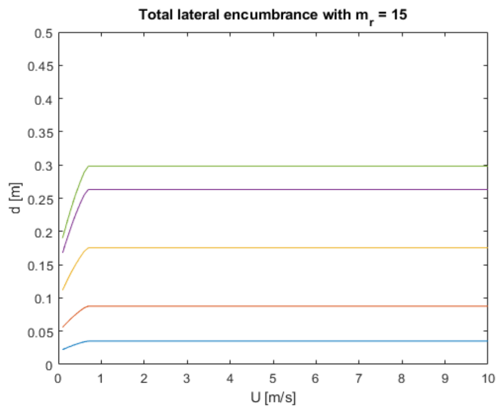

Figure 4.12 Total lateral encumbrance of the oscillating cylinder

An important feature of the response is that the oscillations amplitude remains constant in all wind speed conditions, as well as the conversion efficiency, while absorbed mechanical power consequently increases with the wind speed.

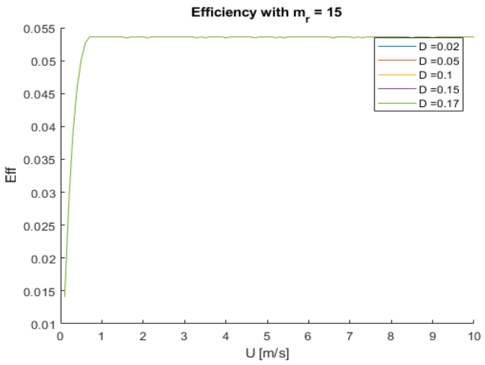

Figure 4.14 Conversion efficiency with varying stiffness and damping

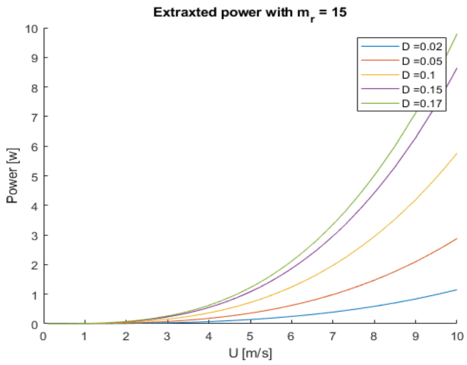

Figure 4.14 Mechanical power absorbed by the system, with varying stiffness and damping

5. Galloping - Parametric analysis

5.1. Mathematical model – Pseudo-static approximation

As explained in introductory chapters, transverse galloping is a fluid-structure interaction found in an intermediate range of reduced velocity U_r, in which the appearance of a transversal motion of a bluff body determines a further exchange of energy from flow to structure, which makes the system unstable.

The basic assumption on which the galloping mathematical models is built on is the pseudo-static aeroelasticity approximation validity. It describes fluid-structure interactions in which flow and body dynamics are such that the body velocity can't be neglected with respect to the fluid speed, but it can be considered "frozen in time" while it comes to solve the fluid dynamic of the system. As mentioned in introductory chapter on galloping, such approximation is usually considered valid if the reduced velocity is higher than a specific lower limit, whose value is still debated. According to Blevins, the minimum value of reduced velocity to adopt the pseudo-static approximation is 10, but the model becomes increasingly accurate as the reduced velocity grows (Païdoussis, et al., 2011).

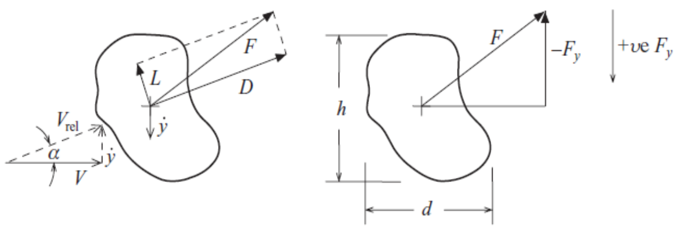

Figure 5.1 Change of the angle of attack due to transverse motion *(Païdoussis, et al., 2011)*

Considering an elastically mounted body with a general transverse section, moving transversely to the flow with a not negligible velocity, as reported in Figure 2.10, the dynamic equation of the system is:

$$ml\ddot{y} + c\dot{y} + ky = \frac{1}{2}\rho {U_{rel}}^2 Dl[-C_L\cos(\alpha) - C_D\sin(\alpha)] \quad (5.1)$$

Following the same notation as in the case of VIVs, the modal mass term m contains both structural and added mass, but in this case, the added mass coefficient is different for each kind of section. The modal damping and stiffness are the sum of mechanical and electromechanical contributes.

$$m = m_s + m_a \quad (5.2)$$

$$m_a = C_a \rho \pi \frac{D^2}{4} \quad (5.3)$$

$$c = c_s + c_{em} \quad (5.4)$$

$$k = k_s + k_{em} \quad (5.5)$$

As mentioned, the angle of attack is a function of both fluid and structure transverse speed,

$$\tan(\alpha) = \frac{\dot{y}}{U} \tag{5.6}$$

C_L and C_D are the fluid-dynamic lift and drag force coefficients, whose values are a function of the section shape and the angle of attack, and consequently of the transverse velocity of the body. Thanks to the pseudo-static approximation, lift and drag force coefficients can be evaluated from static tests, and used to calculated the fluid load on the structure at each time step.

Many researchers simplified the notation of the problem by expressing the overall effect of lift and drag in the transverse direction through the definition of a transverse force coefficient, C_{Fy} (Figure 5.3). Moreover, they used a polynomial fit to approximate the experimental data and obtain an expression easy to handle.

$$C_{Fy} = [-C_L\cos(\alpha) - C_D\sin(\alpha)] = a_0 + a_1\alpha + \cdots + a_n\alpha^n \tag{5.7}$$

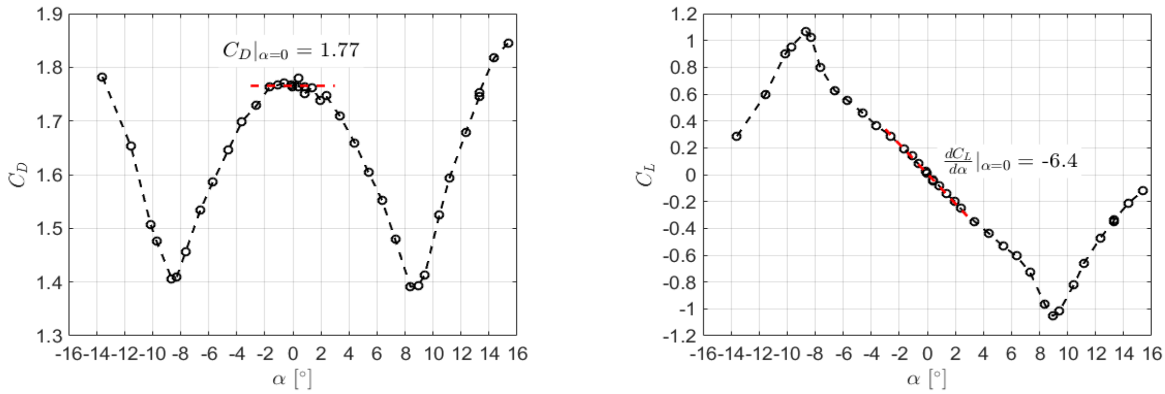

Figure 5.2 Experimental measurements of drag and lift force coefficients for a rectangular cross section *(Mannini, et al., 2018)*

As reported by Païdoussis, the best cohesion between numerical simulation and experimental data should be obtained with a seventh degree polynomial fit (Païdoussis, et al., 2011). However, Barrero-Gil used a third degree polynomial to fit the experimental values of C_{Fy} and obtained analytical expressions to evaluate the efficiency of transverse galloping in energy harvesting (Barrero-Gil, et al., 2010). In his work, he identify the "D" section as the most efficient in converting flow energy among square and two types of triangle sections.

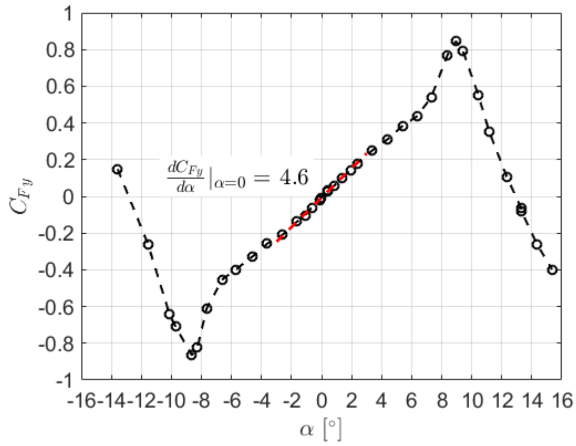

Figure 5.3 Transverse force coefficient for a rectangular cross section *(Mannini, et al., 2018)*

In the present work, in order to be free to analyse different kind of configurations, it has been chosen to consider the effects of lift and drag separately, thus both of them has been approximated with a seventh degree polynomial function, for all the considered cross sections.

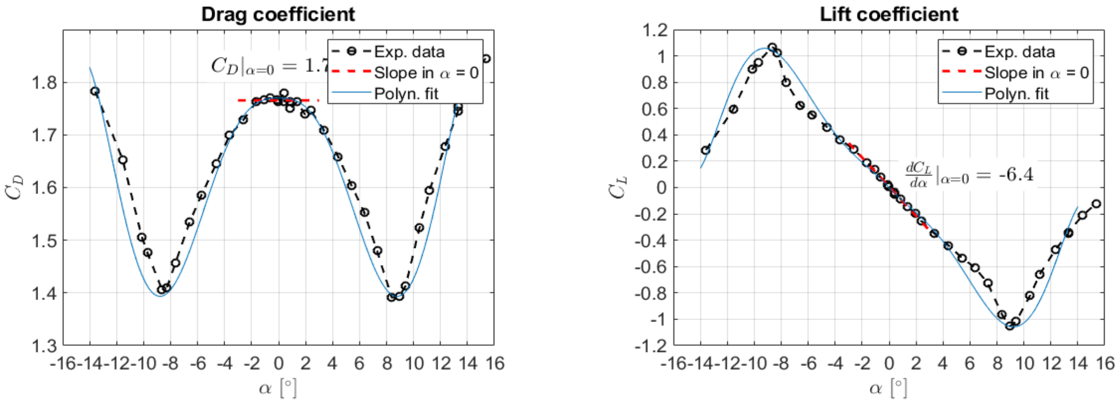

Figure 5.4 Polynomial fit of experimental measurements of drag and lift force coefficients for a rectangular cross section

In Figure 5.4 it is reported the polynomial fit of lift and drag coefficients for the same rectangular section as in Figure 5.2. The same procedure has been followed for different kind of cross section: a square, an isosceles triangle (with $\beta = 30°$), an equilateral triangle ($\beta = 60°$) and a "D" section, whose experimental data have been taken from literature. The coefficients of the polynomial fit for each section are reported into the following table.

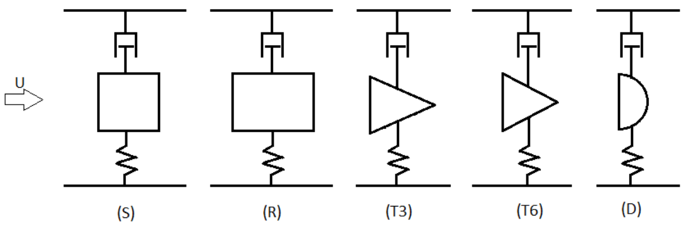

Figure 5.5 Cross section types considered in this work

		a_0	a_1	a_2	a_3	a_4	a_5	a_6	a_7
S	C_D	2.1000	0	-0.0028	-0.0015	2.3757e-04	-1.2495e-05	2.8576e-07	-2.4257e-09
	C_L	0	-0.1000	0.0175	-0.0039	3.8764e-04	-1.7437e-05	3.6362e-07	-2.8800e-09
R	C_D	1.7700	0	-0.0015	-0.0013	-1.7111e-04	5.9356e-05	-3.8901e-06	7.3675e-08
	C_L	0	-0.1117	0.0127	-0.0016	-6.0357e-04	1.0838e-04	-4.7515e-06	3.8272e-08
T3	C_D	0.7198	0	-0.0014	2.2129e-04	-2.4942e-05	1.3879e-06	-3.4379e-08	3.0959e-10
	C_L	0	-0.0522	0.0054	-0.0010	8.2338e-05	-2.7253e-06	3.8825e-08	-1.8747e-10
T6	C_D	1.7845	0	1.4920e-04	-1.0513e-04	4.3406e-06	-7.2429e-08	5.5345e-10	-1.5986e-12
	C_L	0	-0.0405	0.0022	-2.4903e-04	1.0241e-05	-1.7904e-07	1.4402e-09	-4.4232e-12
D	C_D	3.8476	0	-9.7683e-04	2.8494e-07	2.0157e-07	-1.3793e-09	3.2987e-13	1.0875e-14
	C_L	0	-0.0872	3.8060e-04	-1.3989e-05	1.2195e-06	-1.9219e-08	1.1263e-10	-2.2815e-13

Table 1 Polynomial fit coefficients. S: square, R: 1.5 side ratio rectangle, T3: isosceles triangle with $\beta = 30°$, T6: equilateral triangle, D: "D" section.

Moreover, the following figures show the comparison between the experimental data and the polynomial fit over a sufficiently large range of angle of attack, for the triangular and "D" sections.

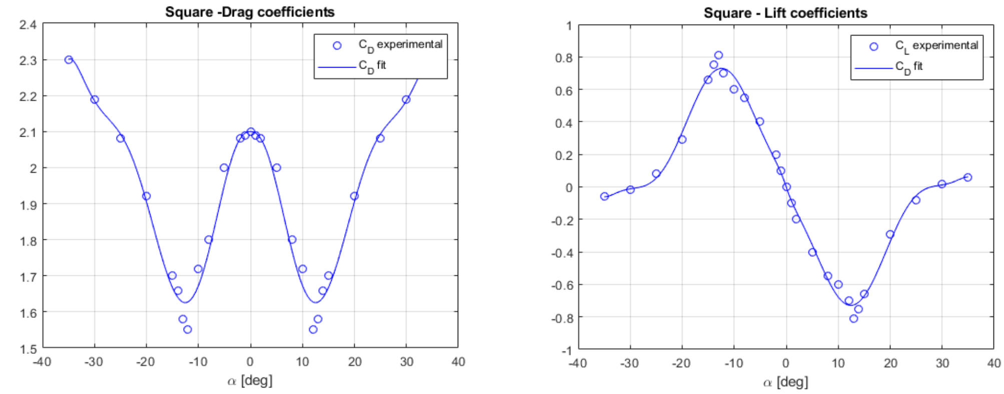

Figure 5.8 Polynomial fit of experimental measurements of drag and lift force coefficients for the square cross-section. Experimental data from *(Carassale, et al., 2013)*

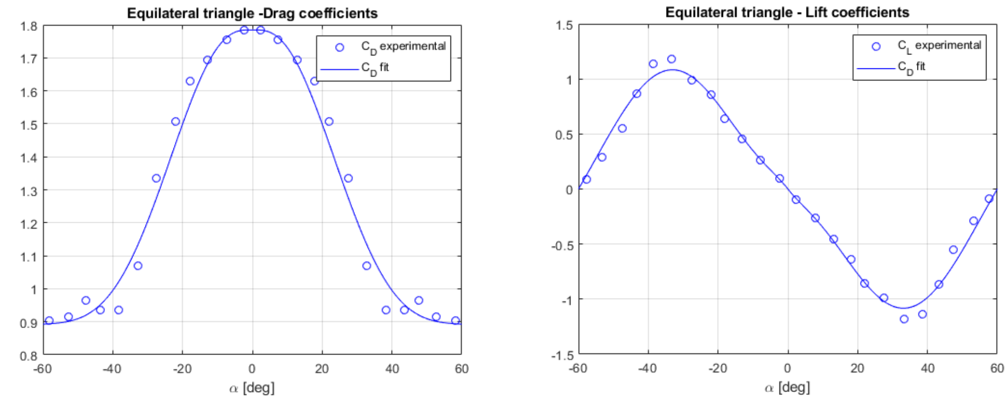

Figure 5.7 Polynomial fit of experimental measurements of drag and lift force coefficients for the equilateral triangle cross-section. Experimental data from *(Alonso & Meseguer, 2006)*

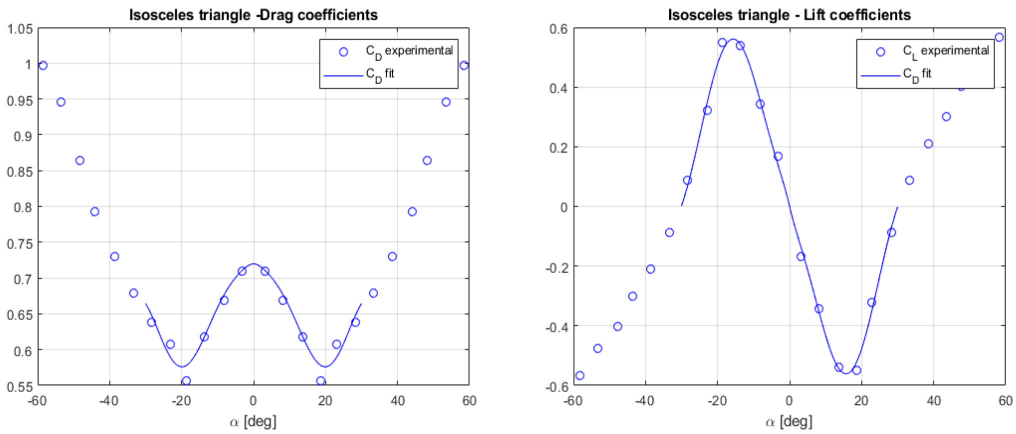

Figure 5.6 Polynomial fit of experimental measurements of drag and lift force coefficients for the isosceles triangle cross-section. Experimental data from *(Alonso & Meseguer, 2006)*

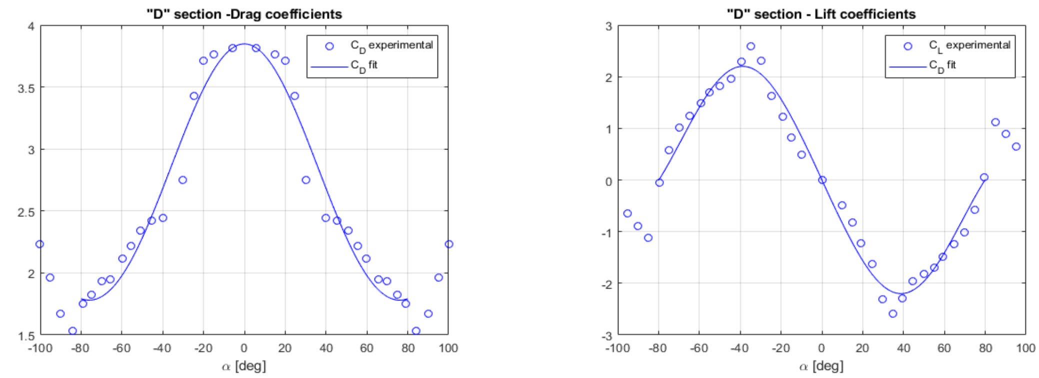

Figure 5.9 Polynomial fit of experimental measurements of drag and lift force coefficients for the "D" cross section. Experimental data from *(Liu, et al., 2013)*

Following the same process as in the VIVs analysis, the dimensionless form of the motion equation is obtained by introducing the dimensionless parameters reported in the table. Moreover, in a first approximation, the relative flow velocity has been considered equal to the undisturbed velocity to simplify the dimensionless expression.

$$U_{rel}{}^2 = U^2 + \dot{y}^2 \cong U^2 \tag{5.8}$$

Structure natural frequency	$\omega_n = \sqrt{\dfrac{k}{ml}}$	Damping ratio	$\zeta = \dfrac{c_s + c_{em}}{2ml\omega_n}$
Reduced displacement	$Y = \dfrac{y}{D}$	Reduced mass	$m_r = \dfrac{m}{\rho D^2}$
Reduced velocity	$U_r = \dfrac{U}{f_n D}$	Dimensionless time	$\tau = \omega_n t$

Finally, by changing the differentiation time from t to τ, the resulting governing equation will become:

$$\ddot{Y} + 2\zeta\dot{Y} + Y = \frac{1}{2}\frac{U_r{}^2}{m_r}[-C_L\cos(\alpha) - C_D\sin(\alpha)] \tag{5.9}$$

Where the angle of attack α can be easily expressed as a function of dimensionless parameters too:

$$\tan(\alpha) = 2\pi\frac{\dot{Y}}{U_r} \tag{5.10}$$

5.2. Numerical solution and methodology

For each value of reduced velocity in a range from 5 to 50, the differential equation is solved through the equivalent model on Simulink, reported in the Figure 5.10, which is composed by two parts. One section integrates the nonlinear differential equation, and the second, highlighted in the figure, calculates the fluid load on the structure at each time step, taking into account the variation of the angle of the attack while the body moves.

At the first iteration, the initial values are set in order to introduce a small perturbation in the transverse motion of the bluff body:

$$Y_0 = 0.01 \qquad\qquad \dot{Y}_0 = 0$$

For each value of reduced velocity the simulation has been carried on for a dimensionless time range equal to 200, which is large enough to guarantee that the steady state solution is reached. The final value of $\dot{Y}$ and Y has then been taken as initial condition for the simulation of the subsequent reduced velocity value.

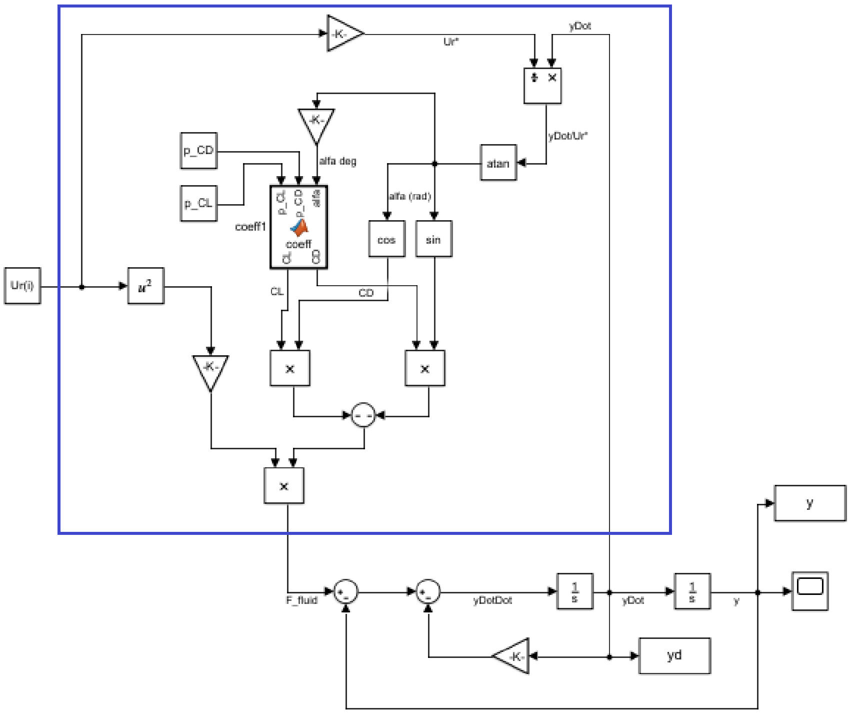

Figure 5.10 Simulink model of the governing equation dimensionless form. The highlighted parte calculates the fluid load at each time step.

For each reduced velocity step, maximum amplitude, frequency response and the maximum value of the wake variable q have been recorded.

The main outcomes of the analysis of the galloping dimensionless model consist in the evaluation of the normalized semi-amplitude response $Y = y/D$, which comes directly from the numerical resolution, and the efficiency of conversion, calculated from the equation.

$$\eta = \frac{absorbed\ power}{available\ power\ throgh\ the\ swept\ area} = \frac{\frac{1}{T}\int_0^T c\dot{y}^2 dt}{\frac{1}{2}\rho U^3 (2y+D) l} \tag{5.11}$$

Also in this case, in order to compare the performance with the Betz limit, we refer to the fluid-dynamic conversion efficiency, in which the absorbed power is set equal to the power dissipated from both mechanical and electromechanical damping, and the efficiency can be expressed as:

$$\eta = \frac{\frac{1}{T}\int_0^T (c_s + c_{em})\dot{y}^2 dt}{\frac{1}{2}\rho U^3 (2y+D) l} \tag{5.12}$$

Introducing the dimensionless parameters reported in table, the equation becomes:

$$\eta = 4(2\pi)^3 \frac{m_r\zeta}{U_r^3} \frac{1}{(2Y+1)} \frac{1}{\Gamma} \int_0^\Gamma \dot{Y}^2 d\tau \tag{5.13}$$

For each reduced velocity step, the conversion efficiency has been calculated over five complete oscillations in order to obtain an average value.

5.3. Dimensionless analysis - Results

As explained in the introductory chapter, the galloping instability occurs above a particular wind speed, which depends on the structure and cross section properties.

$$U_{cr} = \frac{2c}{\rho D\left(-\frac{\partial C_L}{\partial \alpha}\Big|_{\alpha=0} - C_D|_{\alpha=0}\right)} \tag{5.14}$$

In its dimensionless form, the equation expressing the cut-in wind speed will become:

$$U_{r\,cr} = \frac{8\pi m_r\zeta}{\left(-\frac{\partial C_L}{\partial \alpha}\Big|_{\alpha=0} - C_D|_{\alpha=0}\right)} \tag{5.15}$$

From this expression, it is clear that the critical speed grows with the product of reduced mass and damping ratio: consequently, in order to achieve a obtain a determined critical speed, the higher the reduced mass, the lower must be the damping ratio.

As mentioned before, in order to obtain accurate results while applying the pseudo-static approximation, it is required that the reduced velocity is at least equal to 10: as a consequence, it is possible to determine from the previous equation the minimum value of the mass-damping parameter, required to respect the constraint.

$$(m_r\zeta)_{min} = \frac{10}{8\pi}\left(-\frac{\partial C_L}{\partial \alpha}\Big|_{\alpha=0} - C_D|_{\alpha=0}\right) \tag{5.16}$$

It is important to note that the mass-damping ratio is proportional to the Scruton number, which is an important dimensionless number found to be related to interference between VIVs and galloping. It was found that over a certain value of the Scruton number, VIVs and galloping response of structure are completely separated and independent, while on the contrary, it is possible to have a range of wind speed in which both the mechanisms are present (Mannini, et al., 2018). In our case, by imposing a reduced velocity higher than 10, the VIVs phenomenon should not interfere, since it is typically characterized by reduced velocity of the order of 5. Moreover, the eventual interference between VIVs and galloping would actually improve the performance of the system at low wind speed, thus neglecting its effects will eventually give conservative results at low wind speed.

5.3.1. Effect of cross section

As expressed in the equations, the minimum required value of the mass-damping parameter is only dependent on the properties of the bluff body section. In the following table, it is reported for each section type, the fundamental parameter $\left(-\frac{\partial C_L}{\partial \alpha}\Big|_{\alpha=0} - C_D|_{\alpha=0}\right)$ and the minimum mass-damping parameter necessary to obtain a critical reduced velocity above 10.

Cross section type	$\left(-\frac{\partial C_L}{\partial \alpha}\Big\|_{\alpha=0} - C_D\|_{\alpha=0}\right)$	Mass-damping $(m_r\zeta)_{min}$
Square	3.6296	1.4442
Rectangle (side ratio = 1.5)	4.6299	1.8422
Isosceles triangle ($\beta = 30°$)	2.2710	0.9036
Equilateral triangle ($\beta = 60°$)	0.5372	0.2137
“D”	1.1486	0.4570

The obtained value can be interpreted as an indication of how much a section shape is prone to galloping. High values of $\left(-\frac{\partial C_L}{\partial \alpha}\Big|_{\alpha=0} - C_D|_{\alpha=0}\right)$, and consequently $(m_r\zeta)_{min}$, indicate that the system easily experience galloping and thus requires an high mass-damping to "delay" the onset of galloping to the imposed reduced velocity.

As can be noted, there is a significant difference between the obtained values for the rectangular shape and the equilateral triangle. This means that in the same conditions of reduced mass and critical reduced velocity, the correspondent value of damping ratio for the rectangular shape will be proportionally higher.

In the Figure 5.11 are reported the system performances for each cross section, assuming a reference reduced mass equal to 15. The required damping ratio to obtain a critical reduced velocity equal to 10 will be dependent on the specific cross section, and the value of reduced mass.

$$\zeta > \frac{20}{8\pi m_r}\left(-\frac{\partial C_L}{\partial \alpha}\Big|_{\alpha=0} - C_D|_{\alpha=0}\right) \tag{5.17}$$

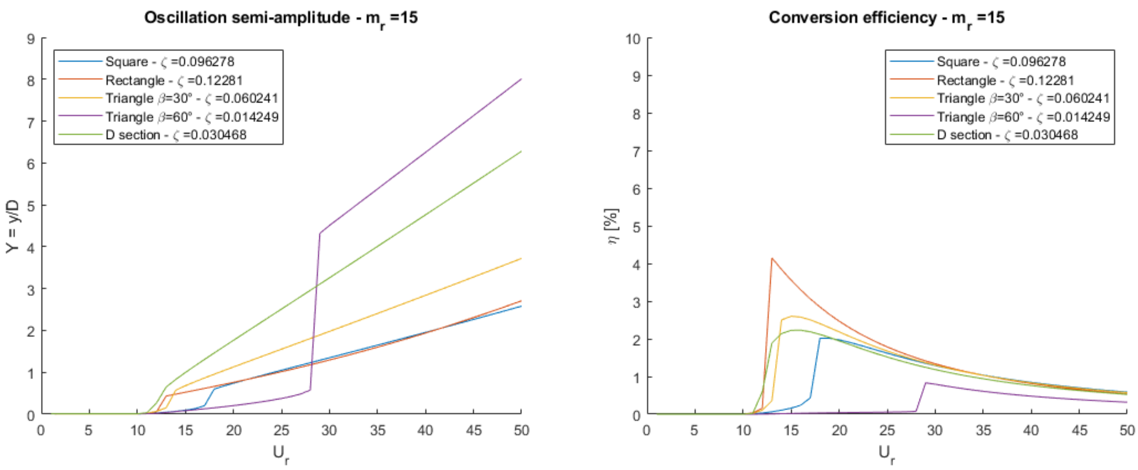

Figure 5.11 Oscillation semi-amplitude and conversion efficiency obtained with different cross section shape. $U_{r_{cr}} = 10$

The first important characteristic of galloping response is the high amplitude of oscillations: unlike in VIVs, galloping response reaches amplitudes of the order of different times the characteristic dimension of the bluff body, depending on the cross section type. Moreover, all the response present a sudden jump in the semi-amplitude, which gives origin to an hysteresis behaviour if the flow speed is gradually reduced (Figure 5.12).

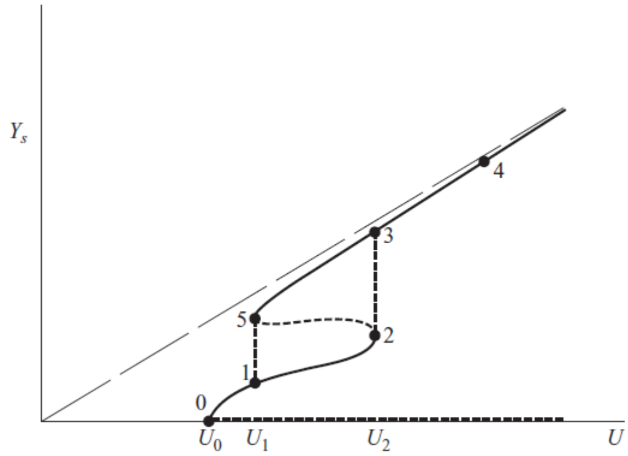

Figure 5.12 Hysteresis behaviour in galloping oscillation amplitude
(Païdoussis, et al., 2011)

In the energy harvesting perspective, high amplitudes are a good feature since the captured power is proportional to the swept area. However, the results show also a relatively low efficiency of conversion for all the section types, probably due to the low frequency characterizing the phenomenon. As can be noted, the rectangular shape is characterized by the best efficiency among the considered sections (about 4.1%), followed by the isosceles triangle (2.6%) and the "D" section(2.2%), while the worst efficiency is given by the equilateral triangle shape.

Apparently, the conversion efficiency seems to be related with the amplitude of oscillation. For small oscillations, the absorbed power is presumably very low and so is the conversion efficiency. As the oscillations grow, also the efficiency increases and gets to an optimum when the amplitude overcome the discontinuity and reaches higher values. After that, the efficiency decreases again as the amplitude continues rising to very high values: from this point on, the swept are is too large in comparison to the extracted power. This behaviour perfectly explain the low performances of the equilateral triangle-type section, whose oscillations amplitude remains very low over a wide range of reduced velocity, and then suddenly grows to values higher than those of other cross sections after the discontinuity. The rectangular section, on the contrary, reaches the discontinuity in the oscillation amplitude quickly, and after that is characterized by moderately large oscillations, which are positive in the energy harvesting process.

The power output of the energy harvester will depend on the product of swept area and conversion efficiency: consequently, if the design focus is on the power output, it is not necessarily true that the optimal solution is characterized by the best efficiency. In facts, starting from the equation of the absorbed power, it is possible to define a dimensionless parameter, that here will be called *reduced power*, which represents the power output for a given bluff body size and wind speed. By definition, the reduced power is actually the ratio between the power absorbed by the structure and the power that passes through the frontal area of the bluff body. Many authors actually used this parameter as the conversion efficiency

$$P_{F-B} = \eta P_{wind} = \eta \frac{1}{2} \rho U^3 (2y + D) l \tag{5.18}$$

$$P_r = \frac{P_{F-B}}{\frac{1}{2}\rho U^3 D l} = \eta (2Y + 1) \tag{5.19}$$

In the figure is reported the product of efficiency and reduced swept area in order to evaluate the section with the best power output

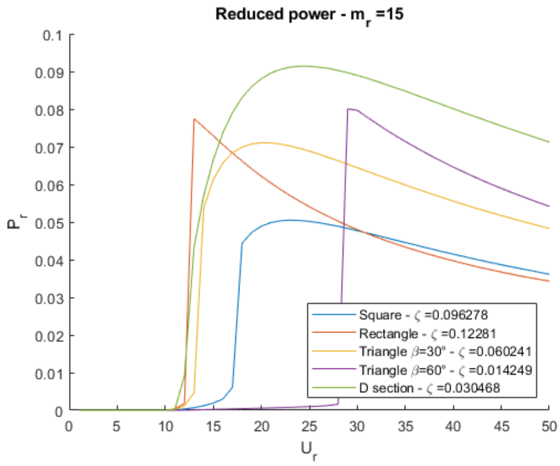

Figure 5.13 Comparison of reduced power for different cross sections. $U_{r_{cr}} = 10$

By this perspective, the best reduced power is obtained with the "D" section prism, which presents also a more gentle slope over the considered range of reduced velocity. Moreover, the range of reduced velocity characterized by high values of reduced power is between 20 and 25, where the system dynamic is completely dominated by galloping. For what concern the rectangular section, it can be noted that the maximum reduced power is obtained in the same conditions of reduced velocity as the maximum in the conversion efficiency: this means that optimizing the two of them produces the same results for the rectangular shape.

Consequently, depending on the design purpose, one may choose the rectangular or the "D" section prism as a bluff body. In general, it can be said that if the purpose is to generate large quantities of energy the conversion efficiency plays an important role, as we can see looking at the traditional wind turbines performance. On the other hand, if the design purpose is to generate a minimum amount of power to aliment a wireless electronic device, the traditional definition of efficiency may not be the main important aspect to consider. In this case, the reduced power would be a better parameter to maximize.

5.3.1. Effect of reduced mass and damping

Different values of reduced mass and damping produce the same effects for all the section shapes. Therefore, in the following paragraph will be reported the results of the analysis made on a "D" section bluff body, which has been chosen arbitrarily.

The effect of varying the reduced mass is reported on the left side of Figure 5.14. For each value of reduced mass, a correspondent value of damping ratio is calculated in order to obtain the same mass-damping parameter, hence the same critical reduced velocity, which is set equal to 10. As can be noted, varying the value of reduced mass, maintain the same mass-damping, does not have significant effects on the system performances: the conversion efficiency seems unaffected by its variations, while the oscillation amplitude grows slightly faster with low reduced masses. Apparently, galloping-based energy harvesters are not strictly limited to very low value of reduced mass as those based on VIVs.

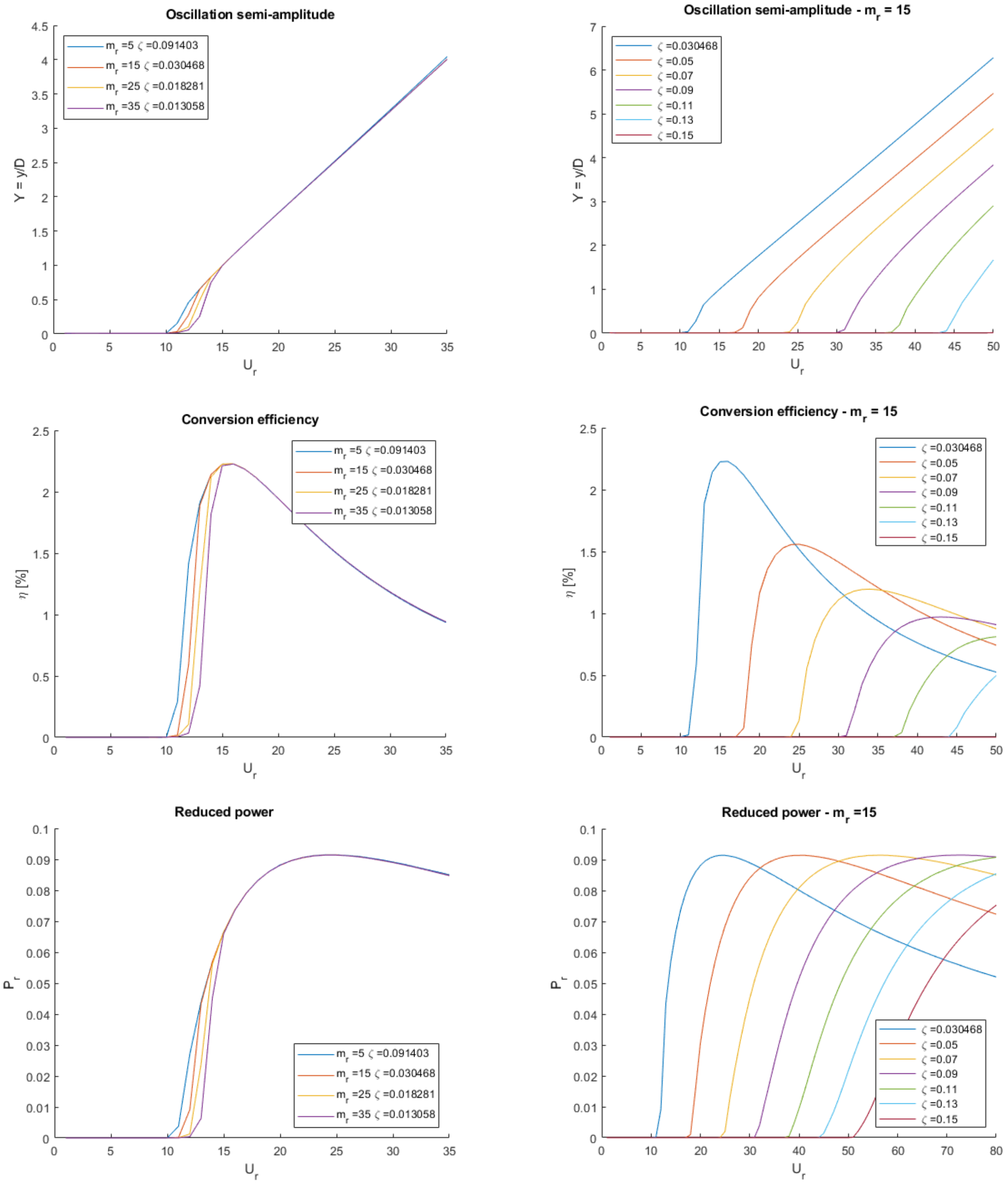

Figure 5.14 Oscillation semi-amplitude, conversion efficiency and reduced power, calculated for a "D" cross-section, imposing $U_{r_{cr}} = 10$. On the left, the curves are obtained with different values of reduced mass, maintaining the $m_r\zeta$ constant. On the right, the responses are obtained for different value damping ratio, maintaining m_r

On the other hand, since there is a component of damping due to mechanical friction that dissipates part of absorbed mechanical power, galloping energy harvesters need to be moderately light, in order to maintain the reduced mass value small enough to obtain the desirable cut-in wind speed with affordable damping values. In facts, the effective electrical power output will be proportional to the electromechanical fraction of the total damping.

The right side of Figure 5.14 shows the effect of varying the damping ratio from the minimum imposed value to a maximum of $\zeta = 0.15$, while maintaining the reduced mass constant. Increasing damping means increasing the critical reduced velocity, but also decreasing the maximum conversion efficiency, with an negative effect on the harvesting performance. On the other hand, it does not affect the reduced power maximum value, but the curve is translated to higher values of reduced velocity.

5.4. Design of dimensional parameters

The dimensionless model analysis showed that galloping-based energy harvesters performance strongly depends on the bluff body cross-section type. As explained in the previous paragraph, depending on the desired parameter to maximize the choice of the cross section changes. To obtain the best conversion efficiency, as traditionally defined, the rectangular shape with side ratio $B/D = 1.5$ seems to be the best option. On the other hand, if the design objective is to maximize the power output, and then the reduced power, the “D” section should present slightly better results.

In both the cases, for a given mass-damping, the system performances are not dependent to the value of reduced mass. This is obviously an advantage while operating in air, where low m_r are achieved only thanks to very light material, which are usually expensive. However, in the context of this chapter the value of reduced mass will be set equal to 15, which is the same condition considered for the VIVs-based energy harvesters.

For both rectangular and D section it is possible to express the linear mass as function of the diameter and the material density. The linear modal mass, will be the sum of the structure mass, and the aerodynamic added mass, calculated as in (Blevins, 2001), all increased by 10% in order to take into account other system components inertia.

Considering the bluff body as a hollow rectangle with $B/D = 1.5$, the thickness of which is proportional to the frontal side D, ($\frac{S}{D} = cost$), the modal mass will become:

$$m = 1.1D^2\left(2(1+\frac{B}{D})\frac{S}{D}\rho_s + C_a\pi\rho_{air}\right) \tag{5.20}$$

The reduced mass, as defined in the dimensionless parameter table, will be independent from the bluff body size.

$$m_r = \frac{1.1D^2\left(2(1+\frac{B}{D})\frac{S}{D}\rho_s + C_a\pi\rho_{air}\right)}{\rho_{air}D^2} = 1.1\left(2(1+\frac{B}{D})\frac{S}{D}\frac{\rho_s}{\rho_{air}} + C_a\pi\right) \tag{5.21}$$

Instead, considering a “D” section bluff body, with the same assumption on the sheet thickness ($\frac{S}{D} = cost$), the modal mass will become:

$$m = 1.1D^2\left((\frac{1}{2}\pi + 1)\frac{S}{D}\rho_s + C_a\pi\rho_{air}\right) \tag{5.22}$$

Then, the reduced mass:

$$m_r = \frac{1.1D^2\left((\frac{1}{2}\pi+1)\frac{s}{D}\rho_s+C_a\pi\rho_{air}\right)}{\rho_{air}D^2} = 1.1\left((\frac{1}{2}\pi+1)\frac{s}{D}\frac{\rho_s}{\rho_{air}}+C_a\pi\right) \tag{5.23}$$

Obviously, the ratios $\frac{s}{D}$ and $\frac{\rho_s}{\rho_{air}}$ depend on the particular material used. Consequently, given a structural configuration and the selected material, the reduced mass should be almost univocally determined.

Imposing a critical reduced velocity of 10, thus a corresponding minimum damping ratio, the dimensionless model analysis showed that the best performances are obtained for a particular value of reduced velocity. In case the aim is to maximize the conversion efficiency, the optimal conditions are achieved with the rectangular section at a reduced velocity of 1.5. On the other hand, if the purpose is to maximize the power output, the best results are obtained with the "D" section at a reduced velocity equal to 24.

Consequently, it is important to choose the bluff body size and the structural natural frequency in such a way to obtain the best performance in the right range of wind speed.

As made in the VIVs analysis, there are two cases that needs to be analysed:

1. all the parameters of the system are kept fixed,
2. it is possible to control the system's stiffness and damping in order to adapt to each operational condition, optimizing the power output.

5.4.1. Case 1. Fixed parameters

In case all the design parameters are kept constant, the choice of size and frequency requires the definition of a design condition for wind speed, which comes from the wind assessment of each particular site. In the context of this chapter, the design wind speed will be set equal to 5 m/s as made in the VIVs-based systems.

As a result, the relation that front side D and frequency should respect can be obtained from the definition of reduced velocity.

$$f_n D = \frac{U}{U_{r_{opt}}} \tag{5.24}$$

Consequently, the designer is free to select a particular front side and consequently determine the necessary natural frequency of the structure. However, a larger value of diameter will provide higher swept area, and thus a higher amount of power from which to extract energy. On the other hand, big front sides will also determine large occupied volumes, which could result as a drawback in the power density evaluation.

For a given front side length, it is possible to estimate the modal mass, natural frequency, and therefore the system's stiffness.

$$m = m_r \rho_{air} D^2 \tag{5.25}$$

$$f_{n_{opt}} = \frac{U}{U_{r_{opt}} D} = \frac{0.4}{D} \tag{5.26}$$

$$k_{opt} = \omega_n{}^2 ml = \left(2\pi f_{n_{opt}}\right)^2 ml \tag{5.27}$$

As explained in the previous paragraph, the optimal value of the damping ratio is the minimum necessary to impose a given critical reduced velocity. Therefore, once $U_{r_{cr}}$ has been selected, it only depends on the reduced mass value and the section properties.

$$\zeta_{opt} = \frac{20}{8\pi m_r}\left(-\frac{\partial C_L}{\partial \alpha}\bigg|_{\alpha=0} - C_D|_{\alpha=0}\right) \tag{5.28}$$

On the other hand, the corresponding optimal physical damping value will depend on the structure natural frequency and modal mass, thus will be a function of the size too.

$$c_{opt} = 2(2\pi f_{n_{opt}})\zeta_{opt} ml \tag{5.29}$$

	Rectangular section		"D" section	
Front side D $[m]$	$f_{n_{opt}}$ $[Hz]$	c_{opt} $[N/(m/s)]$	$f_{n_{opt}}$ $[Hz]$	c_{opt} $[N/(m/s)]$
0.0100	40.0000	0.1134	20.8333	0.0147
0.0500	8.0000	0.5672	4.1667	0.0733
0.0900	4.4444	1.0209	2.3148	0.1319
0.1300	3.0769	1.4746	1.6026	0.1905
0.1700	2.3529	1.9284	1.2255	0.2492

Figure 5.15Figure 3.15 shows the response semi-amplitude calculated for different value of front side D, considering a bluff body length of 1 m. In order to obtain sufficiently reliable results, the diameter measure considered do not exceed 0.17 m, which is chosen in order to maintain an aspect ratio $\frac{l}{D}$ bigger than 6. Corresponding value of natural frequency and damping are reported in the table.

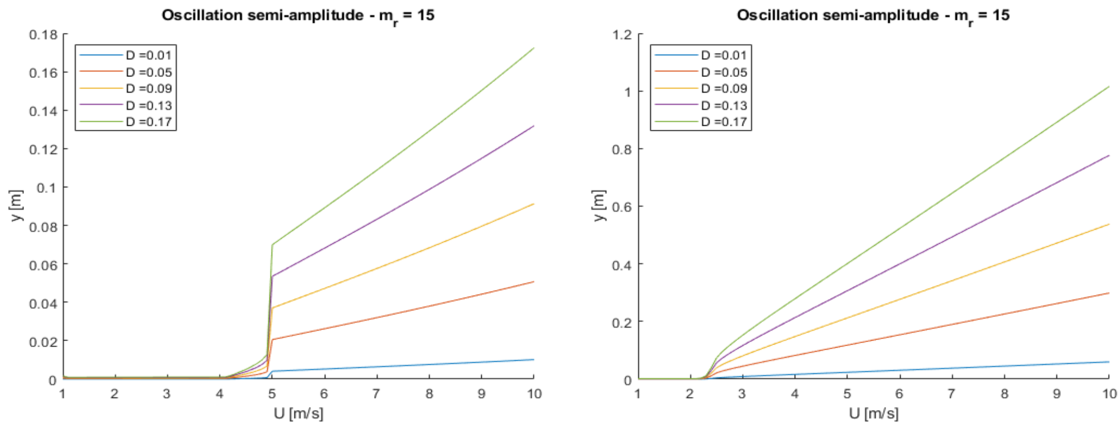

Figure 5.15 Response semi-amplitude calculated for different values of the frontal side D. On the left side, rectangular section. On the right, "D" section.

The power absorbed by the structure, and the actual power converted into electricity will be:

$$P_{F-B} = \eta P_{wind} = \eta \frac{1}{2}\rho U^3(2y + D)l \tag{5.30}$$

$$P_{em} = \eta_{em} P_{wind} = \eta_{em}\frac{1}{2}\rho U^3(2y + D)l = \frac{\zeta - \zeta_s}{\zeta}\eta\frac{1}{2}\rho U^3(2y + D)l \tag{5.31}$$

Where the mechanical damping ratio ζ_s, mainly due to friction, is estimated as equal to 0.002, as made in the VIVs analysis.

Resulting absorbed mechanical power and converted electrical power are reported in Figure 5.16 and Figure 5.17. As can be noted, there's not a significant difference between the power output of the rectangular and "D" sections, while the oscillation amplitudes are much higher in the second case, leading to a worse power density.

On the other hand, the figures clearly show that the rectangular bluff body presents a sudden jump in both oscillation amplitude and power output. Consequently, the design wind speed should be accurately selected in order to maximize the exploitation of the wind resource in each site.

Overall, the rectangular shape seems to be the best choice for an energy harvester, with a good compromise of power output and conversion efficiency.

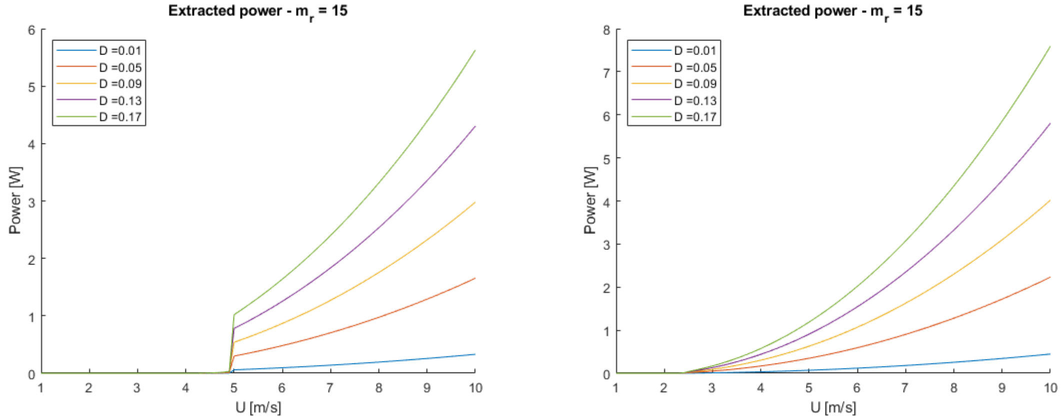

Figure 5.16 Mechanical power absorbed by the system, calculated for different values of the front side D. On the left side, rectangular section. On the right, “D” section.

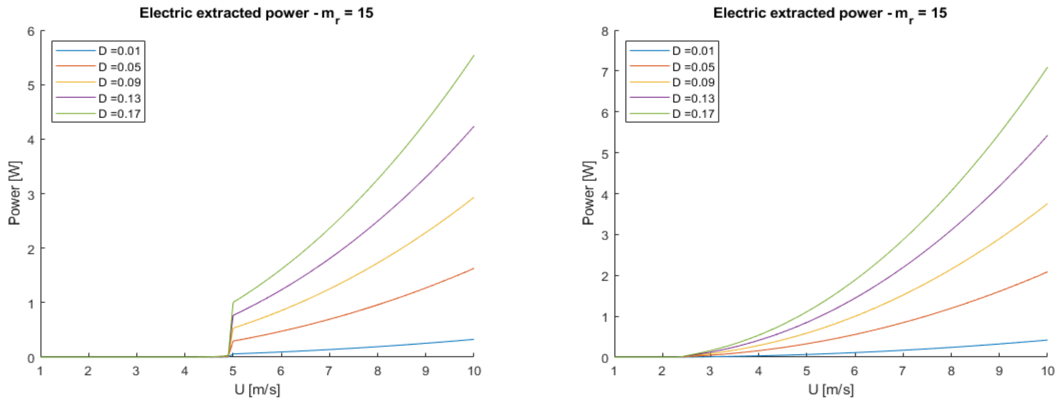

Figure 5.17 Electric power converted by the system, calculated for different values of the front side D. On the left side, rectangular section. On the right, “D” section.

5.4.2. Case 2. Tuned parameters

By tuning the values of the electromechanical stiffness and damping, it is possible to influence the system response and obtain the best operation conditions over a range of wind speeds instead that for one single value.

Given a set of reduced mass and damping ratio, the maximum efficiency conversion is achieved for a particular value of reduced velocity. Beyond this value, the efficiency starts decreasing as the reduced velocity increases. Theoretically, by varying the system stiffness with the wind speed, it is possible to adapt its natural frequency in order to obtain the same optimal conditions of reduced velocity over a wide range of wind speed.

The system frequency and stiffness would be a function of the wind speed:

$$f_n(U) = \frac{U}{U_{r_{opt}}D} = \frac{U}{12.5\ D} \tag{5.32}$$

$$k_{opt}(U) = \omega_n{}^2 ml = (2\pi f_n)^2 ml \tag{5.33}$$

Moreover, being function only of the reduced mass, the optimal damping ratio remains constant, while the optimal system damping would be a function of the wind speed, since it depends on the natural frequency:

$$c_{opt}(U) = 2\omega_n \zeta_{opt} ml \tag{5.34}$$

As mentioned, the value of c cannot decrease below the threshold of the mechanical damping due to friction: as a result, there is a minimum wind speed, below which the system will not be able to produce electrical power.

In figure it is reported the system response and performance obtained by adapting stiffness and damping to the wind speed.

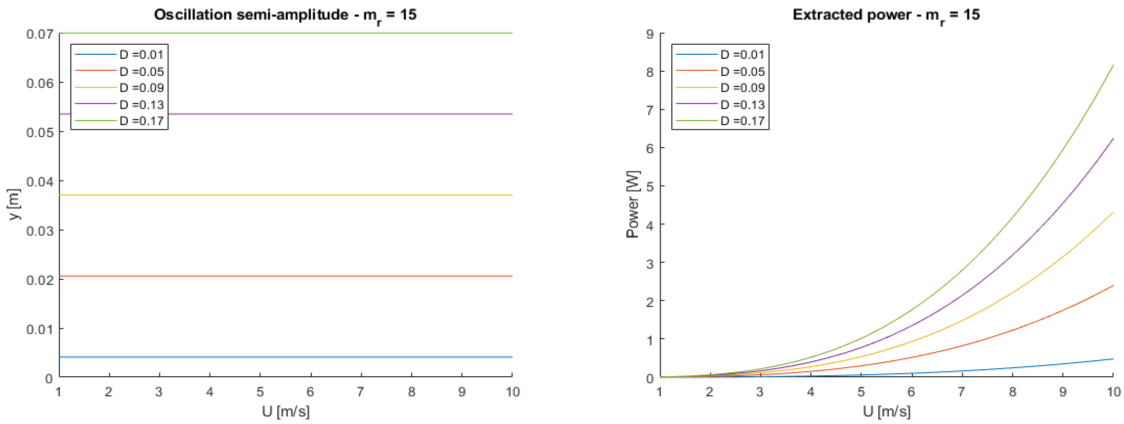

Figure 5.18 Response semi-amplitude and mechanical absorbed power, calculated for a rectangular section by varying stiffness and damping with the wind speed.

As expected, by varying stiffness and damping of the system, it continues operating in the same conditions of reduced velocity and damping ratio. Therefore, also the reduced semi-amplitude and efficiency remains constant as the wind speed changes. In particular, Y remains equal to 0.41, which means that the real semi-amplitude remains constant as well and proportional to the front side length, while the efficiency is constant and equal to 4.3%. Consequently, with a constant swept area and efficiency, the absorbed power grows with the cube of the wind speed.

6. Design concept selection

6.1. Comments on VIVs and galloping as energy harvesting mechanisms

The analysis of the VIVs and galloping mathematical models revealed that none of the two fluid-structure interaction mechanisms is characterized by high values of conversion efficiency. In fact, in both cases the maximum efficiencies are of the order of a few percentage points, between 4 and 5%, which is about ten times less than the traditional horizontal axis wind turbines.

The conversion efficiency is an important parameter to consider in the design of an energy harvester, especially in the case where the objective is to generate high power. In fact, for the same power produced, a system with low efficiency would require proportionally wider swept surfaces, hence larger dimensions and ultimately higher costs. Consequently, it is possible to state that the conversion systems based on FIVs are not suitable for applications where high power is required, as they would present a disadvantageous power volume ratio compared to traditional turbines.

On the other hand, systems based on FIVs have the characteristic of working with bodies with very simple sections, which are expected to be cheaper compared to a blade profile. This, combined with the possibility of specifically design FIVs systems to adapt to low wind speeds, makes them a potentially good alternative in situations where the goal is to generate limited amounts of power to feed a wireless electronic device, in places that are difficult to access or isolated.

Examples might be sensors measuring air temperature and humidity in building air ducts in order to improve the air conditioning adjustments, or sensors measuring significant meteorological data in agriculture. In these cases, harvesting power from resources already available in the environment, such as wind sun or mechanical vibrations, can highly reduce costs related to the replacement and oversizing of batteries. In this perspective, the power requirement is limited to very small values, ranging from a few mW to a handful of watts. In this sense, both VIVs and galloping based systems provide limited but sufficient amount of power. Moreover, in the applications described above, the efficiency of conversion is not necessarily the most important parameter, as the resource from which energy is drawn can be abundant compared to the required power.

In the following figures is reported a comparison between VIVs and galloping responses, in the case of a characteristic dimension *D* (cylinder diameter for VIVs and prims front side for galloping) equal to 0.16 m.

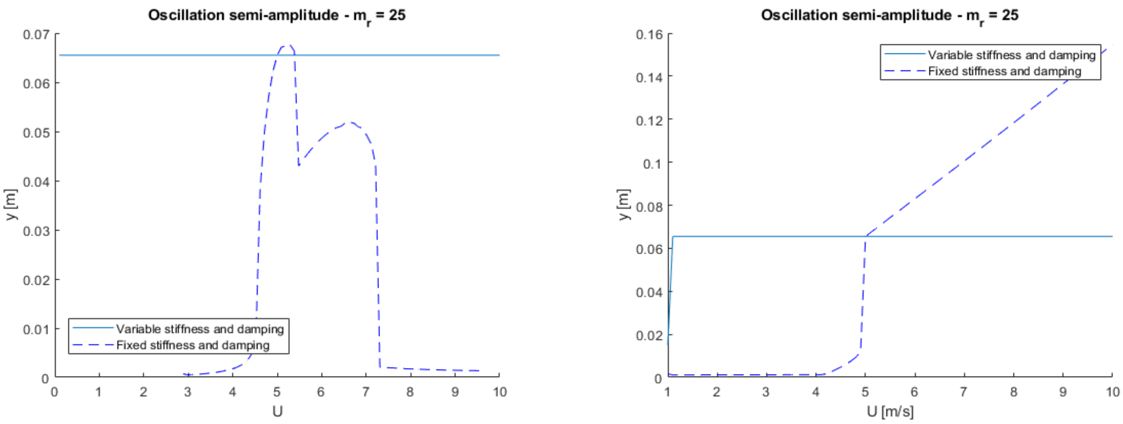

Figure 6.1 Response semi-amplitude of a system experiencing VIVs (left) and galloping (right). D = 0.16 m

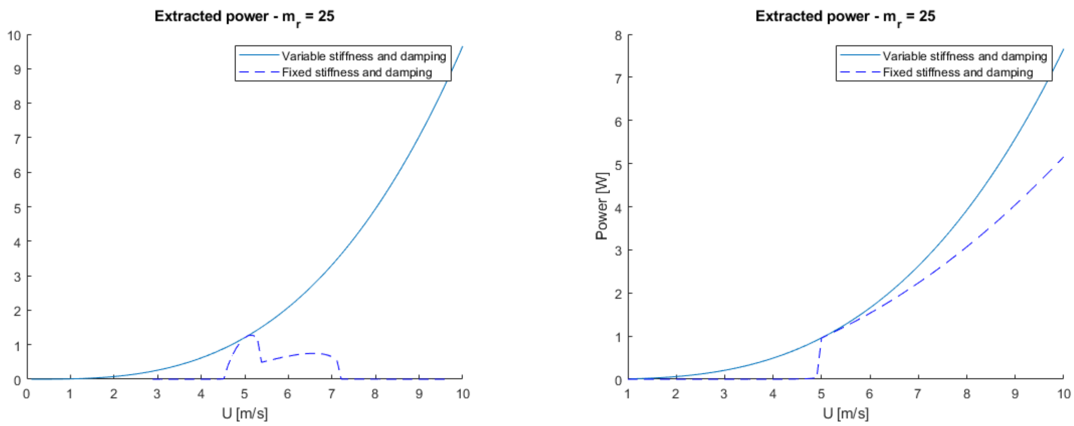

Figure 6.2 Mechanical power extracted from the wind flow by a system experiencing VIVs (left) and galloping (right). D = 0.16 m

As seen in chapter 4, VIVs are a particular phenomenon of resonance in which the frequency of the alternating fluid force generated by vortex shedding matches the structure natural frequency. Interestingly, the shedding frequency, which in theory grows as the wind speed increases, is forced by the fluid-structure interactions to synchronize with the structure oscillation frequency over a wider range of wind speed. In this lock-in region, the self-limited oscillation amplitude reaches values up to 0.6 time the diameters. However, the conversion efficiency and the power output of the system reach significant values only in a small range of wind speed, very close to the theoretical resonance condition. Thus, in order to extend the operation range, it has been supposed to control the stiffness contribute of the electrical generator in order to vary the system natural frequency, and synchronize it with the vortex shedding frequency as the wind speed grows. Moreover, the maximum value of conversion efficiency and power output are highly affected by the mass-damping parameter: in particular, they present an optimum when the mass-damping is equal to 0.2. Consequently, as the frequency changes, also the electromechanical damping needs to be adapted to the new conditions.

As a result, the response amplitude would remain constant as long as structure and vortex shedding frequency remain synchronized. Thus, once the wind speed reaches values that are could possibly damage the structure, it is enough to desynchronize the two frequencies to make the system automatically stop.

Vice versa, the galloping instability appears when the transversal forces generated by the wind on a certain type of bluff body, overcome the system damping and produce a positive work as the system oscillates. As explained in chapter 5, the galloping instability starts in correspondence of a particular critical wind speed, which depends on the structure cross-section and mass-damping, and from this value on the amplitude continues to grow as the wind speed increases. Consequently, as the wind speed increases, the amplitude of oscillations can reach values that are not compatible with the integrity or at least the safety of the structure. Moreover, it has been found that the conversion efficiency reaches its maximum for a specific value of reduced velocity, and consequently for a specific value of frequency for each value of wind speed. Hence, it has been proposed to vary the system natural frequency by controlling the electromechanical stiffness and damping contributes, in order to maintain the same conditions of reduced velocity and damping ratio as the wind speed grows.

As a result, also in this case the system would experience constant amplitude oscillations and conversion efficiency as the wind speed grows. Finally, once the wind speed exceeds a safety threshold, the damping of the system needs to be increased to a specific value in order to prevent the instability occurrence.

From the power comparison in Figure 6.2, it seems that VIVs and galloping are characterized by the same power output. In reality, even if the mechanical power absorbed from the wind is similar in the two cases, even slightly higher for VIVs, the actual electric power output will be only a fraction of this value: in facts, part of the power absorbed by the structure would be dissipated through mechanical losses. As explained in the previous chapters, both VIVs and galloping are characterized by an optimal value of the mass-damping parameter that maximize the energy conversion: in particular, it was found that $(m_r\zeta)_{opt}$ is equal to 0.2 for the VIVs system, and 1.8422 for the galloping system using a rectangular section prism. Consequently, for each value of reduced mass there is a correspondent optimal damping ratio, as reported in the following table.

Reduced mass	ζ_{opt} - VIVs	ζ_{opt} - galloping
5	0.0400	0.3684
15	0.0133	0.1228
25	0.0080	0.0737
35	0.0057	0.0526

Table 2 Optimal damping ratio for VIVs and galloping energy harvesters, for different values of reduced mass.

As can be noted, VIVs requires very small damping ratios even with low reduced masses. Moreover, as already mentioned, structures in air are usually characterized by moderate or high values of reduced mass. Realistically, the energy harvester structures can reach reduced masses in the range between 25 and 35, using material with good mechanical properties and low densities, such as aluminium or composites. Consequently, the optimal damping ratio required by VIVs systems would be comparable with the damping contribute of the mechanical losses, which can easily be around 0.002, and the net power output would be highly lower than what predicted. Obviously, the more the reduced mass is high, the more the mechanical losses will impact on the harvested power. On the contrary, galloping can work with higher values of damping ratio, allowing to convert a much bigger fraction of the absorbed energy into electricity.

Another aspect of energy harvesters based on flow-induced vibrations is the orientation of the system with respect to changing wind direction. In facts, it is clear that the galloping instability strongly depends on the bluff body orientation: as explained in the theoretical chapter, sometimes the same cross section shows orientation in which can develop the instability and others in which it can’t, as in the case of the triangular or “D” cross section. Moreover, both VIVs and galloping develop a significant motion in the transverse direction with respect to the wind flow: this means that in both the cases the structure needs to orientate itself in the right direction as the wind changes, eventually using a fin in the back as in small size wind turbines. A brilliant solution to this problem has been proposed by Vortex Bladeless, whose design relies on a completely axial symmetric structure, free to oscillate in any direction, and on an omnidirectional electric generator, capable to absorb the energy of oscillations independently by their direction. Unfortunately, this kind of solution can only be applied to VIVs, since the circular section is the only perfectly symmetric.

6.2. Concept proposal

From the comparison between VIVs and galloping it is clear that the second phenomenon of fluid-structure interaction is more suitable to be used by wind energy harvester, even if it presents some problems especially as regards the amplitude of the oscillations.

In an attempt to solve these issues, the proposed concept consists of an elastically mounted bluff body that is forced to rotate around a pivot, placed at a distance R from the centre of its section (Figure 6.3). Furthermore, the kinematic mechanism used forces the bluff body to maintain the same orientation with respect to the wind direction and guarantees the fact that the relative wind speed is the same at every point of its profile.

In fact, if the body was aligned with the rod connecting it to the pivot, during the oscillations the angle of attack would be strongly influenced by the angular position, and would quickly reach values outside the range where the instability is established. Moreover, the relative velocity of the flow with respect to the bluff body profile would be different at each point of the profile, making the use of aerodynamic force coefficients derived from static tests, therefore also of the pseudo-static approximation, unreliable.

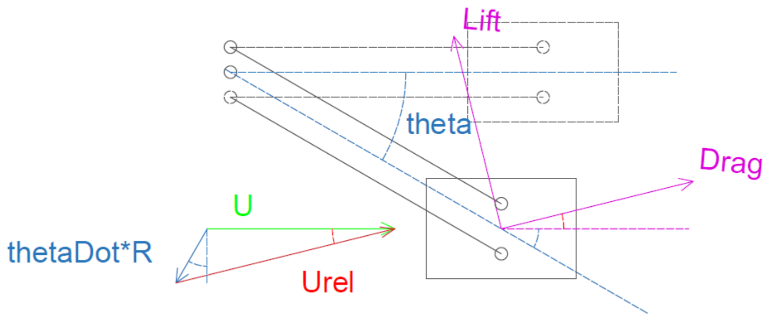

Figure 6.3 Scheme of the proposed energy harvester concept based on galloping.

The adoption of the described kinematic mechanism converts the linear force and motion of transverse galloping into torque and rotation, which in the opinion of the author allows more flexibility in the choice of an alternator. In addition, it introduces a non-linearity in the system stiffness, which helps limiting the maximum amplitudes reached by the system at high wind speed, besides the fact that the mechanism itself constitutes a physical boundary that confines the system motion even in case of free oscillations. Finally, the proposed concept can exploit the in-line component of the fluid force to help reorient the whole system when the wind direction changes.

Referring to the scheme in Figure 6.3, the governing equation of the system dynamic is:

$$I_t\ddot{\vartheta} + c_t\dot{\vartheta} + k_t\vartheta = \frac{1}{2}\rho {U_{rel}}^2 DR[-C_L\cos(\vartheta-\alpha) + C_D\sin(\vartheta-\alpha)] \tag{6.1}$$

Where ϑ is the angular coordinate, I_t is the modal moment of inertia, while c_t and k_t are the modal damping and stiffness, which are given by the sum of structural and electromechanical contributes. D is the front side length and R is the pivot arm length.

Because of the different kinematics the angle of attack α and the relative wind speed can be calculated from the relations:

$$\tan(\alpha) = \frac{R\dot{\vartheta}\cos\vartheta}{U-R\dot{\vartheta}\sin\vartheta} \tag{6.2}$$

$${U_{rel}}^2 = \left(R\dot{\vartheta}\right)^2 + U^2 - 2R\dot{\vartheta}U\cos\left(\frac{\pi}{2} + \vartheta\, sign(\dot{\vartheta})\right) \tag{6.3}$$

The resulting Simulink model is reported in Figure 6.4: with respect to the transverse galloping model, in this case there are a few complication due the more complex kinematics of the system, which depends on the angular position ϑ.

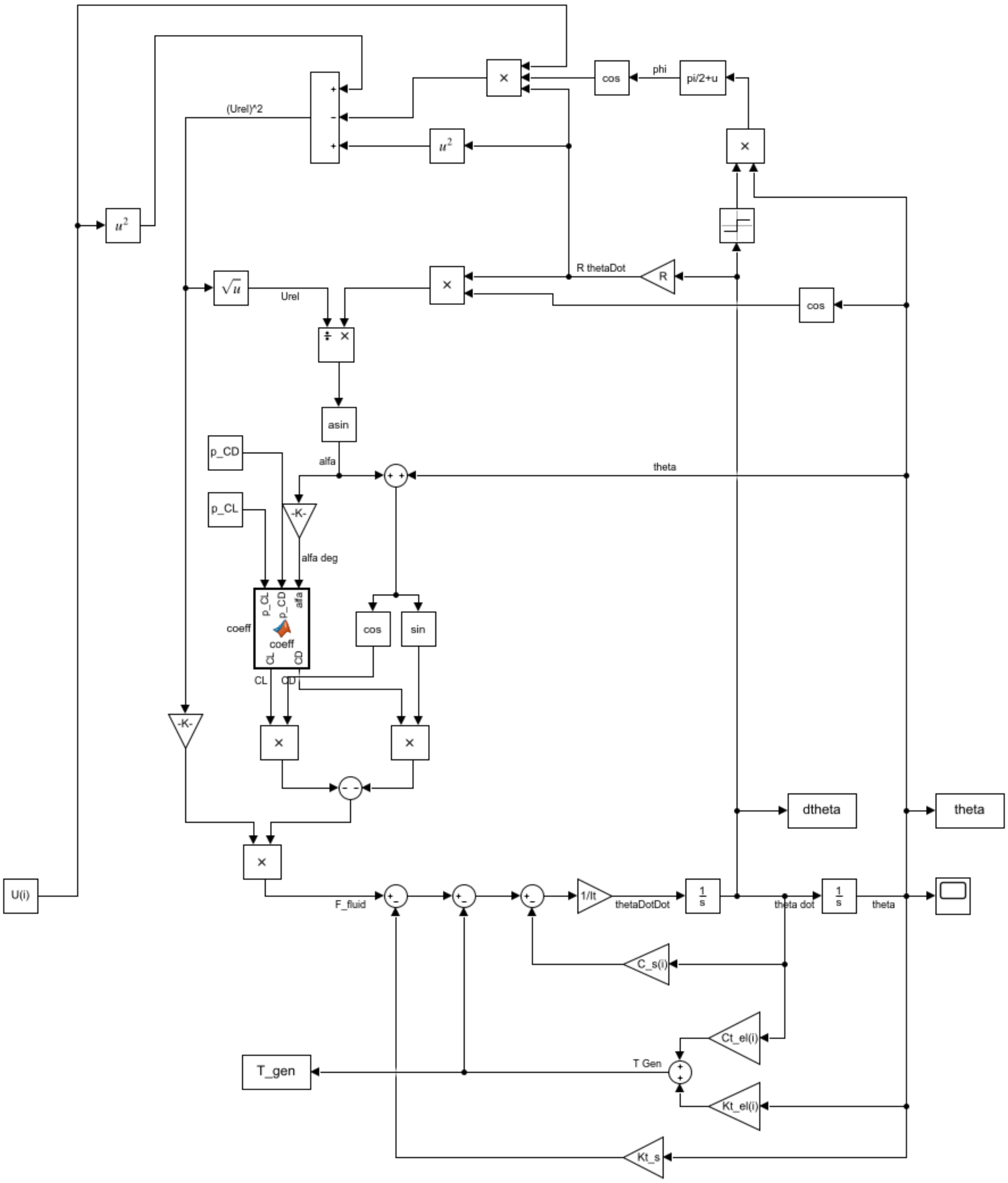

Figure 6.4 Simulink model of the proposed energy harvester concept.

In proposed model, it has been introduced the same control on the electromechanical stiffness and damping as for the transverse galloping one.

6.2.1. Critical wind speed

Applying the same assumptions as made for the pure transversal galloping, it is possible to determine the critical speed above which the instability occurs as a function of the structure parameters. In facts, considering the system in t its static equilibrium position ($\vartheta = 0$), perturbed by a infinitesimal angular velocity ($\dot{\vartheta} \rightarrow 0$), the relations become:

$$\vartheta = 0 \;\Rightarrow [\,\cos(\vartheta) = 1\,, \qquad \sin(\vartheta) = 0\;] \Rightarrow \tan(\alpha) = \frac{R\dot{\vartheta}}{U}$$

$$\dot{\vartheta} \to 0 \quad \Longrightarrow \quad \alpha \cong \tan(\alpha) = \frac{R\dot{\vartheta}}{U} \to 0$$

And consequently,

$$\cos(\vartheta - \alpha) = \cos(-\alpha) \cong 1$$

$$\sin(\vartheta - \alpha) = -\sin(\alpha) \cong -\alpha$$

$$U_{rel} = U$$

Moreover, for small values of α, the lift and drag force coefficients for the rectangular cross section can be expressed as:

$$C_L|_{\alpha\to 0} = C_L|_{\alpha=0} + \left.\frac{\partial C_L}{\partial \alpha}\right|_{\alpha=0} \alpha = \left.\frac{\partial C_L}{\partial \alpha}\right|_{\alpha=0} \alpha$$

$$C_D|_{\alpha\to 0} = C_D|_{\alpha=0} + \left.\frac{\partial C_D}{\partial \alpha}\right|_{\alpha=0} \alpha = C_D|_{\alpha=0}$$

Hence, the motion equation can be rewritten as:

$$I_t\ddot{\vartheta} + c_t\dot{\vartheta} + k_t\vartheta = \frac{1}{2}\rho \mathrm{U} D R^2 \left[-\left.\frac{\partial C_L}{\partial \alpha}\right|_{\alpha=0} - C_D|_{\alpha=0}\right]\dot{\vartheta} \tag{6.4}$$

The critical wind speed is then calculated as:

$$U_{cr} = \frac{2c_t}{\rho D R^2\left(-\left.\frac{\partial C_L}{\partial \alpha}\right|_{\alpha=0} - C_D|_{\alpha=0}\right)} \tag{6.5}$$

Introducing the already defined dimensionless parameters, and defining a reduced inertia as the equivalent of reduced mass in a rotating system,

$$I_{t_r} = \frac{I_t}{\rho D^2 R^2} \tag{6.6}$$

The critical reduced velocity can be expressed in the same form as made in for the transverse galloping:

$$U_{r_{cr}} = \frac{8\pi I_{t_r}\zeta}{\left(-\left.\frac{\partial C_L}{\partial \alpha}\right|_{\alpha=0} - C_D|_{\alpha=0}\right)} \tag{6.7}$$

Since the reduced inertia is the ratio between the system inertia and the inertia of corresponding volume of air respect the same center of rotation, it can be verified that the it has the same value of the reduced mass defined for the same system. As a consequence, the critical wind speed is not affected by the introduction of the pivot mechanism.

6.2.2. Effects of pivot arm length

The proposed concept introduces the pivot length as a new parameter in the physical model. In order to evaluate the its effects on the system, the following figures show how oscillation amplitude, absorbed power and efficiency change as the pivot arm length increases, for a system with a front side equal to 0.16 m.

As reported in Figure 6.5, the oscillation semi-amplitude changes significantly as R varies, if expressed as the angle swept during the motion: the more R is short, the more ϑ reaches higher values. On the other hand, the effective transversal amplitude does not changes significantly with R, showing slightly higher values for longer pivot arms.

Interestingly, for what concerns the absorbed power and the conversion efficiency, different values of R produce the same performances, as shown in Figure 6.6. Moreover, the results are practically identical to those obtained for the pure transverse galloping.

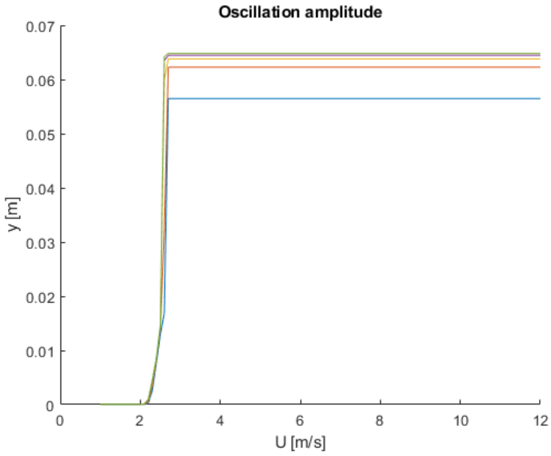

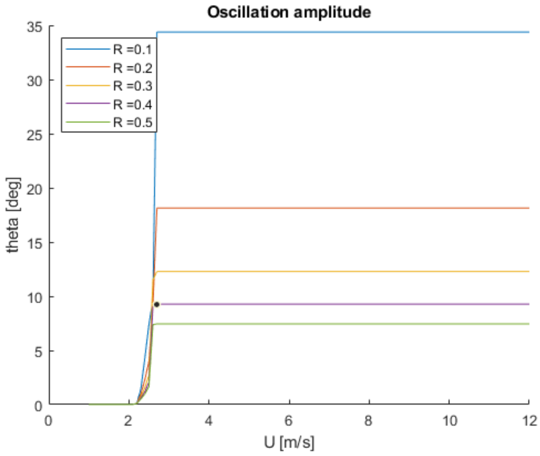

Figure 6.5 Oscillation semi-amplitude calculated for different values of the pivot arm length. D = 0.16 m

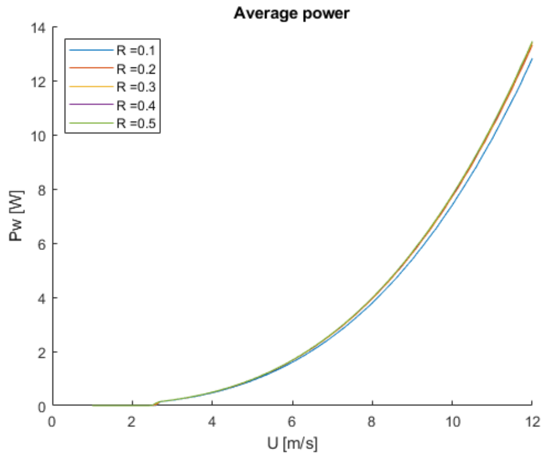

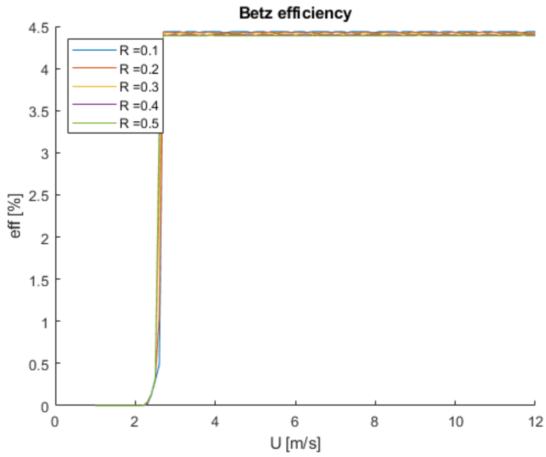

Figure 6.6 Absorbed mechanical power and efficiency, calculated for different values of the pivot arm length. D = 0.16 m

One interesting effect of the pivot arm length on the system dynamics is the variation of its natural frequency as the nonlinearity in the stiffness becomes stronger. In facts, small values of R produce a sensible increment in the actual oscillation frequency, affecting the value of reduced velocity, which results lower than expected (Figure 6.7, left side). Therefore, too short R can have a negative effect on the system performances, which are optimal in a given range of reduced velocity and damping ratio, as explained in the galloping chapter.

On the other hand, small R have positive effects on the power density, calculated as the ratio between the produced power and the occupied area on the ground, which in the case of this concept, has been considered as the circular surface swept by the system while rotating of 360°. The power density can be used as a parameter to evaluate the system performance, in particular if one need to compare it with other technologies such as photovoltaic panels. Intuitively, the occupied are is proportional to the square of the pivot arm, thus shorter values of R are preferred (Figure 6.7, right side).

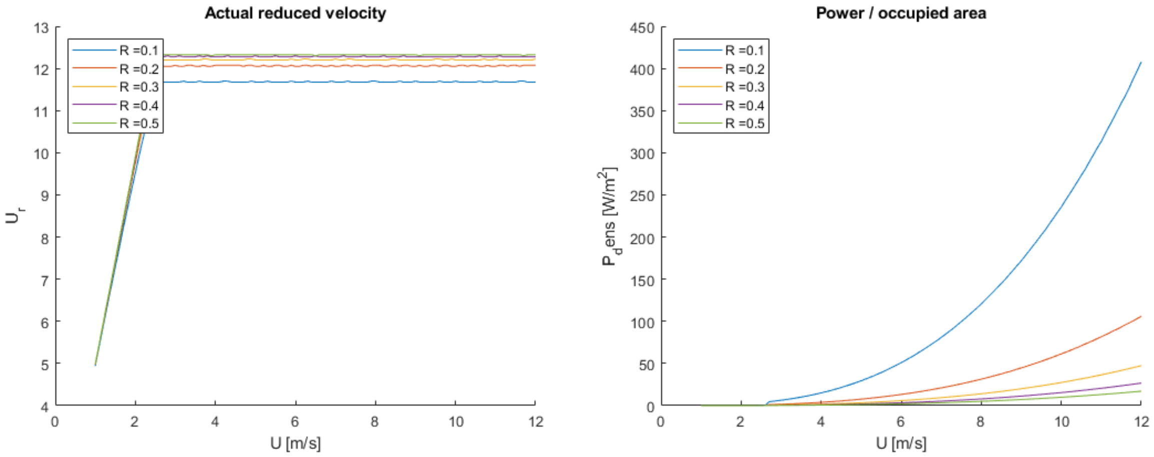

Figure 6.7 Reduced velocity and power density, calculated for different values of the pivot arm length. D = 0.16 m

Finally, the pivot arm size has an effect on the torque and angular velocity transmitted to the gearbox and alternator. Obviously, since the mechanical power must be constant, long arms generate high torques and small angular velocity, while long arms would do the opposite (Figure 6.8). Considering the magnitudes involved, a gearbox is needed to transform the mechanical power into higher angular velocity and smaller torques, which are better condition for electric alternators. As a consequence, shorter pivot arms will require smaller reductions in the gearbox, and also involve smaller torques on the mechanic structure.

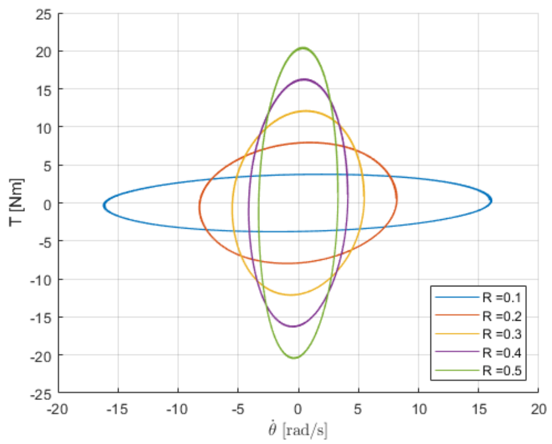

Figure 6.8 Torque and angular speed required from the alternator at a wind speed of 8 m/s, calculated for different values of the pivot arm length. D = 0.16 m

Taking into account all the exposed considerations, the optimal length of the pivot arm should be as short as possible, compatibly with the constrains on the reduced velocity. Thus, in the author opinion, the best value for R in the presented case, with D = 0.16, is 0.2.

7. Case study application

In the following, wind speed measurements are used to develop a preliminary design of the energy harvester proposed in the previous chapter and assess its performance. In this case, the purpose of the design is to obtain a device capable to work with moderate wind speed, and produce a power output of the order of some Watt, occupying a volume lower than 1 m^3.

7.1. Wind assessment

Wind data has been taken from the *Ministero delle agricole alimentari, forestali e del turismo* website, where hourly wind speed and direction measurements at 10 m altitude are available for a set of locations distributed around Italy.

Since the purpose of the energy harvester is to operate with moderate wind speed, it has been chosen a proper reference site, which presents a moderate wind speeds distribution: in particular, the selected wind measurements have been collected by the meteorological station of Albenga during the years 2015, 2016 and 2017.

As known, wind speed is characterized by an high variability in almost all the time scales. In facts, by plotting the measurements in chronological order, it is possible to notice significant and unpredictable differences between the wind speed values over a year, a season and even during the same day. In Figure 7.1, it is reported as an example the mean wind speed value for each day of the year 2017.

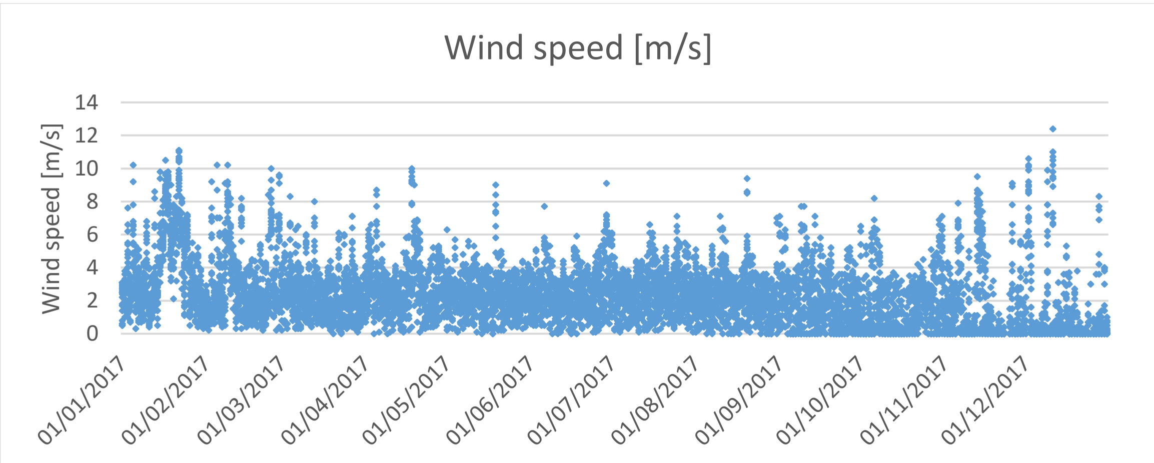

Figure 7.1 Hourly wind speed measurements in Albenga *(Ministero delle agricole alimentari, forestali e del turismo, 2019)*

Moreover, wind presents a strong variability also in its direction, as reported in Figure 7.3. Even if one site is characterized by a main direction in which the wind blows more frequently, as in the case in exam, the direction variability still plays a big role in the wind power generation, thus an energy harvester device needs to be capable of reorienting itself along the wind direction as it changes.

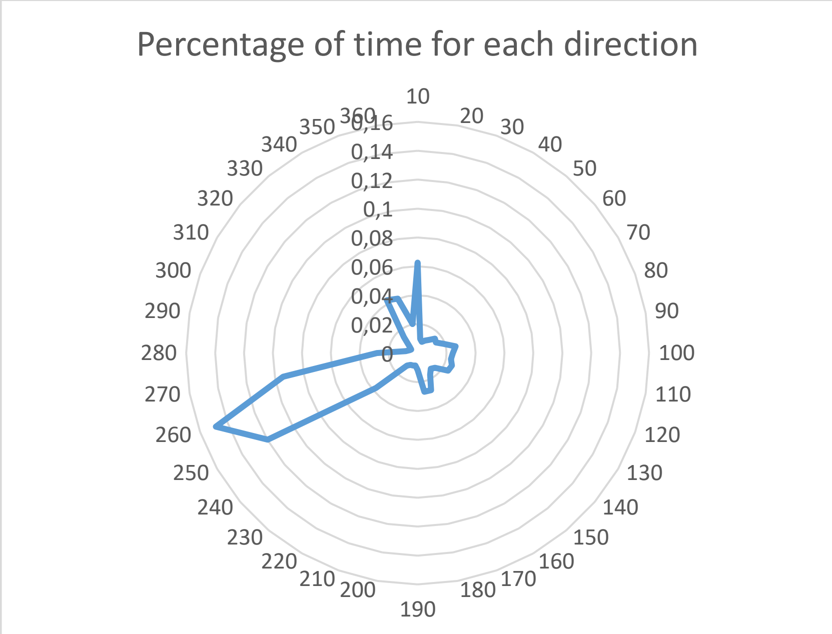

Figure 7.3 Wind rose diagram representing the frequency of wind direction in Albenga. (360° stays for North, 180° for South and so on).

In order to assess the energy content of the site, and understand which particular wind speed should be taken as a reference for the energy harvesting design, the best practice is to organize the wind data in a histogram that reports the probability with which each wind speed can be found during the year (Figure 7.2). As can be seen, in the reference site the wind blows very frequently at moderate speed between 1.5 and 3.5 m/s, while it is quite rare to find winds faster than 5 m/s. The maximum measured speed is 12.4 m/s, the most frequent wind blows at 3 m/s, while half of time the measured wind speed has been lower than 2.4 m/s.

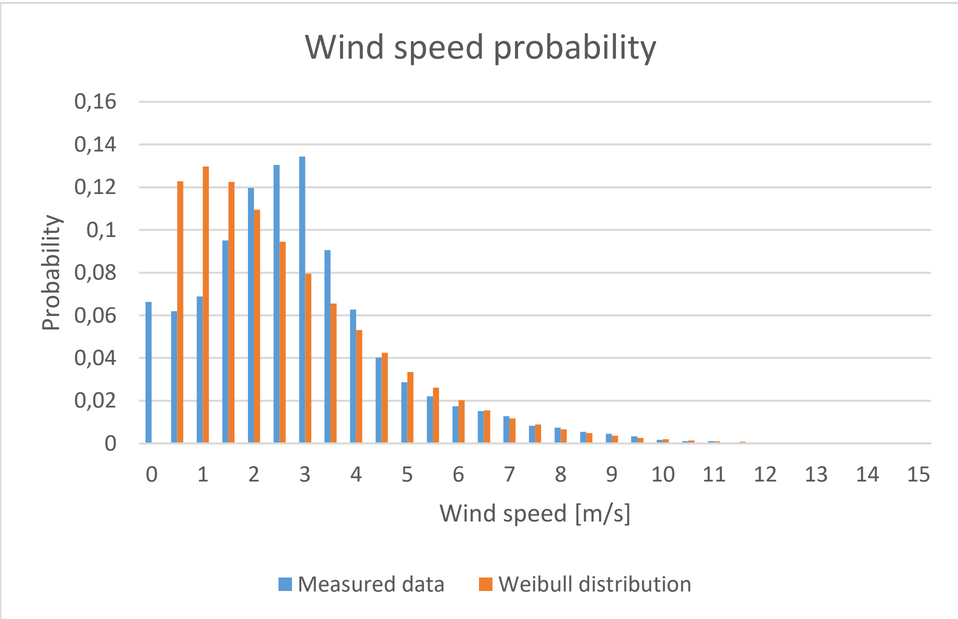

Figure 7.2 Wind speed measured data and Weibull probability distribution in Albenga.

Each wind speed provides a certain energy density, calculated as the product between the number of hours in which the wind blows at a certain speed for the power associated with it, which depends on its cubic value. As a result, the energy density of the reference site presents a completely different distribution compared to the wind speed Figure 7.4. In facts, low wind speed, even if more frequent, are characterized by low power, hence their fraction on the total available energy is small. On the contrary, high wind speed provide big amount of power, and their share on the total energy available is high, even if they appear less frequently.

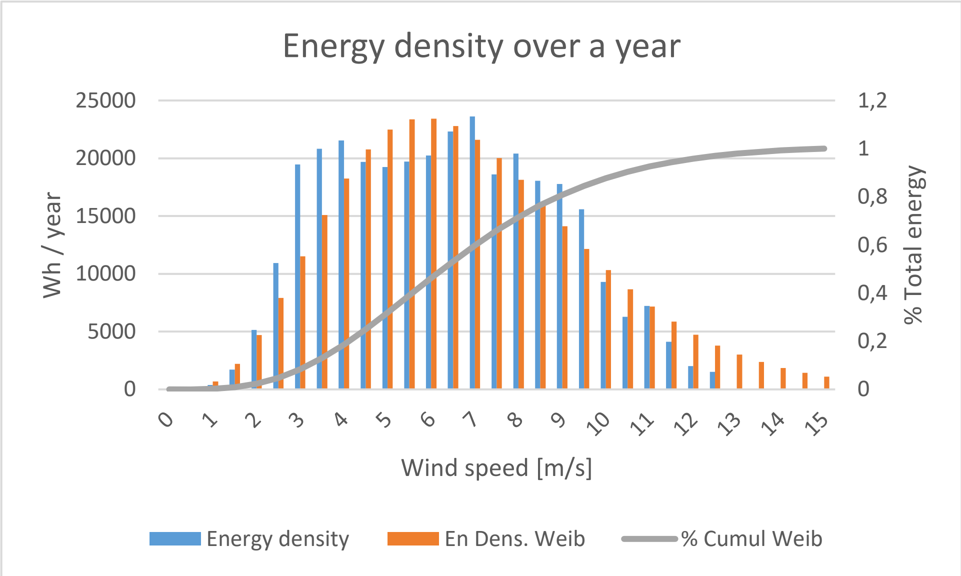

Figure 7.4 Wind energy density in Albenga, from measured data and Weibull probability distribution.

Commonly, the wind speed distribution can be replaced by a Weibull distribution, which is found to express quite accurately the probability at which wind speed is found along the year. The Weibull curve and the associated energy density reported in the figures have been determined by equalizing the total energy density calculated from the collected data and the one relative to the Weibull distribution.

The analysis of wind speed and energy distribution can highlight the range of wind speed in which it is important to obtain the best performances with the proposed energy harvester. In particular, it should guide the designer in the choice of the nominal power of the device, which of course will define the size and the cost of the energy harvester.

7.2. Preliminary design

Since one of the constrain we assumed for the design process is that the device should occupy a volume lower than 1 m^3, the first step is to determine the dimensions of the main parameters.

Assuming a height for the device equal to 1 m, the power output, which is proportional to the swept area, will depend on the length of the prism front side. Hence, to maximize the power output, it has been chosen a bluff body with the characteristic length $D = 0.16\ m$, which is the limit to respect the constrain on the aspect ratio($\frac{l}{D} \geq 6$). Being the prism cross section a rectangle with side ratio $\frac{B}{D} = 1.5$, its longest side will be $B = 0.24\ m$.

Given the its dimensions, the mass of the bluff body will depend on the material used, which need to be light and present good mechanical properties in order to minimize the structure weight. Examples can be aluminium or composite, which can provide the requested strength with thin sheets. In the following, it has been assumed to use a 0.5 mm thick aluminium profile as bluff body, and considering a density of 2700 kg/m^3, the mass would be equal to:

$$m = D^2\left(2(1+\frac{B}{D})\frac{s}{D}\rho_s + C_a\pi\rho_{air}\right)l = 1.22\ kg \quad (7.1)$$

Where $C_a = 1.51$ according to Blevins (Blevins, 2001).

Then, the pivot arm length R needs to be chosen according to the considerations made in Chapter 6: based on Figure 6.7and Figure 6.8, which show the effect of different values of R with $D = 0.16\ m$, it seems that the best option to obtain a good power density and respect the constrains on the reduced velocity, is to set $R = 0.2\ m$.

Therefore, the resulting momentum of inertia and the corresponding reduced momentum of inertia are:

$$I_t = m * R^2 = 0.059\ kg/m^2 \quad (7.2)$$

$$I_{t_r} = 1.2\frac{I_t}{\rho D^2 R^2} = 56.42 \quad (7.3)$$

In the reduced momentum of inertia it has been introduced an increase of 20% in order to consider the inertia of pivot arms and generator. It should be noted that the obtained result is probably an overestimation of the system inertia, which will determine lower conversion efficiency and power output. However, the purpose of this work is to assess the potential of the proposed energy harvester concept, which will eventually be optimized in the following works.

Subsequently, the system stiffness and damping have been calculated for each value of wind seed, following the consideration discussed in Chapter 5.

Based on the wind speed distribution, the cut-in velocity has been set equal to 2 m/s: in facts, lower wind speed contain only about the 2% of the total available energy, even if they blow during 40% of the time. The required structural natural frequency and torsional stiffness, are calculated in order to obtain the optimal reduced velocity (equal to 12.5, see Chapter 5) in correspondence of the cut-in wind speed:

$$f_{n_s} = \frac{U_{start}}{U_{r_{opt}}D} = 1\ Hz \quad (7.4)$$

$$k_s = \omega_n{}^2 I_t = \left(2\pi f_{n_s}\right)^2 I_t = 2.33\ Nm/rad \quad (7.5)$$

From the cut-in speed on, the frequency of the structure will be tuned controlling the electromechanical contribute k_{em} to the system stiffness k_t, whose values are reported in Figure 7.6.

$$f_{n_{opt}}(U) = \frac{U}{U_{r_{opt}}D} \quad (7.6)$$

$$k_t(U) = \omega_n{}^2 I_t = \left(2\pi f_{n_{opt}}\right)^2 I_t \quad (7.7)$$

$$k_{em}(U) = k_t(U) - k_s \quad (7.8)$$

As made in Chapter 5, for each value of wind speed can be calculated an optimal value of damping.

$$c_{opt}(U) = 4\pi f_{n_{opt}}\zeta_{opt} I_t \quad (7.9)$$

Then, assuming a mechanical damping ratio equal to 0.002, the electromechanical contribute to the system damping would be:

$$c_{em}(U) = c_t(U) - c_s \tag{7.10}$$

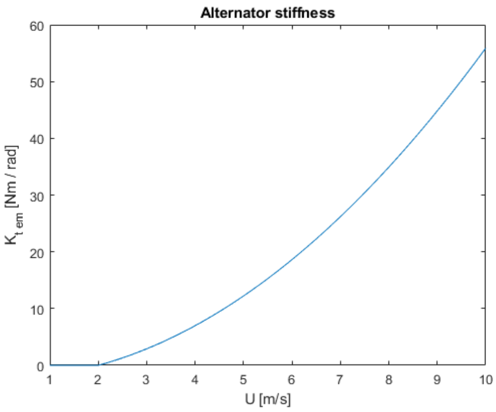

Figure 7.6 Alternator optimal stiffness.

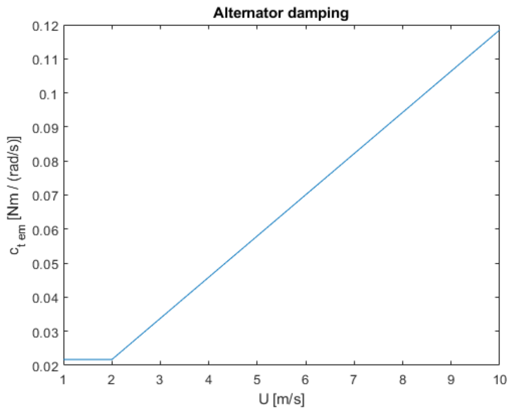

Figure 7.6 Alternator optimal damping.

Once all the system parameters have been defined, the electric alternator has been chosen by comparing the required performance with the characteristic curves of the available alternators.

Since both optimal stiffness and damping increase with the wind speed, the same happens for the alternator required performances: therefore, the higher the nominal wind speed is set, the bigger will be the alternator size and power, and consequently price. As a consequence, the selection of the nominal speed and the correspondent alternator is a techno-economic problem, which need different kind of considerations in order to be properly answer. In the context of this work, it has been chosen a nominal wind speed of 7 m/s. In facts, higher wind speeds appear less than the 4% of the time over a year, hence in the opinion of the author it is not worth over-sizing the system for such a low frequency of use. Moreover, the power carried by higher wind speed, which is still about the 30% of the total available energy, will not be lost, but it will just be harvested with lower efficiency.

In Figure 7.8are reported the requested torque and angular speed by the dynamic system while oscillating at the selected nominal speed of 7.5 m/s. The maximum torque and angular speed are:

$$T = 8.83\ Nm$$

$$\dot{\vartheta} = 7.57 \frac{rad}{s} = 72.30\ rpm$$

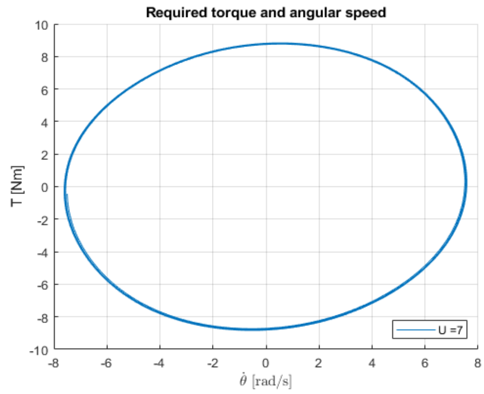

Figure 7.8 Alternator optimal stiffness.

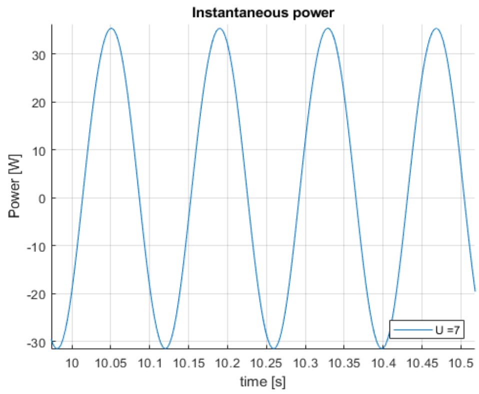

Figure 7.8 Alternator optimal damping.

As can be noted in Figure 7.8, the involved instantaneous power is much higher than the average output power. Unfortunately, this means that the alternator needs to be an high nominal power in order to handle the power exchanges during the oscillations.

Comparing the characteristics of the alternators available among the Maxon Motors website, it has been chosen the brushless motor *EC-i 30*, whose nominal power is 50 Watts, together with the *Planetary Gearhead GP 32 C*, with a reduction of 1:159.

Values at nominal voltage	
Nominal voltage	24 V
No load speed	9960 rpm
No load current	169 mA
Nominal speed	8840 rpm
Nominal torque (max. continuous torque)	55.5 mNm
Nominal current (max. continuous current)	2.48 A
Stall torque	768 mNm
Stall current	33.7 A
Max. efficiency	86 %
Characteristics	
Terminal resistance	0.713 Ω
Terminal inductance	0.475 mH
Torque constant	22.8 mNm/A
Speed constant	418 rpm/V
Speed / torque gradient	13.1 rpm/mNm
Mechanical time constant	1.89 ms
Rotor inertia	13.8 gcm²
Thermal data	
Thermal resistance housing-ambient	9.01 K/W
Thermal resistance winding-housing	2.46 K/W
Thermal time constant winding	31.2 s
Thermal time constant motor	1080 s
Ambient temperature	-40...+100 °C
Max. winding temperature	+125 °C
Mechanical data	
Max. speed	15000 rpm
Axial play	0 - 0.14 mm
Max. axial load (dynamic)	5 N
Max. force for press fits (static)	98 N
(static, shaft supported)	1300 N
Max. radial load	25 N, 5 mm from flange
Other specifications	
Number of pole pairs	2
Number of phases	3
Number of autoclave cycles	0
Product	
Weight	240 g

Figure 7.9 EC-i 30 Ø30 mm 50 W brushless motor specifications *(Maxon Motor, 2019)*

In Figure 7.10 it is shown the comparison between the selected motor characteristic curve and the requested performances by the system.

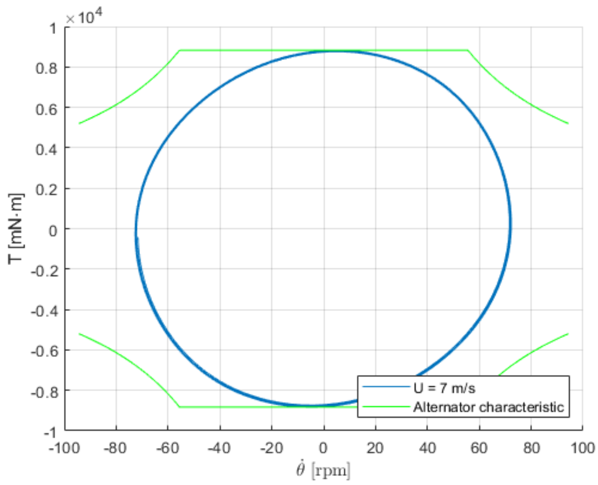

Figure 7.10 Alternator characteristic curve and required performances (U=7 m/s) comparison.

7.3. Results

The following figures report the results obtained by introducing the alternator characteristic curve into the Simulink model, thus imposing it as a limit to the alternator torque.

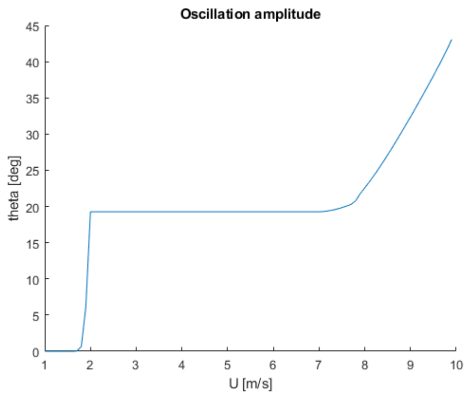

Figure 7.12 Oscillation semi-amplitude

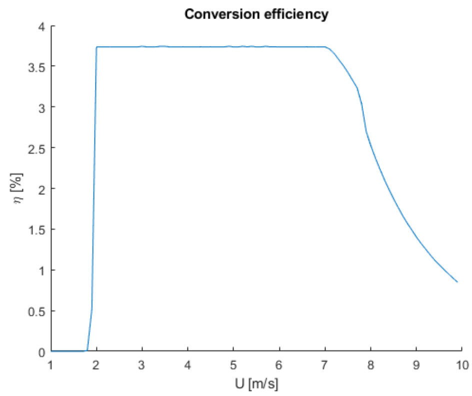

Figure 7.12 Conversion efficiency from fluid power to mechanical power input to the alternator.

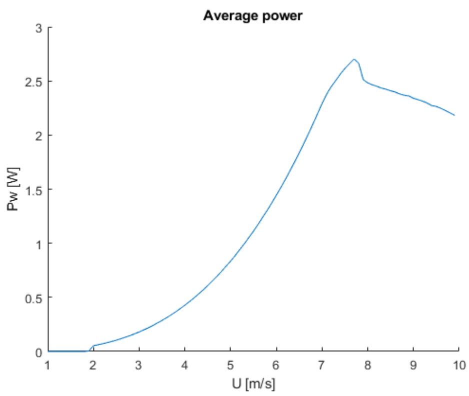

Figure 7.14 Mechanical power input to the alternator.

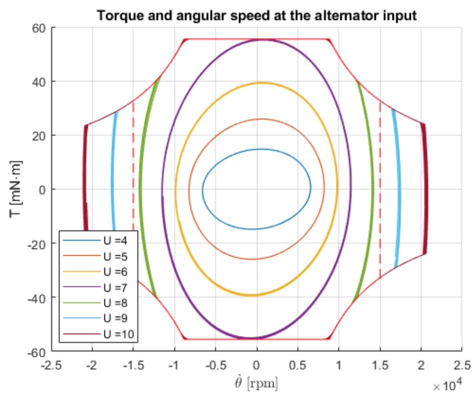

Figure 7.14 Torque and angular speed at the alternator input.

As can be seen, the amplitude remains constant as the wind speed increases up to about 7 m/s. from this point on, the theoretical torque, required to maintain the optimal system stiffness and damping, becomes higher than the maximum alternator one. Therefore, the system cannot be stabilized: oscillation amplitudes start growing, the conversion efficiency drops, and the power decreases slightly. Moreover, as the wind speed continues growing and overcomes 8 m/s, the angular speed at the alternator exceeds the maximum speed supported. As a consequence, in order to obtain a stable system it is necessary to develop a different strategy of control for wind speed higher than the nominal one.

For instance, increasing the damping value starting from wind speed higher than 8 m/s can reduce the oscillation amplitudes and the angular speed of the response. Moreover, the damping value can be raised up to the critical value that stops the galloping instability at a particular wind speed.

$$c_{t_{cr}} = \frac{U\rho D R^2}{2}\left(-\frac{\partial C_L}{\partial \alpha}\bigg|_{\alpha=0} - C_D|_{\alpha=0}\right) \tag{7.11}$$

With the aim to limit the maximum angular speed reached by the system inside the constrains imposed by the alternator, it has been imposed a cut-off wind speed of 8.5 m/s. Then, the damping value has been linearly increasing starting from the optimal value at $U = 8\,m/s$ in order to reach the critical value for $U = 8.5\,m/s$, augmented by 20%. Finally, the damping value has been maintained above the critical threshold also for higher wind speeds.

The results obtained with the new proposed control strategy are shown in the following figures, in which it is possible to notice how the system is damped out when wind speed approaches 8.5 m/s.

In facts, the oscillation semi-amplitude, which grows as the wind speed rises from 7 m/s to 8 m/s, subsequently start decreasing while the system damping is augmented. Interestingly, both the conversion efficiency and the average power show a second peak as the system is damped. One reason could be found in the kinetic energy that the system fist accumulated as the oscillation amplitude increases with wind speed between 7 and 8 m/s, and then converted when the damping is strong enough to slow down the system.

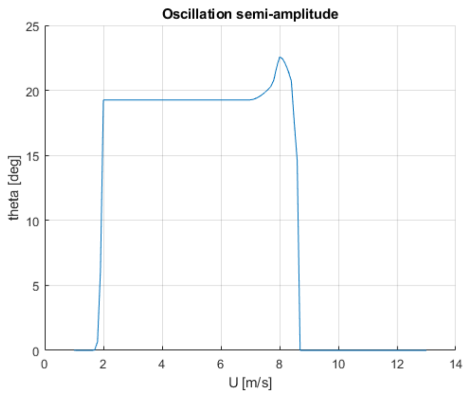

Figure 7.18 Oscillation semi-amplitude

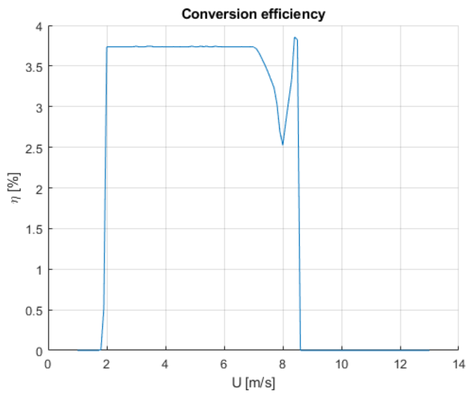

Figure 7.18 Conversion efficiency from fluid power to mechanical power input to the alternator.

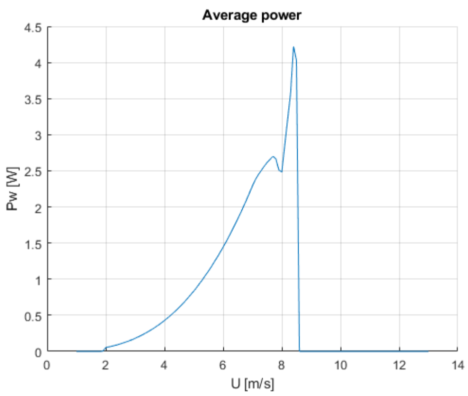

Figure 7.16 Mechanical power input to the alternator.

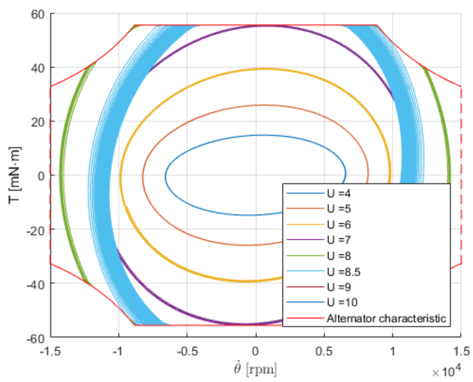

Figure 7.16 Torque and angular speed at the alternator input.

As expected augmenting the system damping reduced the maximum angular speed requested to the alternator: in facts, Figure 7.16 shows that with the new control strategy on the damping the system does not reach the upper limit of rotational speed as made before. Furthermore, the figure shows how the increased damping gradually slows down the system with wind speeds higher than 8 m/s.

However, it is important to note that in the context of this work, the proposed control strategy is just an example of how to obtain a safe response at wind speeds that exceed the nominal one, and that further work needs to be done in the definition of an optimal control strategy. Also, it should be noted that the obtained results are affected by an eventual overestimation of the system inertia, which will determine lower conversion efficiency and power output. However, the purpose of this work is to assess the potential of the proposed energy harvester concept, which will eventually be optimized in the following works.

Figure 7.19 shows the power density over the occupied soil surface, defined as in Chapter 6. As shown, the proposed design reaches a peak of 13 W/ m^2, which overall can be considered a good result for this preliminary design phase. Even if it is a modest power density, it can be compared with those of photovoltaic panels, which in optimal condition reaches about 120 W/ m^2. Moreover, it must be considered the limited wind resource of the considered site: in facts, with higher wind speeds, the system would have consequently generated higher power.

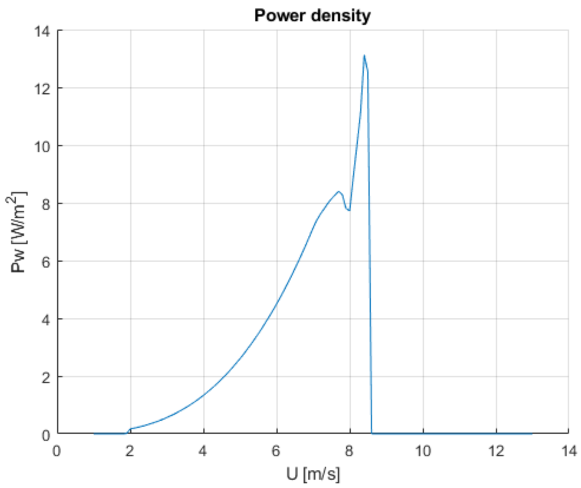

Figure 7.19 Ratio between the mechanical power input to the alternator and the total occupied soil surface..

Finally, the following graph shows the generated energy over a year by the proposed concept in the reference site of Albenga.

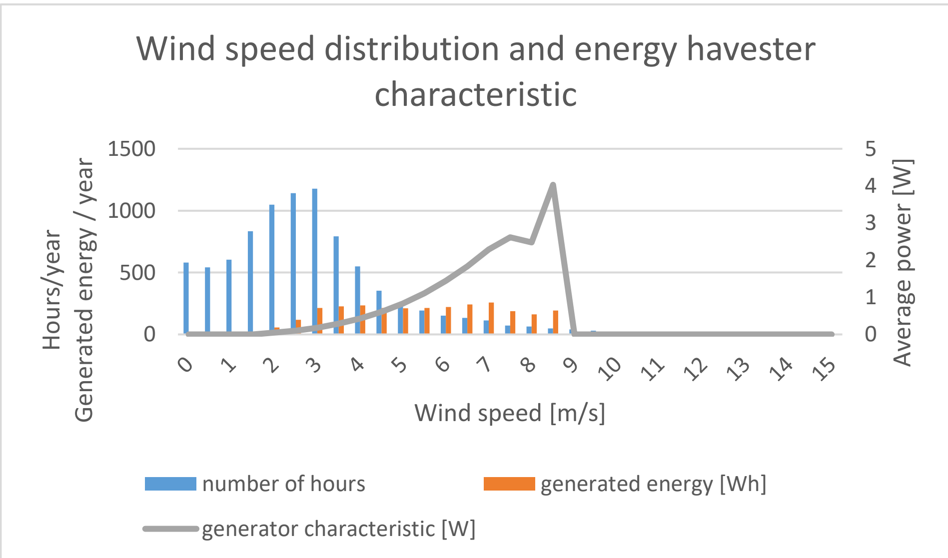

Figure 7.20 Energy produced over a year by the proposed energy harvester in the reference site.

The generated energy has been calculated by multiplying the number of hour in which the wind blow at a certain speed for the power produced by the energy harvester at the same wind speed. In this particular case study, the energy harvester would produce power during about 60% of the time, generating about $2760\ Wh$ over a year. Defining the rated power of the energy harvester as that in correspondence of the point where the alternator characteristic starts to saturate, which is $P_N = 2.6\ W$, the resulting capacity factor would be equal to 0.12, which is quite low. Of course, this depends also on the selected site: the better the site, the higher the capacity factor. However,

The obtained results show that the generated energy is very low, confirming that the system do not have the necessary properties to be employed in high power applications. On the other hand, the produced energy appear to be adequate with respect to purpose of supplying small amount of power to wireless sensors and electronic devices.

8. Conclusions and further works

In this work has been studied the potential of systems based on flow-induced vibrations, and in particular vortex-induced vibrations and galloping, in wind power generation applications. In fact, although in the past years there have been several studies on the subject, there is still confusion about the real potential of FIVs-based energy harvesters. Therefore, this work is an attempt to analyse the two phenomena under different perspectives, in order to identify their strengths and limits. The analysis of the phenomena was based on the most applied models in the scientific literature, taking into consideration the hypotheses on which they are built.

In the course of the work it was found that both phenomena have low conversion efficiencies and therefore do not seem suitable to be used to generate large amount of power, in particular if compared with the traditional wind turbines. On the other hand, it was found that they have the necessary characteristics (design simplicity, small volumes and low cost) to find an application in the generation of small powers, used to feed isolated sensors and electronic devices.

Furthermore, the analysis of VIVs and galloping revealed that the former need extremely light structures for their use in energy generation, which are difficult to obtain even with high-performance materials. Galloping, on the other hand, is less affected by the lightness of the structure, which still have positive effects on the performances, but it presents the problem of oscillations that grow enormously as the wind speed increases.

In addition, it has been studied the effect of the prism section type on the performances of galloping-based energy harvester, using experimental data on aerodynamic lift and drag coefficients available in the literature. It emerged that the most suitable section in the generation of energy is the rectangular shape, with a side ratio of 1.5, and the short side facing the wind direction.

Finally, taking into consideration all the observations made, it has been proposed an original concept based on galloping, whose objective is to resolve or limit some of the problems associated with the fluid-structure interaction phenomenon. Therefore a preliminary design of the device was developed, in order to highlight its potential and its criticalities. In particular, the results obtained demonstrate how the proposed design can be used for the purpose of generating small powers, even in the presence of limited wind speeds. In fact, the Simulink simulations carried out with the physical model suggested that it can absorb powers of 1 W with a wind speed of 5 m / s, and peaks of about 4 W in correspondence with winds at 8 m / s. The peak power density on the corresponding occupied surface is therefore equal to 13 W / m2, which, although modest, can be almost compared with that of a photovoltaic panel.

However, it is clear that it is necessary to deepen the work done and improve it by optimizing the various aspects. In this perspective, in the opinion of the author, the main activities to be foreseen in the continuation of this work are:

- An experimental activity aimed at obtaining, for various types of sections, the trends of aerodynamic coefficients C_L and C_D, in similar Reynolds conditions, and for various turbulence regimes. This data should be used to confirm the results obtained in the context of this work, regarding the type of section of the prism most suitable for energy generation, or to identify another shape that determines better performance. Furthermore, evaluating the effect of turbulence is important to estimate the effective behaviour of the system, whose effectiveness is expected to decrease when operating in real wind conditions.
- The validation through experimental tests of the models used to describe VIVs and galloping, and the definition of limits of reduced speed regime in which the their application produces reliable results. In this context, the preliminary design carried out can be used as a reference model for experimental analysis, also considering its small dimensions.

- The development of more advanced control strategies, able to maximize the performances of the system as the wind speed changes, and the design optimization of the various components.

9. References

Abdelkefi, A., 2016. Aeroelastic energy harvesting: a review. *International Journal of Engineering Science,* Volume 100, p. 112–135.

Alonso, G. & Meseguer, J., 2006. A parametric study of the galloping stability of two-dimensional triangular cross-section bodies. *Journal of Wind Engineering & Industrial Aerodynamics,* 94(4), pp. 241-253.

Arionfard, H., 2018. *Flow-induced vibrations of two mechanically coupled pivoted circular cylinders.* s.l.:s.n.

Barrero-Gil, A., Alonso, G. & Sanz-Andres, A., 2010. Energy harvesting from transverse galloping. *Journal of Sound and Vibration,* Volume 329, p. 2873–2883.

Barrero-Gil, A., Pindado, S. & Avila, S., 2012. Extracting energy from Vortex-Induced Vibrations: A parametric study. *Applied Mathematical Modelling,* 36(7), pp. 3153-3160.

Bernitsas, M. M., Raghavan, K., Ben-Simon, Y. & Garcia, E. M. H., 2008. VIVACE (Vortex Induced Vibration Aquatic Clean Energy): A New Concept in Generation of Clean and Renewable Energy From Fluid Flow. *Journal of Offshore Mechanics and Arctic Engineering,* 130(4), p. 041101.

Blevins, R. D., 2001. *Flow-Induced Vibration - Second Edition.* Malabar, Florida: Krieger Publishing Company.

Carassale, L., Freda, A. & Marrè-Brunenghi, M., 2013. Effects of free-stream turbulence and corner shape on the galloping instability of square cylinders. *Journal of Wind Engineering & Industrial Aerodynamics,* Volume 123, pp. 274-280.

Che-Chun (Jim) Chang, R. A. K. M. M. B., 2011. VIV and galloping of single circular cylinder with surface roughness at 3.0×e4≤Re≤1.2×e5. *Ocean Engineering,* p. 1713–1732.

Dai, H., Abdelkefi, A. & Yang, Y. a. W. L., 2016. Orientation of Bluff Body for Designing Efficient Energy Harvesters from Vortex-induced Vibrations. *Applied Physics Letters,* 108(5).

EIA, 2017. *International Energy Outlook 2017,* s.l.: s.n.

Facchinetti, M., de Langre, E. & Biolley, F., 2004. Coupling of Structure and Wake Oscillators in Vortex-induced Vibrations.. *Journal of Fluids and Structures,* 19(2), pp. 123-40.

Facchinetti, M. L., de Langrea, E. & Biolleyb, F., 2004. Coupling of structure and wake oscillators in vortex-induced vibrations. *Journal of Fluids and Structures,* Volume 19, p. 123–140.

Franzini, G. R. & Bunzel, L. O., 2018. A numerical investigation on piezoelectric energy harvesting from Vortex-Induced Vibrations with one and two degrees of freedom. *Journal of Fluids and Structures,* Volume 77, pp. 196-212.

Govardhan, R. N. & Williamson, C. H. K., 2006. Defining the modified Griffin plot in vortex-induced vibration: revealing the effect of Reynolds number using controlled damping. *Journal of Fluid Mechanics,* Volume 561, pp. 147-180.

H. D. Akaydin, N. E. a. Y. A., 2012. The performance of a self-excited fluidic energy harvester. *Smart Materials and Structures.*

Hai Sun, M. M. B. C. M. E. S. K. ,. G. N. E. M., 2017. Hydrokinetic energy conversion by two rough tandem-cylinders in flow induced motions: Effect of spacing and stiffness. *Renewable Energy,* pp. 61-80.

Hartlen, R. T. & Currie, I. G., 1970. *Lift-oscillator model of vortex-induced vibration.* s.l.:Journal of the Engineering Mechanics Division.

Jayant Sirohi, R. M., 2011. Piezoelectric wind energy harvester for low-power sensors. *Journal of Intelligent Material Systems and Structures,* p. 2215–2228.

Jia, J. et al., 2018. Modeling and Analysis of Upright Piezoelectric Energy Harvester under Aerodynamic Vortex-induced Vibration. *Micromachines,* 9(12).

Khalak, A. & Williamson, C., 1999. MOTIONS, FORCES AND MODE TRANSITIONS IN VORTEX-INDUCED VIBRATIONS AT LOW MASS-DAMPING. *Journal of Fluids and Structures,* 13(7-8), pp. 813-851.

L. Zhao, L. T. a. Y. Y., 2014. Enhanced piezoelectric galloping energy harvesting using 2 degree-of-freedom cut-out cantilever with magnetic interaction. *Japanese Journal of Applied Physics.*

L. Zhao, L. T. Y. Y., 2012. Small wind energy harvesting from galloping using piezoelectric materials. *Proceedings of ASME 2012 Conference on Smart Materials, Adaptive Structures and Intelligent Systems.*

Liu, B. et al., 2013. Hysteresis Phenomenon in the Galloping of the D-Shape Iced Conductor. *Mathematical Problems in Engineering,* Volume 2013.

Liya Zhao, Y. Y., 2017. Toward Small-Scale Wind Energy Harvesting: Design, Enhancement, Performance Comparison, and Applicability. *Hindawi Shock and Vibration.*

Mannini, C., Massai, T. & Marra, A. M., 2018. Unsteady galloping of a rectangular cylinder in turbulent flow. *Journal of Wind Engineering & Industrial Aerodynamics,* pp. 210-226.

Maxon Motor, 2019. *Brushless DC Motors by maxon motor.* [Online]
Available at: https://www.maxonmotor.com/maxon/view/content/Overview-brushless-DC-motors
[Accessed 2019].

Ministero delle agricole alimentari, forestali e del turismo, 2019. *Mipaaft - Direzione del vento a 10 m media vettoriale nell'ora.* [Online]
Available at:
https://www.politicheagricole.it/flex/cm/pages/ServeBLOB.php/L/IT/IDPagina/8121
[Accessed 2019].

Ogink, R. & Metrikine, A., 2010. A wake oscillator with frequency dependent coupling for the modeling of vortex-induced vibration. *Journal of Sound and Vibration,* 329(26), pp. 5452-5473.

Païdoussis, M. P., Price, S. J. & de Langre, E., 2011. *Fluid-Structure Interactions - Cross-Flow-Induced Instabilities.* s.l.:Cambridge University Press.

Peter South, R. M., 1983. *Oscillating wind energy conversion systems,* s.l.: Solar Energy Research Institute.

Sarpkaya, T., 2004. A critical review of the intrinsic nature of vortex-induced vibrations. *A critical review of the intrinsic nature of vortex-induced,* p. 389–447.

Sebastian Pobering, N. S., 2008. Power supply for wireless sensor systems. *Proceedings of the 7th IEEE Conference on Sensors,,* p. 685–688 .

Sebastien Michelin, E. d. L., 2018. *Fundamentals of Fluid-Solid Interactions.* Palaiseau(France): École Polytechnique.

Srinivasan, S., Narasimhamurthy, V. & Patnaik, B., 2018. Reduced Order Modeling of Two Degree-of-freedom Vortex Induced Vibrations of a Circular Cylinder. *Journal of Wind Engineering & Industrial Aerodynamics,* Volume 175, pp. 342-351.

Villarreal, D. J. Y., 2016. *Electrical energy generator and method of generating electrical energy.* United States, Patent No. US 2016/0013737 A1.

Villarreal, D. J. Y., 2017. *Electrical power generator and an electrical power generation method.* United States, Patent No. US 2017/0284365 A1.

Vortex Bladeless S.L., 2018. *How it works? - Vortex Wind Turbine in a Nutshell.* [Online] Available at: https://vortexbladeless.com/technology-design/
[Accessed 30 01 2019].